Departamento de Astronomía
Facultad de Ciencias Físicas y Matemáticas
UNIVERSIDAD DE CONCEPCIÓN

Star Formation of Ultra-Faint Dwarf Spheroidal Galaxies

Formation of Dwarf Spheroidal Galaxies

Formación Estelar de Galaxias Enanas Esferoidales Ultra Débiles

Formación de Galaxias Enanas Esferoidales

Tesis para ser presentada en Dirección de Postgrado, Universidad de Concepción para optar al grado de Magister en Ciencias con Mención en Física.

CATALINA ANDREA ARAVENA NÚÑEZ
PROFESOR GUÍA: DR. MICHAEL FELLHAUER

Programa de Magíster en Ciencias con mención en Física
CONCEPCIÓN, CHILE
2020

Agradecimientos

Quisiera agradecer a todas las personas que a lo largo de estos años me han acompañado y brindado su apoyo. En primer lugar, quiero agradecer a mi familia, especialmente a mis papas por estar siempre a mi lado y porque sin ellos esto no hubiese sido posible. Agradezco a mi mamá, por entregarme su fortaleza y perseverancia y a mi papá, por cada una de sus palabras y por nunca dejar de creer en mí.

Quisiera agradecer especialmente a mi profesor guía y supervisor Michael Fellhauer, por su paciencia y apoyo constante durante todo este proceso y porque siempre estuvo dispuesto a ayudarme a solucionar cada uno de los problemas que se presentaron en el camino. Además le quisiera dar las gracias a todos los miembros del Theory Group y a mi compañeros de la sala de tesistas por su constante preocupación y palabras de ánimo, en especial agradezco a Diego Matus, por su buena voluntad y por las infinitas tarde que dedicó a ayudarme.

Agradezco profundamente a la naty, mi amiga, y quien estuvo a mi lado todos estos años, por convertise en un pilar fundamental y ser un apoyo incondicional.

Por último gracias a los programas Basal, Fondecyt y Dirección de Postgrado por la ayuda financiera, que me permitió participar de diferentes congresos.

Abstract

The dwarf galaxies prior to 2005 have absolute magnitudes brighter than $M_V = -8.7$, corresponding to V-band luminosities large than 2.5×10^5 $L_\odot$. Their Plummer (half-light) radii are $\gtrsim 200$ pc, and with the exception of Sextans and Ursa Minor, their central surface brightness are < 26 mag arcsec^{-2}. In contrast the ultra-faint dSph (UFD) galaxies, discovered in recent years, are up to a factor of ~ 1000 less luminous, with half-light radii as small as ~ 20 pc and surface brightness that can be $\sim 2-3$ mag arcsec^{-2} fainter than that of Sextans. UDFs are a continuation of the dwarf spheroidal (dSph) sequence to smaller and fainter objects. These galaxies exhibit similar properties such as old, metal-poor populations, patchy and distorted shapes and high velocity dispersions. They might be amongst the first galaxies in the early Universe and are therefore interesting probes of early structure formation.

The standard formation scenarios involve strong destructive processes which finally let to their shape we see today. Assmann et al. (2013a) proposed a scenario in which star clusters form in the dark matter (DM) halo of a dSph galaxy. These clusters suffer from low star formation efficiency and dissolve while orbiting inside the halo. Thereby they built the faint luminous component that we observe in dSph galaxies.

In our project, we test the possible formation scenario for dSph galaxies for the formation of UFDs. We model Segue 1 by performing numerical simulations, with a strong background potential mimicking the dark matter halo and our stars are initially in virial equilibrium and placed in a filamentary stellar distribution, a fractal distribution, within an analytical halo, building the faint luminous component that we observe. We expect our scenario, using Segue 1 as example, is able to reproduce kinematical and structural features of UFDs we see today.

Resumen

La galaxias enanas esferoidales descubiertas antes del 2005 presentan magnitudes absolutas mayores a $M_v = -8.7$ y luminosidades mayores a 2.5×10^5 $L_\odot$. Sus radios de Pummer son $\gtrsim 200$ pc, a excepción de las galaxias Sextans y Ursa minor, su brillo superficial es de s< 26 mag arcsec^{-2}. Por otro lado, las galaxies enanas esferoidales ultra débiles descubiertas en los últimos años, son por un factor de ~ 1000 menos luminosas, con radios de Plummer de hasta ~ 20 pc y brillo superficial de hasta $\sim 2-3$ mag arcsec^{-2} m más débil que el de Sextans. Las galaxias UFDs son una extensión de las enanas esferoidales,objetos de más pequeños y débiles. Estas galaxies muestran propiedades similares, como población estelar vieja y pobre en metales, formas irregulares y distorsionadas y altas velocidades de dispersión. Podrían ser de las primeras galaxias del Universo temprano por lo que son una interesante prueba de formación de estructuras temprana.

Los escenarios de formación estándar involucran fuertes procesos destructivos que finalmente dejan la forma que vemos hoy. Assmann et al. (2013a) propuso un escenario en donde los cúmulos estelares se forma al interior del halo de materia oscura de una galaxia enana esferoidal. Estos cúmulos presentan una baja formación de estrellas y se disuelven a medida que orbitan al interior del halo. De esa manera construyen el componente luminos que observamos en las galaxias enanas esferoidales.

En nuestro proyecto probamos un posible escenario de formación de galaxias enanas esferoidales para la formación de UFDs. Modelamos Segue 1 mediante el desarrollo de simulaciones numéricas, con un potencial de fondo que imital al halo de materia oscura y las estrellas se encuentran inicialmente en equilibrio virial y ubicadas en una distribución estelar filamentaria, es decir, una distribuci1'on fractal, dentro de un halo analítico, construyendo el débil componente luminoso que observamos. Esperamos con nuestro escenario, usando a Segue 1 como ejemplo, poder reproducir las características estructurales y cinemáticas de las galaxias UFDs que vemos hoy.

TABLE OF CONTENTS

List of Tables

List of Figures

Figure **Page**

CHAPTER 1

THEORY

Although galaxies are important in their own right, they also offer the prospect of providing clues to new laws of physics, for example. The formation of galaxies is intimately related to the properties of the early Universe. Galaxies have frequently been used as enormous laboratories to study the laws of physics in extreme conditions (Binney and Tremaine, 1987).

1.1 Dwarfs Spheroidal Galaxies

Orbiting around the Milky Way, is a large number of satellite galaxies, many of which have low average surface brightness and small effective radii (Vincenzo et al., 2014). Dwarf spheroidal galaxies (dSph) belong to the most numerous galaxy population in the Universe, but their low surface brightness hampers their detection. The Local Group (LG) offers the nearest laboratory to analyse the formation and evolution process of this low-luminosity dSph galaxy population. The historical picture of dSphs, containing relatively little interstellar material, has changed during the past few years owing to the improved spatial resolution and sensitivity of infrared, (sub)millimeter and radio observing facilities (De Looze et al., 2016). They are classified as early-type because they are observed to posses very low gas mass at the present time and their stars are very iron-poor compared to the Sun (Tolstoy et al., 2009; Koch et al., 2008).

> "Nearly all the known satellites, located within the expected virial radius of the bright spirals, at distances smaller than 300 kpc, are classified as dwarf spheroidal galaxies (dSphs)." (Tomozeiu et al., 2016).

Dwarf Spheroidal galaxies are among the least luminous and one of the most dark matter dominated galaxies which are observed today in the Universe.
Color-magnitude diagram (CMD) fitting analysis have revealed star formation histories (SFH)

in dSphs to have been either continuous for a long time or occurring in bursts, but most have singles burst at the beginning. All dSph galaxies host an underlying very old stellar population with age $\gtrsim$ 10 Gyr, and some of them are dominated by an intermediate-age stellar population with age in the range 4-8 Gyr. Very few dSphs have been observed to host younger stars, a sign of a relatively recent star formation activity, which occurred up to ~2-3 Gyr ago.
All these features led cosmologists to hypothesize dSphs to be the evolved small progenitor systems which merged in the past to form the actual large structures in the Universe as the stellar halo, disc and bulge of the Milky Way, in the framework of the ΛCDM standard cosmological model (Vincenzo et al., 2014).
The dSph galaxies are characterized by an absolute magnitude in the range $-13 \leq M_v \leq -9$, their total estimated masses, considering both the stars and the dark matter halo, is of the order of $10^7 - 10^8 M_\odot$, within their half-light radii. The stellar velocity dispersion of the classical dwarf spheroidal is of the order of $10\,\mathrm{km\,s^{-1}}$ and remains approximately constant with distance from the center of the galaxy.

1.1.1 Formation Theory of dSph galaxies

There are several models that attempt to explain the origin of dSph galaxies by considering different mechanisms. Some of them are based on tidal and ram-pressure stripping. There is another model that explains the formation of dwarfs galaxies based on energy and momentum conservation when gas-rich galaxies interact and there are models which consider dwarf galaxies in isolation, but they usually take only a smooth gas distribution into account and focus on higher masses for the dwarfs (Assmann et al., 2013a).

1.1.1.1 Tidal and Ram Pressure Stripping Model

In these models, the dSph galaxies are formed due to the interaction between a rotationally supported dwarf irregular galaxy and a Milky Way sized host galaxy. These models show that dSph galaxies tend to appear near a spiral galaxy, but they do not explain the presence of distant isolated dSph galaxies (Assmann et al., 2013a).
Mayer et al. (2007) proposed the modest potential well of these extreme dwarfs cannot be the one property that determined their nature. Their halo masses are too large to invoke suppression of gas accretion owing to the cosmic ultraviolet background at high redshift, or blow-out due to supernovae winds. Tidal shocks occurring as a dwarf repeatedly approaches the primary galaxy can transform rotationally supported systems resembling dwarf irregular galaxies (dIrrs) into systems dominated by random motions, similar to dSphs. This tidal stirring can explain why dSphs are more clustered around the primary galaxies relative to dIrrs but it leaves a significant gas component inside the dwarf, so that star formation can continue for several billions of years instead of being truncated early. Ram pressure in a hot gaseous corona could strip their gas completely (Mayer et al., 2007).

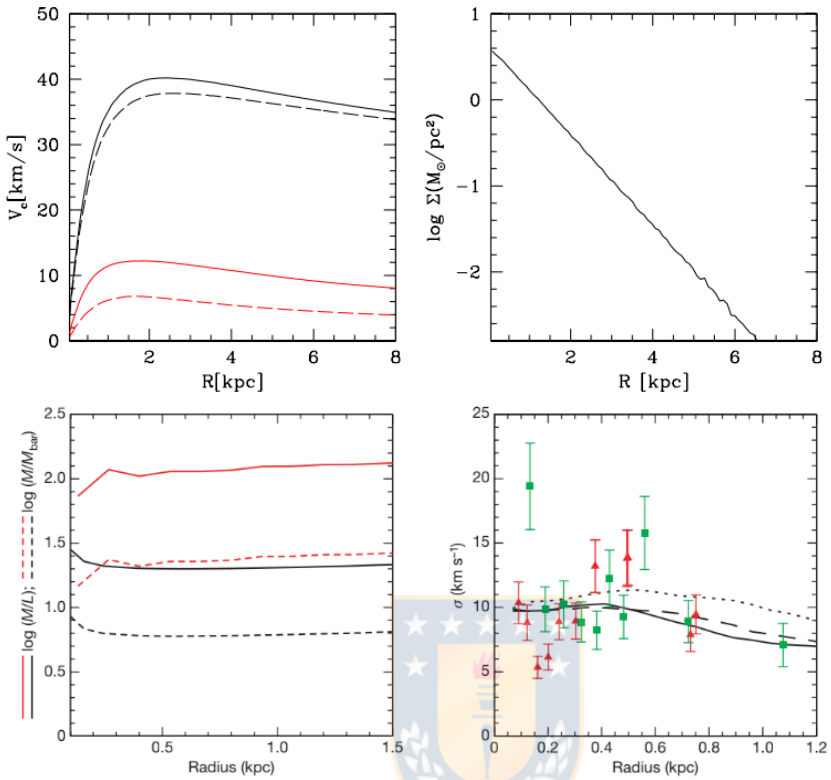

FIGURE 1.1. Structural properties of the initial dwarf galaxy model, and structural properties of the simulated dwarf after 10 billion years of evolution. The top left panel shows the initial rotation curve: the red solid line shows the contribution of the gas, the red dashed line the contribution of the stars, the black dashed line is the dark matter contribution and the black solid line shows the total rotation curve. The top right panel shows the initial baryonic surface density profile. The bottom left panel shows the mass profile out to the radius at which stars are gravitationally bound. The black dashed lines show the initial ratios of the total mass to the baryonic mass and the red dashed line show the final ratios of the total mass to the baryonic mass. The black solid lines show the initial B band mass-to-light ratio of the dwarf and the red solid line show the final B band mass-to-light ratio of the dwarf. They noted that using an initial $M/L_{B^\star} = 1.5$ is motivated by the fact that at $z > 2$ a stellar population is at most three billion years old, whereas a final $M/L_{B^\star} = 5$ is consistent with passive fading of the stellar population for about ten billion years. The bottom right panel shows the line-of-sight stellar velocity dispersion profiles for three random directions (black lines) perpendicular to each other, together with published data points for Draco (red triangles) and Ursa Minor (green squares), including formal 1σ error bars. The curves are shown out to the radius for which data point are available (Mayer et al., 2007). Figure from Mayer et al. (2007).

Mayer et al. (2007) used a high resolution ΛCDM dark-matter only cosmological simulation of the formation of a Milky Way-sized halo and constructed a high resolution N-body+ smoothed particle hydrodynamics (SPH) model of a dwarf galaxy satellite having a disk of stars and gas inside a cold dark matter halo. This model assumes that 80% of the baryonic disk mass is a gas component, the inefficient conversion of gas into stars is expected at these low mass scales since most of the gas will have densities below the threshold for star formation and the dwarf model is placed on an eccentric orbit inside a massive Milky Way-sized halo model which is a replica of that seen in cosmological simulations (see Figure 1.1) (Mayer et al., 2007).

1.1.1.2 Resonant Stripping Model

This model considers a mechanism known as resonant stripping and can be used to explain the formation of isolated dSph galaxies. These objects are formed after encounters between dwarf disc galaxies and large systems, in a process driven by gravitational resonances (Assmann et al., 2013a).

The model proposed by D'Onghia et al. (2009) describes numerical experiments to investigate the consequences of encounters between dwarf galaxies. After 2 billion years nearly ~80% of the stars are stripped away from the smaller dwarf but its surrounding dark matter halo is less strongly affected, leading to a change in the ratio of dark to luminous matter. The stars sit at the bottom of the potential well and therefore comprise the most tightly bound material in the galaxy. This result is caused by a gravitational process called resonant stripping; the resonant stripping can alter the mass to light ratio of dwarfs by removing luminous material more efficiently than dark matter. Figure 1.2 shows the luminous fraction of the smaller dwarf, plotted as a function of time during the interaction with a galaxy 100 times its mass (filled circles), compared to another simulation designed to follow a similar dwarf orbiting the Milky Way today (filled squares) (D'Onghia et al., 2009).

Resonant stripping is most effective for galaxies interacting on prograde orbits; because gravitational torques can alter the internal structure of the galaxies and relative alignments of spin and orbital momenta. Resonant stripping will affect gas and stars in a similar manner in a rotational supported disc and can drive the morphological evolution of dwarfs. When operating in low mass groups, this mechanism can pre-process dwarfs by transforming disk galaxies into spheroids before they are accreted by large galaxies like the Milky Way (D'Onghia et al., 2009).

D'Onghia et al. (2009) shows the dwarf spheroidal galaxies formed in this manner have properties similar to those of dwarfs observed in the Local Group and predicts that dwarf spheroidals should have similar properties in different environments, which is supported by the observed similarities between dwarf spheroidals in the Perseus cluster and those in the Local Group (D'Onghia et al., 2009).

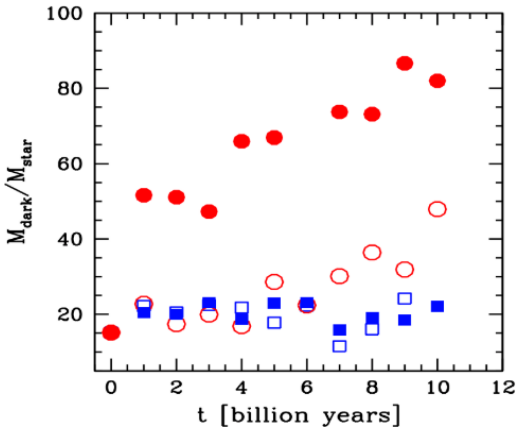

FIGURE 1.2. The time evolution of the dark-to-luminous mass ratio ($M_{\rm DM}/M_{\rm stars}$). The filled red circles represent the dark-mass to luminous ratios, $M_{\rm DM}/M_{\rm stars}$, of the smaller dwarf being resonantly stripped and computed at the tidal radius. The same case but for a mostly retrograde encounters is illustrated by the open red circles. If the orbits are more retrograde, stars are not preferentially removed immediately and after 4 Gyr the internal structure of the smaller dwarf and the orbit are affected by gravitational torques, allowing resonant stripping to occur. The ratio $M_{\rm DM}/M_{\rm stars}$ of the small galaxy orbiting around the Milky Way today is illustrated by the filled blue squares and the retrograde orbits are illustrated by the open blue squares. In both cases, the spin and orbital frequencies of the galaxies are no longer comparable and the resonant interaction is suppressed, even in the prograde case. Figure from D'Onghia et al. (2009).

1.1.1.3 Models in Isolation in big ΛCDM simulations

Sawala et al. (2010) modeled the formation and evolution of dwarfs galaxies with halo masses in the range of $\sim 2\times10^8$ to $10^9 M_\odot$ in fully cosmological, smoothed particle hydrodynamic (SPH) simulations. They simulated a cosmological volume with periodic boundary conditions, in which haloes grow from small density perturbations imposed at high redshift. The numerical model includes metal-dependent cooling, star formation, chemical enrichment, feedback from Type II and Ia supernovae and UV background radiation. This model has resulted in the formation of galaxies similar to the Local Group dwarf spheroidals. They span a wide range in luminosity 6.4×10^4 to $3.4\times10^6 L_\odot$ and median metallicity from $[Fe/H]=-1.83$ to -1.12. The variation in total mass, 2.3 to $11.8\times10^8 M_\odot$, is surprisingly small, but it is comparable to the values inferred from observations in the Local Group. The range of velocity dispersions is $6.5-9.7$ kms^{-1}, but they can not resolve systems as faint as some of the ultra-faint dwarf galaxies (Sawala et al., 2010).

The model proposed by Sawala et al. (2010) finds that the combination of feedback and the cosmic UV background results in the formation of galaxies with properties similar to the Local Group dwarf spheroidals, and that their effect is strongly moderated by the depth of the gravitational

potential, this means, the model can reproduce the observed luminosities and metallicities. Also, their simulations indicate that the evolution of the dwarf galaxies is strongly affected both by the SN feedback and by the UV background radiation, that feedback is necessary to shut down star formation in those haloes, massive and dense enough to cool and forming stars. It is the combination of these two effects that shapes the evolution of the galaxy. Figure 1.3 ilustrates different stages in the evolution of a protogalaxy together with its environment. Feedback heats the gas and blows some of it out during the early stages of the evolution, in the first two columns, the filamentary structure of the environment is still recognizable, together with a number of small haloes that have accumulated gas, but not yet begun star formation. After redshift $z = 6$, UV radiation heats the remaining gas above the haloes virial temperature, quickly removing it from the halo, and it also heats the intergalactic medium. Some gas falls back to the main halo at later times, but does not lead to a significant amount of star formation. Smaller haloes without star formation, and hence not subject to feedback, also lose their gas due to the UV radiation. Where the density of the gas is sufficiently high, they convert gas particles into star particles, having masses of about $10^2 - 10^3 M_\odot$. They do not take into account, that those masses in stars would form in an association or in a small dissolving cluster, because it is below their resolution, nor that more massive star clusters (SCs) could form in a single star-forming event (Assmann et al., 2013a).

1.1.1.4 Dissolving Star Cluster Model

The model proposed by Assmann et al. (2013a) is supported by two widely accepted theories. One of them is the structure formation in the ΛCDM paradigm, here, galaxies form hierarchically in the potential well of dark matter halos and small haloes form first. The second theory describes the star formation inside the galaxies (Lada and Lada, 2003), this theory proposes that stars never form in isolation, but in groups and clusters from slowly forming open clusters and association to intense starbursts, in gas-rich environments, that typically produce a few to a few hundred young star clusters, within a region of just a few hundred pc.
The dissolving star cluster model proposes that the dynamical evolution of these SCs, that is, their dissolution due to the gas expulsion, may explain the formation of classical dSphs galaxies, including all their irregularities in the stellar kinematic distribution as well as surviving SCs around them. The SCs form with low star formation efficiency (SFE) and, thus, are designed to dissolve inside the dark matter halo to form the luminous component of the dSph galaxy (Assmann et al., 2013a,b). Their major result is that even 10 Gyr of evolution is not enough to erase substructures stemming from their formation process. These substructures are mainly visible in velocity space (see Figure 1.4).
External structural remnants of the formation process are very faint. The central structures which are within 500 pc have observable luminosities comparable to the luminosity of the dSph galaxies of the Milky Way.

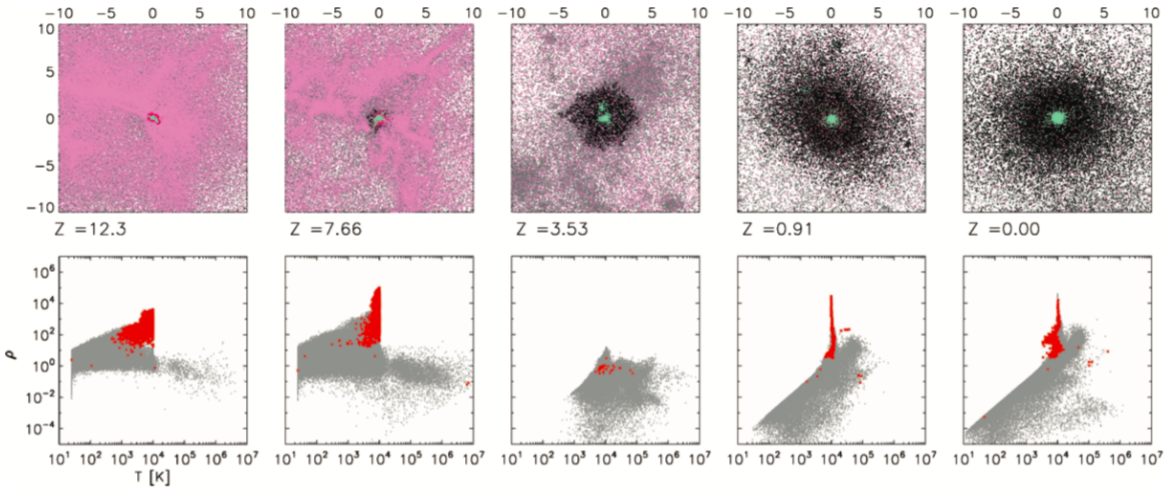

FIGURE 1.3. Different stages in the evolution of a protogalaxy together with its environment, both SN feedback and UV radiation are included. The top row shows the spatial distribution of particles at different redshift, i.e., shows the positions of dark matter, gas and star particles. Dark matter particles are shown in black or grey, gas particles in red or pink, depending on whether they are bound to the object in the centre, or whether they are part of the other haloes or the intergalactic medium. Star particles are shown in green. The bottom row shows the distribution of the gas particles on the density-temperature plane, i.e., the temperature and density of gas particles, both within and outside of the most massive halo. Red dots indicate gas that is bound to the central halo, while grey dots are for particles in all other parts of the simulates volume. It can be seen that the central halo is almost gas free at redshift $z = 3.5$, due to the combined effect of feedback and the UV background. Figure from Sawala et al. (2010)

Velocity dispersion is around $10\,\mathrm{km\,s^{-1}}$ and has a flat velocity dispersion profile in projection. This resembles closely the observations of the known classical dwarfs.

In continuation Alarcón Jara et al. (2018) add different star formation histories (SFHs) to the dissolving star cluster model. Their main result is that independent of the used SFH the general finding, i.e., the ability to reproduce the shapes and luminosities of the dSph galaxies, remain the same.

They obtain dSph galaxies, showing exponential surface brightness profiles and flat velocity dispersion curves in the range of 5 to 12 km $\mathrm{s^{-1}}$. Using the same distribution scale-length they obtain more concentrated objects when using cusped haloes than in the case of the cored haloes. Figure 1.5 shows a set of some characteristics of the final object. Left column shows the shape of the final object with colour bars for the magnitude for surface brightness. The central column represent the radial surface brightness profile, measured in concentric rings and the right column

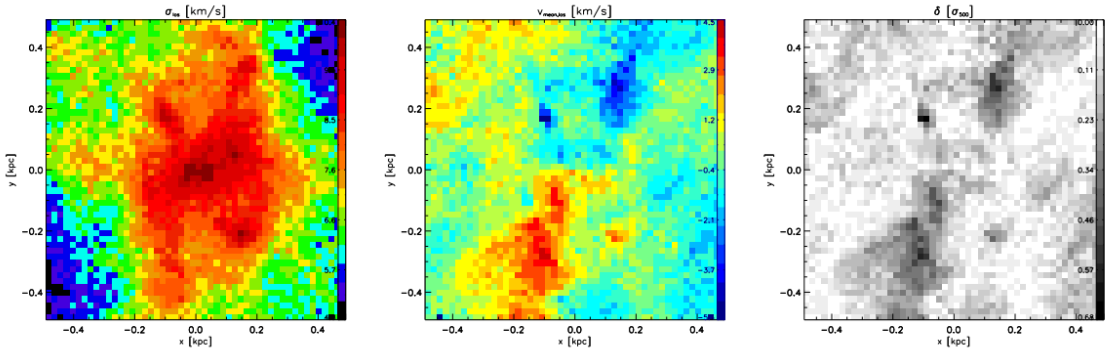

FIGURE 1.4. The 2D velocity structure. Show the dynamics of the realization within 500 pc as two-dimensional pixel maps with resolution of 20 pc. In the left-hand panel it shows the line-of-sight velocity dispersion calculated for each pixel separately. Is possible see regions of high velocity dispersion of more 10 $\mathrm{km}s^{-1}$ in the central area and more substructure. The middle panel show the mean velocity of all particles within a pixel, the figure shows even after 10 Gyr of evolution we still see the stars of dissolved Scs. The right-hand panel shows the δ parameter $\left(\delta \equiv \frac{|v_{mean}|}{\sigma_{500}}\right)$. Figure from Assmann et al. (2013a).

shows the radial velocity dispersion profile, measured in concentric rings. It is possible to note a wide range of different outcomes from the simulations, all with properties like the classical dSph galaxies of the Milky Way. The top panel shows a nearly spherical final object in which all the SCs have dissolve. The middle panel shows a very elongated final object in which all the SCs have dissolved, but some of them had similar orbital planes causing a flattened profile and the bottom panel shows a double-cored final object with two high-density peaks in the centre.
Alarcón Jara et al. (2018) deduce that the SCs inside the DM haloes have formed with low SFEs (<30 per cent) and most likely in a cusped DM profile as predicted by ΛCDM. They show this formation scenario works even with different SFHs, DM profiles and SFEs, to dissolve the SCs and not only reproduce the observational data, also provide observers with predictions for future observations.

1.2 Ultra-Faint Dwarf Spheroidal Galaxies

The dwarf spheroidal galaxies (dSphs) in the Milky Way subgroup offer a unique opportunity to investigate galaxy formation and evolution by studying the photometric properties of the resolved stellar populations (Okamoto et al., 2011). Since 2005, the Sloan Digital Sky Survey (SDSS) has discovered a large number of new dwarf galaxies orbiting around the Milky Way. Ultra-faint dwarf spheroidal galaxies are about 10-100 times fainter than the classical dSphs galaxies, present

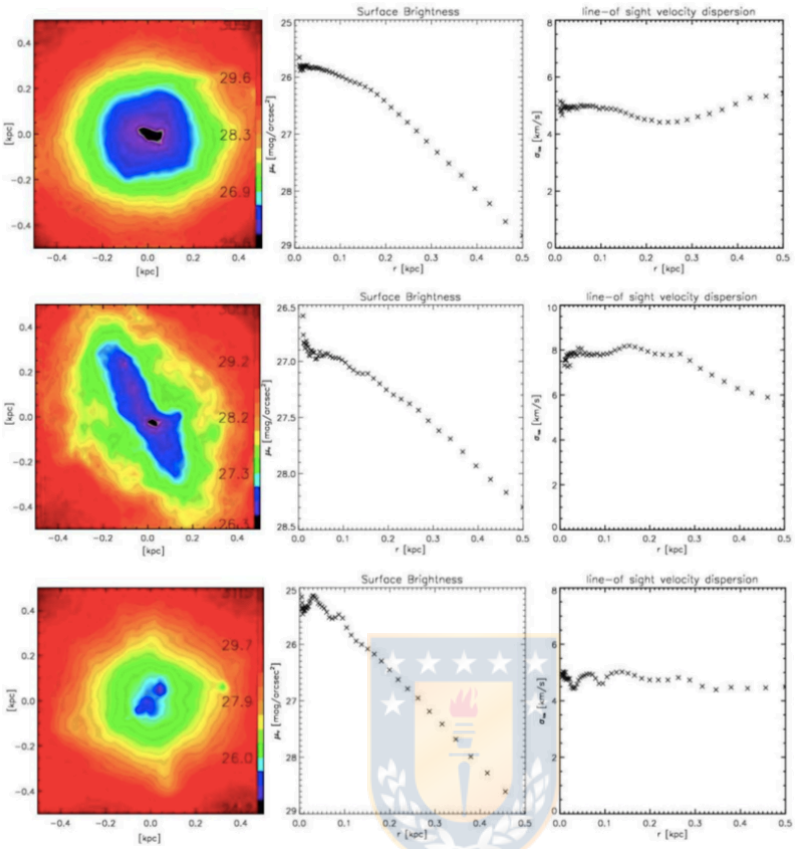

FIGURE 1.5. Characteristics of the final object inside a radius of 500pc: Show a wide range of different outcomes from the simulations, all with properties like the classical dSph galaxies of the Milky Way. Left column shows the shape of the final object with colour bars for the magnitud for surface brightness. The central column represent the radial surface brightness profile , measured in concentric rings and the right column shows the radial velocity dispersion profile, measured in concentric rings. The top panel shows a nearly spherical final object in which all the SCs have dissolve, with a linear SFH, SFE= 20 per cent and Navarro, Frenk & White (NFW) profile. The middle panel shows a very elongated final object in which all the SCs have dissolved, but some of them had similar orbital planes causing a flattened profile, has a quadratic SFH, SFE= 20 per cent and a cored DM halo. The bottom panel shows a double-cored final object with two high-density peaks in the centre, with a constant SFH, SEF= 30 per cent and NFW halo. Figure from Alarcón Jara et al. (2018)

extremely low surface brightness, luminosities smaller than $\sim 1000 L_{\odot}$, extremely metal-poor populations and are the most dark matter (DM) dominated systems known.

UFDs galaxies do not contain any gas at the present time, and their stars are on average very iron-poor with ages $\gtrsim 10-12$ Gyr., and may be the only galaxies where star formation ended in the earliest epoch of the Universe (Vincenzo et al., 2014; Tollerud et al., 2011).

For decades, only about a dozen dwarf galaxies were known to orbit the Milky Way; the majority of these systems correspond to dSphs galaxies, which are the least luminous, but, by number, the dominant galaxy type in the present-day Universe (Brown et al., 2012). A new population of dwarf galaxies in the Local Group, known as ultra-faint dwarfs (UFDs) appears to be an extension of the classical dSphs with very similar physical properties (see Figure1.7). They have only been discovered relatively recently, after the advent of deep, wide-area photometric surveys like the Sloan Digital Sky survey (SDSS), the Panoramic Survey Telescope and Rapid Response System (Pan-STARRS) and the Dark Energy Survey (DES), which found several low brightness satellites of the Milky Way (Ji et al., 2019; Nagasawa et al., 2018). Figure 1.6 maps the distribution of all known SDSS ultra-faint satellites on the Galactic sky until 2013 (upper panel). These SDSS objects all lie at high galactic latitude, as the survey is concentrated around the North Galactic Pole. Bottom panel shows the sky distribution of previously known satellites of the Milky Way with the classical dwarfs and 32 new candidate dwarfs until 2018.
Though at first it was unclear whether such objects were dwarf galaxies or globular clusters (GCs) (Willman et al., 2005a), UFDs are now understood to be the natural result of galaxy formation in small dark matter halos in standard ΛCDM cosmology. Theoretically, these galaxies begin forming at $z \sim 10$ in small ($\sim 10^8 M_\odot$) dark matter halos. Supernova (SN) feedback is specially effective in these small galaxies, so they form stars inefficiently for $1-2$ Gyr before their star formation is quenched by reionization. All observed properties of UFD are also consistent with this (Ji et al., 2019). Subsequent spectroscopic surveys of these system reveal kinematics and metallicities in line with those of dwarf galaxies (Muñoz et al., 2010).
These systems are thus good laboratories in which to constrain cosmological models. Conn et al. (2018) proposed these objects will provide crucial empirical input for testing cosmology predictions and verifying formation scenarios of the MW, for example a way of solving the missing satellite problem. Galaxy formation simulations assume (Brown et al., 2012):

1. UFDs formed the bulk of their stars prior to the epoch of reionization.

2. Mechanism that could drive an early termination of stars formation include: reionization, gas depletion and supernova feedback.

Current mass estimations for ultra-faint dwarfs are based on the assumption that the dynamical state of these systems has not been influenced significantly by Galactic tides, and therefore that they are near dynamical equilibrium.
One of the remaining questions related to their discovery is whether these galaxies formed intrinsically with such low luminosities, or whether they were born as brighter objects and attained their current luminosities through tidal mass loss (Muñoz et al., 2010).

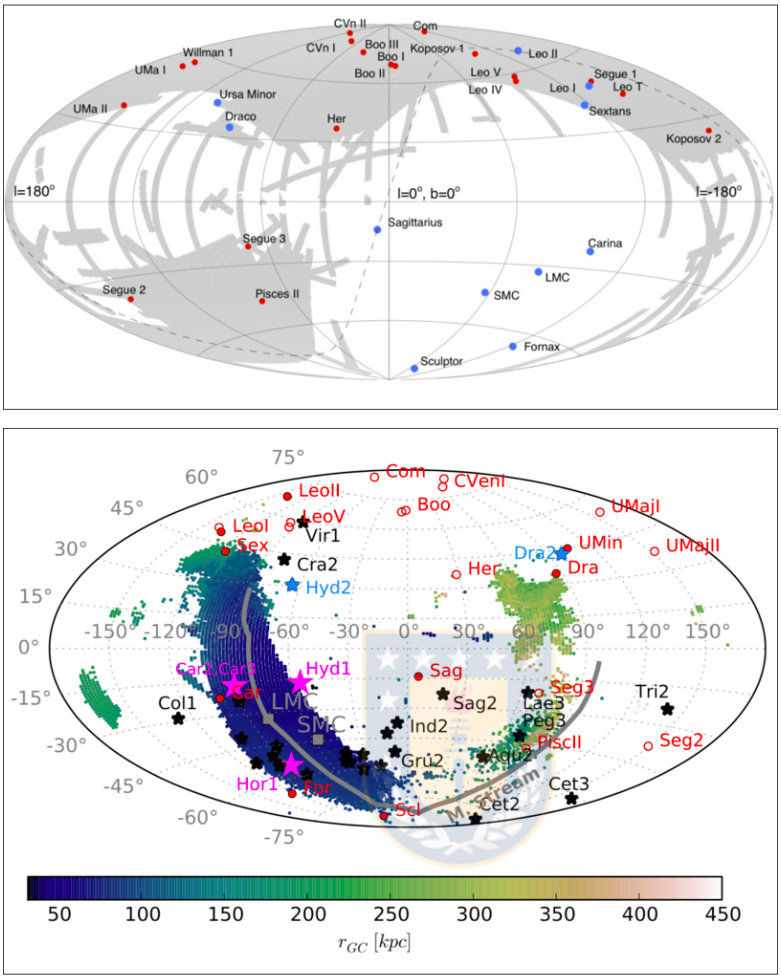

FIGURE 1.6. Distribution of known satellites, classical and ultra-faint dwarf. Upper panel shows the distribution until 2013 of the classical dwarf galaxies (blue circles) and the SDSS ultra-faint satellites (red circles). The SDSS DR8 imaging footprint is shown in gray. Dashed line show the orbit of the Sgt dwarf galaxy. Figure from Belokurov (2013). Bottom panel shows the sky distribution of previously known satellites of the Milky Way (red circles) with the classical dwarfs (filled red circles) and 32 new candidate dwarfs (star symbols) until 2018. The thick gray color shows the location of the Magellanic Stream and the color bar represents the distance gradient. Figure from Kallivayalil et al. (2018)

1.2.1 Solving the Missing Problem?

One of the primary quest of astronomy is understanding the formation of structure in the Universe. In this regard, the Lambda Cold Dark Matter (ΛCDM) cosmological models are consistent and in agreement with many observable phenomena, but some discrepancies are found on small scales. Specifically, this model predicts many more dark-matter sub-halos, a factor of 50, than the number of observed dwarf galaxies (Moore et al., 1999; Francois et al., 2016). The ΛCDM

cosmological model predicts that massive galaxies such as the Milky Way should be surrounded by large number of dark matter halos. The relatively modest populations of observed dwarf galaxies orbiting the Milky Way and Andromeda, however, seem to be in conflict with this prediction (Moore et al., 1999; Klypin et al., 1999). The fact that the number of DM halos in the LG predicted by ΛCDM simulations is much larger than the number of observed Galactic satellites has become widely known as the "substructure crisis" or "missing dwarf" problem (Simon and Geha, 2007). Proposed solutions to the substructure problem can be broadly divided into two categories: cosmological and astrophysical. Cosmological solutions include modifying the power spectrum at small scales and changing the properties of the dark matter particles, such as by making them warm or invoking a late decay from a non-relativistic particle. Astrophysical solutions are more common, but perhaps easier to constrain observationally. Some of the most popular astrophysical solutions include the hypothesis that reionization could suppress the formation of dwarf galaxies by preventing low-mass dark matter halos from acquiring enough gas to form stars after $z \sim 10$ and the possibility that the dwarf galaxies we observe today were once much more massive objects that have been reduced to their present appearance by dramatic tidal stripping (Simon and Geha, 2007).

As one way of rectifying this problem, Bullock et al. (2000) put forth the idea that reionization could have suppressed star formation in the smallest dark matter sub-halos, essentially by boiling the gas out of their shallow potential wells. The dearth of stars would make these sub-halos difficult or impossible to detect. Building upon this hypothesis, Ricotti and Gnedin (2005) proposed that dwarf galaxies could follow one of three evolutionary paths: true fossils that formed most of their stars prior to reionization, polluted fossils with star formation continuing beyond reionization, and survivors that largely formed their stars after reionization (Brown et al., 2014). In 2007, Simon and Geha (2007), having established the masses of the ultra-faint dwarfs, re-examine the missing satellite problem, and after correcting for the sky coverage of the SDSS , they find that the ultra-faint dwarfs substantially alleviate the discrepancy between the predicted and observed numbers of satellites around the Milky Way, but there are still a factor of ~ 4 too few dwarf galaxies over a significant range of masses. Thus, they show that if galaxy formation in low-mass dark matter halos is strongly suppressed after reionization, the simulated circular velocity function of CDM sub-halos can be brought into approximate agreement with observed circular velocity function of Milky Way satellite galaxies (Simon and Geha, 2007). Each model will be discussed in more detail in section 1.2.3.

1.2.2 Characteristics and Properties

UFDs are satellites of the MW that are highly dark-matter dominated, with total luminosities of $L_\star \approx 10^3 - 10^5 L_\odot$, discovered in deep wide-are sky surveys. Based on a color-magnitude diagram analysis, Brown et al. (2014) found that nearly three-fourths of the entire stellar mass content of such galaxies is formed by $z \approx 10$ and $\sim 80\%$ of the stellar mass content is already formed by

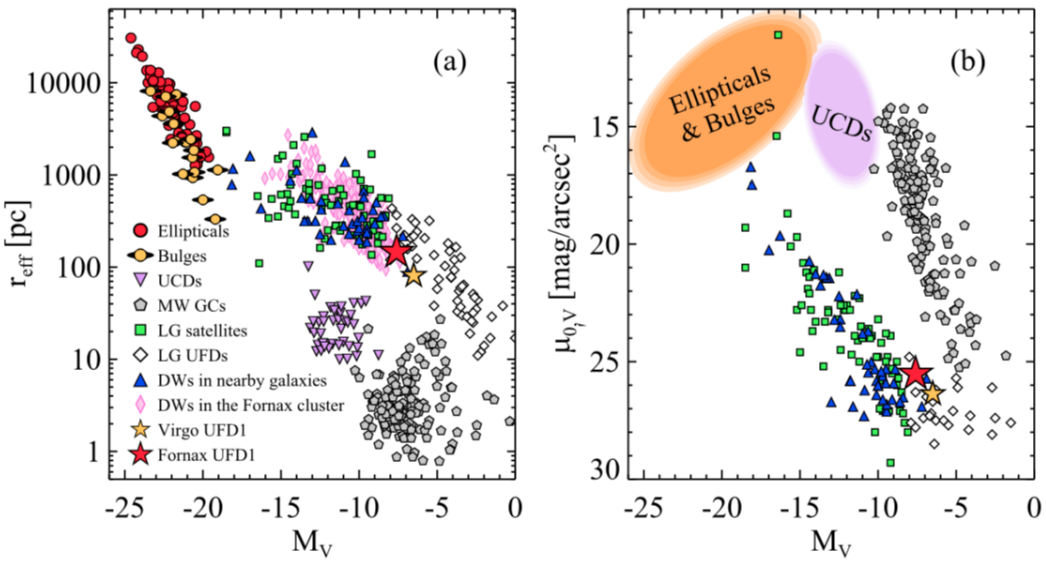

FIGURE 1.7. Comparison of effective radius $r_{\rm eff}$, total magnitudes, $M_{\rm v}$, and central surface brightness, $\mu_{0,{\rm v}}$, of different stellar systems. Circles and lenticular symbols are for the giant ellipticals and bulges in spiral galaxies, downward triangles for the ultra-compact dwarfs (UCDs), pentagons for the Milky Way globular cluster, squares and empty diamonds for the Local Group satellites and UFDs and upward triangles for the dwarfs in M81 and M106. Left panel shows the effective radius as a function of the absolute V total magnitude. Right panel shows the $V-$band central surface brightness vs. absolute V total magnitude. Figure from Lee et al. (2017).

$z \approx 6$ (Safarzadeh et al., 2019). These ultra-faint dwarfs are the oldest, most metal-poor, and least chemically evolved stellar systems known. They therefore provide unique windows into the formation of the first galaxies and the behavior of dark matter on small scales.

The search for faint dwarf galaxies has been a nearly continuous endeavor since the serendipitous discovery of the first such system, Sculptor, by Shapley (1938). As significantly deeper survey data became available, systematic searches for more dwarfs slowly revealed what are now known as the classical dwarf spheroidal satellites of the Milky Way. However, after the identification of Sextans by Irwin et al. (1990), the push to ever lower luminosities and surface brightness stalled for more than a decade. New efforts to find faint, low surface brightness Milky Way dwarf galaxies continued fruitlessly in this period. Though, there were strong theoretical reasons to expect that dwarfs with substantially lower luminosities and surface brightness should exist. This prediction proved resoundingly correct in 2005, when the first such object were discovered in Sloan Digital Sky Survey imaging by Willman et al. (2005a,b). These results opened the floodgates, and within two years the known population of Milky Way satellite galaxies more than doubled. Over the following decade, new discoveries continued at a rapid pace in SDSS and other surveys, such that the Milky way satellite census has now doubled yet again (see Figure 1.8). Now have a

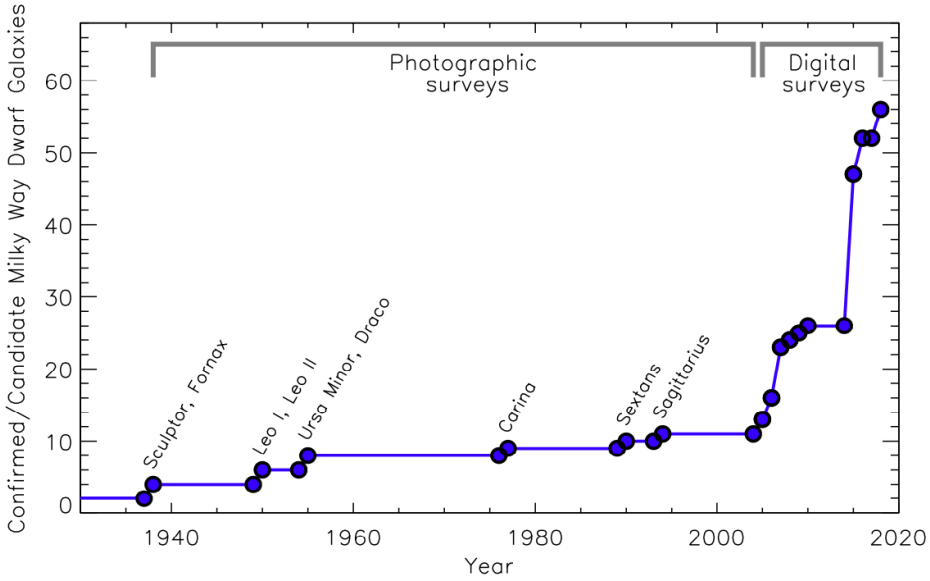

FIGURE 1.8. Milky Way satellite galaxies as a function of the time. The major discovery impact of SDSS (2005-2010) and DES/Pan-STARRS (2015), each of which approximately doubled the previously known satellite population. Figure from Simon (2019).

general understanding of the properties of these systems and their place in galaxy evolution and cosmology.

While the faintest dwarf galaxies resemble globular clusters in some ways, when the population of low luminosity stellar systems is considered as a whole it is clear that they are galaxies rather than star clusters:

1. The stellar kinematics of UFDs galaxies demonstrate that they contain significant amounts of dark matter.

2. All but the very lower-luminosity UFDs have physical extents larger than any known clusters.

3. Within each UFD, the abundances of Fe and $\alpha-$elements exhibit substantial spreads resulting from extended star formation and internal chemical enrichment.

4. UFDs follow a luminosity metallicity relationship, while globular clusters do not.

5. The abundances of certain elements in UFDs are similar to those in brighter dwarfs, and do not resemble the light element chemical abundance correlations seen in globular clusters.

Several aspects of the UFDs make them critical objects to understand, with potentially wide-ranging implications. First, UFDs reside in the smallest dark matter haloes yet found . While

only the mass at the very center of the halo is currently measurable, the extrapolated virial masses of the UFDs are $\sim 10^9\,M_\odot$ (e.g., Strigari et al., 2008), and the halo masses at the time when the stars formed may have been $\sim 10^8\,M_\odot$ (e.g., Safarzadeh et al., 2018). UFDs are also the most dark-matter dominated systems known. This combination of small halo mass and negligible baryonic mass make UFDs extremely valuable laboratories for constraining the nature of dark matter. The measured central densities perhaps eventually the density profiles, of UFDs provide significant clues to the behavior of dark matter on small scales. Second, the UFDs represent the extremely limit of the galaxy formation process. They have the lowest metallicities, oldest ages, smallest sizes, smallest stellar masses, and simplest assembly histories of all galaxies. Both, observational and theoretical models indicate that UFDs formed at very high redshift, probably before the epoch of reionization. These objects therefore present us with a unique window into the conditions prevalent at the time where the first galaxies were forming (Simon, 2019).

1.2.2.1 Defining Ultra Faint Dwarf as galaxies

The dwarfs galaxies known prior 2005 have absolute magnitude brighter than $M_v = 8.7$, corresponding to V-band luminosities larger than $2.5 \times 10^5\,L_\odot$. Their Plummer (half-light) radii are $\gtrsim 200\,pc$, and with the exception of Sextants and Ursa Minor, their central surface brightness are $< 26\,mag\,arcsec^{-2}$. In contrast, the dwarfs discovered in SDSS and other modern surveys are up to a factor of ~ 1000 less luminous, with half-light radii as small as $\sim 20\,pc$ and surface brightness that can be $\sim 2-3\,mag\,arcsec^{-2}$ fainter than that of Sextans. The ultra-faint dwarfs continuously extend the properties of more luminous dwarfs in stellar mass, surface brightness, size, dynamical mass, and metallicity. They are not a physically distinct class of objects, UFDs represent the extreme end of the distribution of galaxy properties, while classical dSphs can already be identifies and studied in other nearby groups of galaxies, the UFDs are special in that only the very brightest examples of such systems will be detected beyond the Local Group in the foreseeable future. Finally it is tempting to suggest that UFDs might differ from classical dSphs in that their star formation was shut off by reionization at $z \gtrsim 6$ instead of continuing to lower redshift. Based on this dwarf galaxies with absolute magnitudes fainter than $M_v = -7.7\,(L = 10^5\,L_\odot)$ are considered UFDs.

Prior to the discovery of dwarf galaxies fainter than $M_v \sim -5$, dwarfs and globular cluster occupied distinct and cleanly separated portions of the size-luminosity parameter space. Conn et al. (2018) dubbed the region occupied by a number of ultra-faint satellites ($14 < r_{1/2} < 25\,pc$) the trough of uncertainty to emphasize the difficulty in classifying these systems. In order to resolve the confusion caused by the lack of an agreed-upon systems for separating galaxies from stars clusters, Willman and Strader (2012) proposed the following definition:

> "A galaxy is a gravitationally bound collection of stars whose properties cannot be explained by a combination of baryons and Newton's laws of gravity."

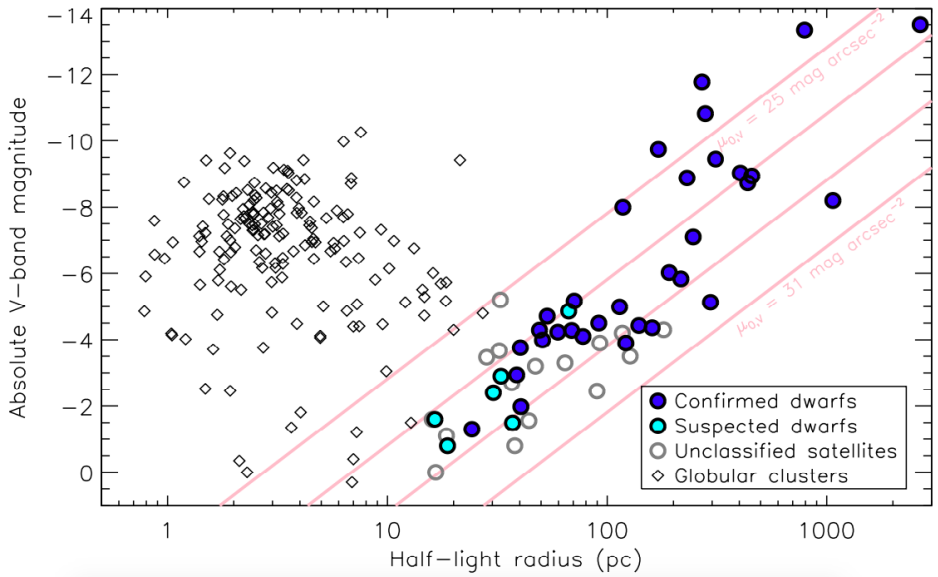

FIGURE 1.9. Distribution of the Milky way satellites in absolute magnitude (M_v) and half-light radius. Dark blue filled circles represent the confirmed dwarf galaxies and objects suspected to be dwarf galaxies but for which the available data are not conclusive are shown as cyan filled circles. Dwarf galaxies without any published classification are shown as open gray circles. The faint candidates with $R_{1/2} \gtrsim 50$ pc are almost certainly dwarf galaxies, but are not include in the confirmed category given the currently available observations. The black diamonds represent the Milky Way's globular cluster. Lines if constant central surface brightness (at 25, 27,29, and 31 mag arcsec^{-2} in V band) are plotted in pink (Simon, 2019). Figure from Simon (2019).

Applied to UDFs, this definition is generally interpreted as requiring an object to have either a dynamical mass significantly larger than its baryonic mass or non-zero spread in stellar metallicities to qualify as a galaxy. The former criterion directly indicates the presence of dark matter, while the latter indirectly suggests that the object must be embedded in a dark matter halo massive enough that supernova ejecta can be retained for subsequent generation of stars formation.

1.2.2.2 Stellar kinematics

One of the first step in clarifying the nature of the UFDs was to determine their stellar velocity dispersion, by measuring the velocities of individual stars in several systems, these early studies constrained their dynamical masses and dark matter content (Simon, 2019). Until 2007 there was a significant correlation of velocity dispersion, σ, with absolute magnitude, M_v, with the more luminous galaxies ($M_v \lesssim -6$) having larger dispersions of $\sim 7-8\,\mathrm{km\,s^{-1}}$ and the fainter

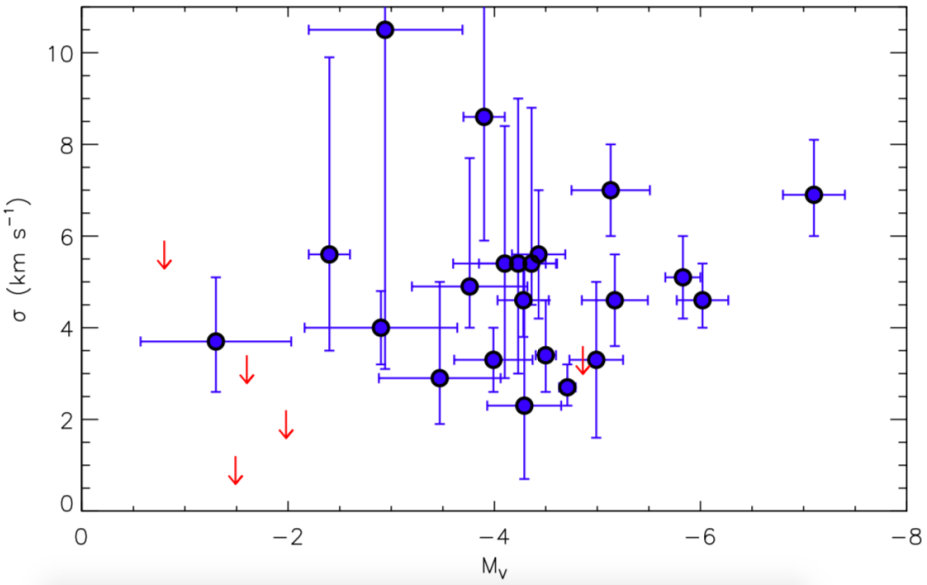

FIGURE 1.10. Line-of-sight velocity dispersion of ultra-faint Milky Way satellites as a function of absolute magnitude. Measurements and uncertainties are shown as the blue points with error bars, and 90% confidence upper limits are displayed as red arrows for systems without resolved velocity dispersion (Simon, 2019). Figure from Simon (2019).

galaxies ($M_V \gtrsim -6$) exhibiting smaller dispersions of $\sim 4-5\,\mathrm{km\,s^{-1}}$. Four low-luminosity galaxies Coma Berenices, Canes Venatici II, Hercules and Leo IV were the first galaxies to break the velocity dispersion barrier at $\sim 7\,\mathrm{km\,s^{-1}}$. The unprecedentedly low velocity dispersions of these galaxies and the correlation with absolute magnitude down to such low luminosity demonstrate that if there is a floor on the masses of dSphs, it does not appear to have been reached yet (Simon and Geha, 2007), demonstrating that UFD can not be purely baryonic systems.
At the present, velocity dispersion measurements or limits have been obtained for 27 out 42 confirmed or candidate UFDs (see Figure 1.10).

1.2.2.3 Metallicities and chemical abundances patterns

The metallicities of stars in UFDs are important both for classifying them as galaxies and for connecting them to the broader field of galaxy formation.
The first spectroscopic metallicity measurements for ultra-faint dwarfs were provided by Simon and Geha (2007); Muñoz et al. (2006); Martin et al. (2007). Collectively these studies showed that the ultra-faint dwarfs have very low metallicities ([Fe/H] $\lesssim -2$) and that the stars in each object span a range in metallicity, and indicates that stars formation in these objects extended for a long enough period of time for supernova (SN) enrichment to occur and their gravitational

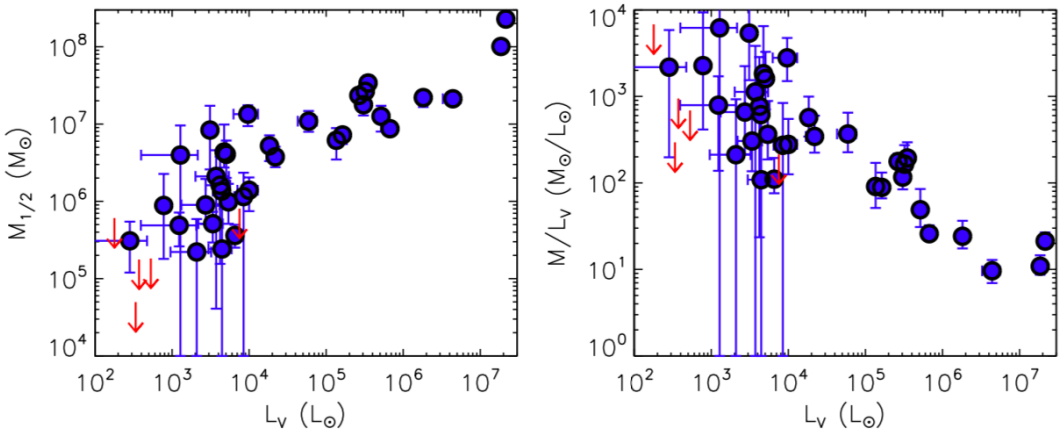

FIGURE 1.11. The dynamical masses of ultra-faint Milky Way satellites as a function of luminosity are shown in the left panel and the mass-to-light ratios within the half-light radius for ultra-faint Milky Way satellites as function of luminosity are shown in the right panel. Measurements and uncertainties are shown as the blue points with error bars, and mass limits determined from 90% confidence upper limit on the dispersion are displayed as red arrows for systems without resolved velocity dispersion (Simon, 2019). The confirmed ultra-faint dwarf galaxies included in this plot are listed in Table 1.2. Figure from Simon (2019).

TABLE 1.1. Ultra-Faint dSph Metallicities. The table shows the number of analyzed stars, mean [Fe/H], the rms dispersion in [Fe/H] and the distribution of signal-to -noise (S/N). Table from Kirby et al. (2008).

dSph	N	$\log(L/L_\odot)$	$\langle$[Fe/H]$\rangle$	$\sigma_{[Fe/H]}$	log(S/N)
UMa II	12	3.6 ± 0.2	-2.44 ± 0.06	0.57	1.5 ± 0.4
Leo T	19	5.1 ± 0.3	-2.02 ± 0.05	0.54	1.1 ± 0.2
UMa I	28	4.1 ± 0.1	-2.29 ± 0.04	0.54	1.5 ± 0.3
Leo IV	12	3.9 ± 0.2	-2.58 ± 0.08	0.75	1.3 ± 0.3
Com	24	3.6 ± 0.2	-2.53 ± 0.05	0.45	1.5 ± 0.3
CVn II	16	3.9 ± 0.2	-2.19 ± 0.05	0.59	1.5 ± 0.1
CVn I	165	5.4 ± 0.1	-2.08 ± 0.02	0.46	1.3 ± 0.3
Herc	22	4.6 ± 0.1	-2.58 ± 0.04	0.51	1.6 ± 0.4

potential is deep enough that not all of the supernova eject can escape the system. Kirby et al. (2008) showed that many of the ultra-faint dwarfs contain extremely metal-poor (EMP) star with [Fe/H] < -3, again distinct form globular clusters and classical dSphs (see Table1.1).

Brown et al. (2014) proposed a composite color-magnitude diagram (CMD) for six ultra-faint galaxies (Hercules, Leo IV, Canes Venatici II, Ursa Major I, Bootes I and Coma Berenices), the CMDs all appear extremely similar to each other, implying the population ages and metallicities are also similar. Figure 1.12 shows the composite CMD for six galaxies, each shifted to the

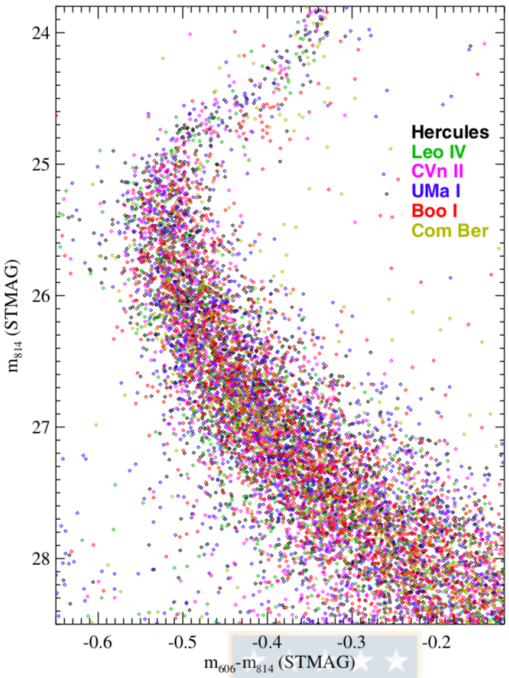

FIGURE 1.12. Color magnitude-diagram of six UFD (color points) focused on main-sequence and sub-giant branch. The similarities of six CMDs imply that the UFD populations are extremely similar in age and metallicities. Figure from Brown et al. (2014).

same distance and reddening, and focused on the CMD region most sensitive to age, i.e., the Main Sequence turnoff and sub-giant branch. Each UFD appears to be dominated by an ancient metal-poor population and has a similar star formation history (SFH). An appropriate object to use as a reference is the Galactic globular cluster M92, one of the most ancient and metal-poor stellar systems known. The globular cluster with little extinction and well studied population and age of 13.2 Gyr, has served as a reference population in different studies of UFDs (Brown et al., 2014)

It appears likely that UFDs are uniformly ancient, with all or nearly all of their stars forming in the early Universe. While most or all UFDs exhibit a blue plume of stars brighter than the main sequence turnoff, this population is best interpreted as blue stragglers rather than young stars. These objects can thus be considered as pristine fossils from the era of reionization. Improved age measurements reveal how synchronized the star formation in such galaxies was would be very interesting. Conversely, a clear detection of younger stars in very low-luminosity dwarfs would have important implications for stars formation in low-mass dark matter halos and perhaps for cosmology as well (Simon, 2019).

UFDs are particularly appealing systems in which to study early chemical evolution and nucleosynthesis because their small stellar masses imply that they have hosted relatively few SN

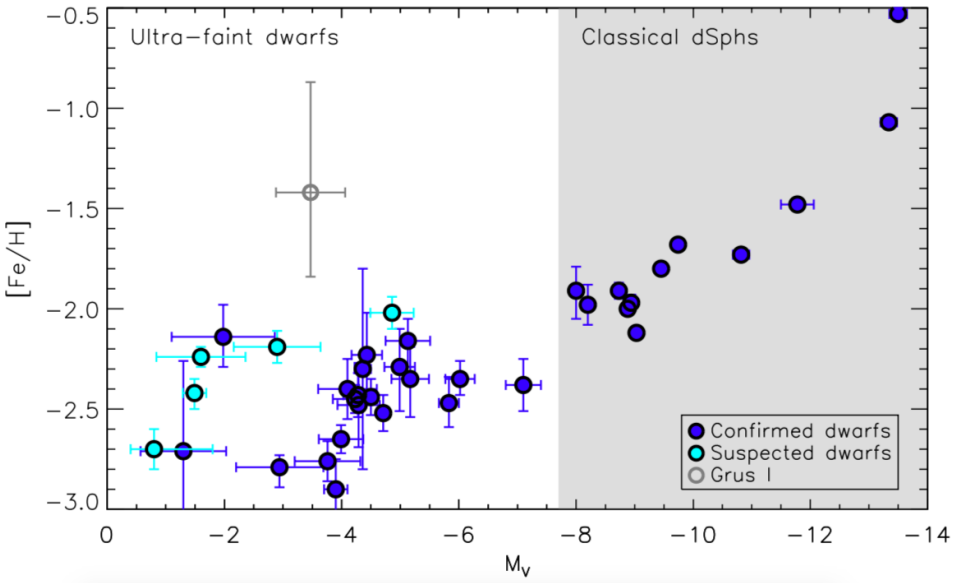

FIGURE 1.13. Mean stellar metallicities of the Milky Way satellites as a function of absolute magnitudes. Confirmed dwarf galaxies are displayed as dark blue filled circles, and objects suspected to be dwarf galaxies but for which the available data are not conclusive are shown as cyan filled circles. Grus I, for which there is no published classification, is shown as an open gray circle. The error bars in the vertical direction indicate the uncertainty on the mean metallicity of each object (Simon, 2019). Figure from Simon (2019).

explosions. That fact, combined with the short time periods during which they were forming stars, means that UFDs may preserve the unpolluted chemical signatures of small numbers of nucleosynthetic events, perhaps even individual explosions. It was clear that the UFDs are enhanced in α elements such as oxygen, magnesium, calcium, and silicon, and unusually deficient in neutron-capture elements including barium and strontium.

1.2.2.4 Structural properties

Martin et al. (2008) provide a homogeneous analysis of the structural properties of the early SDSS UFDs, shown that the radial profiles of ultra-faint dwarfs can be accurately described by either exponential or Plummer profiles. Muñoz et al. (2018) advocate instead for Sérsic profiles, which match the observed radial profiles more closely. Confirmed UFDs have half-light radii ranging from 24 pc (Segue 1) to 295 pc (UMa I), with candidate UFDs extending down to 15 − 20 pc in a few cases. In comparison, the classical dSphs have half-light radii between 170 pc (Leo II) to 2660 pc (Sagittarius).

It has been suggested that the faintest galaxies have significantly larger ellipticities than larger systems, with an average ellipticity for UFDs of 0.50 ± 0.01, while the weighted average ellipticity

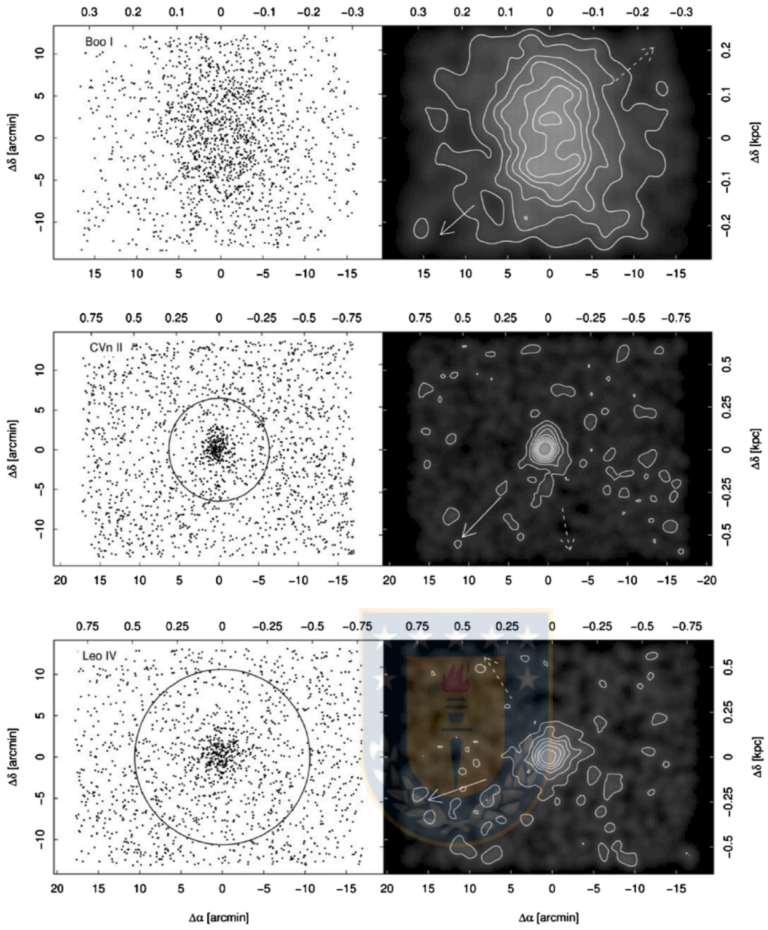

FIGURE 1.14. Spatial distribution of the member candidates selected from each CMD (left) and the isodensity contour maps of the member candidates (right) of UFDs. The solid and dashes arrows indicated the direction of Galactic center (Sgr A) and Galactic latitude toward the disk, respectively. The upper panel show the spatial distribution of Boö I, the middle panel show the spatial distribution of CVn II and the lower panel show the spatial distribution of Leo IV and the tidal radii of CVn II and Leo IV dSphs are shown as solid lines. Figure from Okamoto et al. (2011).

of the classical dSphs is 0.350 ± 0.003, in good agreement with the statistics determined by Martin et al. (2008). But Simon (2019) concluded that there is no significant evidence at present that UFDs have more elongated shapes than more luminous dwarfs.

A reoccurring question regarding the structure of the faintest dwarfs is whether their isophotes are irregular or distorted in any way, which could suggest, e.g., recent tidal stripping (Okamoto et al., 2011; Zucker et al., 2006). Several analyses of simulated photometric data sets of faint dwarfs have shown that these apparently irregular shapes are the result of Poisson fluctuations

in the distribution of stars in the lowest surface brightness regions of these systems rather than evidence for disturbed morphology (Muñoz et al., 2010; Martin et al., 2008). Figure 1.14 shows the spatial distribution and the density contour maps of UFDs, which show various morphologies. Boö I show elongated and distorted shapes, CVn II has a relatively high concentration, while Leo IV shows a smooth and less concentrated spherical shape (Okamoto et al., 2011).
Simon (2019) proposes the following 21 satellites (see Table 1.2 for different properties of confirmed UFDs) can be regarded as spectroscopically confirmed ultra-faint dwarf galaxies: Segue 2, Hydrus 1, Hologorium I, Rectuculum II, Eridanus II, Carina II, Ursa Major II, Segue 1, Ursa Major I, Willman 1, Leo V, Leo IV, Coma Berenices, Canes Venatici II, Boötes II, Boötes I, Hercules, Pegasus III, Aquarius II, Tucana II and Pisces II (see Table 1.2) and the satellites that may be dwarfs but for which either no spectroscopy has been published or the data are inconclusive include: Tucana IV, Cetus II, Cetus III, Triangulum II, DES J0225+0304, Hologorium II, Recticulum III, Pictor I, Columba I, Pictor II, Carina III, Virgo I, Hydra II, Draco II, Sagittarius II, Indus II, Grus II, Grus I, Tucana V, Phoenix II and Tucana III.

TABLE 1.2. Properties of ultra-faint dwarf Spheroidal Galaxies. Table from Simon (2019)

UFD	M_v	$R_{1/2}$ [pc]	Distance [kpc]	v_{hel} [km s^{-1}]	σ [km s^{-1}]	[Fe/H]	$\sigma_{[Fe/H]}$
Segue 2	$-1.98^{+0.88}_{-0.88}$	40^{+4}_{-4}	$-37.0^{+3.0}_{-3.0}$	$-40.2^{+0.9}_{-0.9}$	< 2.2	$-2.14^{+0.16}_{-0.15}$	$0.39^{+0.12}_{-0.13}$
Hydrus I	$-4.71^{+0.08}_{-0.08}$	53^{+4}_{-4}	$27.6^{+0.5}_{-0.5}$	$80.4^{+0.6}_{-0.6}$	$27^{+0.5}_{-0.4}$	$-2.52^{+0.09}_{-0.09}$	$0.41^{+0.08}_{-0.08}$
Horologium I	$-3.76^{+0.56}_{-0.56}$	40^{+10}_{-9}	$87.0^{+13.0}_{-11.0}$	$112.8^{+2.5}_{-2.6}$	$4.9^{+2.8}_{-0.9}$	$-2.76^{+0.10}_{-0.10}$	$0.17^{+0.20}_{-0.03}$
Reticulum II	$-3.99^{+0.38}_{-0.38}$	51^{+3}_{-3}	$31.6^{+1.5}_{-1.4}$	$62.8^{+0.5}_{-0.5}$	$3.3^{+0.7}_{-0.7}$	$-2.65^{+0.07}_{-0.07}$	$0.28^{+0.09}_{-0.09}$
Eridanus II	$-7.10^{+0.30}_{-0.30}$	246^{+17}_{-17}	$366.0^{+17.0}_{-17.0}$	$75.6^{+1.3}_{-1.3}$	$6.9^{+1.2}_{-0.9}$	$-2.38^{+0.13}_{0.13-}$	$0.47^{+0.12}_{-0.09}$
Carina II	$-4.50^{+0.10}_{-0.10}$	92^{+8}_{-8}	$36.2^{+0.6}_{-0.6}$	$477.2^{+1.2}_{-1.2}$	$3.4^{+1.2}_{-0.8}$	$-2.44^{+0.09}_{-0.09}$	$0.22^{+0.10}_{-0.07}$
Ursa Major II	$-4.43^{+0.26}_{-0.26}$	139^{+8}_{-8}	$34.7^{+2.0}_{-1.9}$	$-116.5^{+1.9}_{-1.9}$	$5.6^{+1.4}_{-1.4}$	$-2.23^{+0.21}_{-0.21}$	$0.67^{+0.20}_{-0.15}$
Segue 1	$-1.30^{+0.73}_{-0.73}$	24^{+4}_{-4}	$23.0^{+2.0}_{-2.0}$	$208.5^{+0.9}_{-0.9}$	$3.7^{+1.4}_{-1.1}$	$-2.71^{+0.45}_{-0.39}$	$0.95^{+0.42}_{-0.26}$
Ursa Major I	$-5.13^{+0.38}_{-0.38}$	295^{+28}_{-28}	$97.3^{+6.0}_{-5.7}$	$-55.3^{+1.4}_{-1.4}$	$7.0^{1.0+}_{-1.0}$	$-2.16^{+0.11}_{-0.13}$	$0.62^{+0.10}_{-0.08}$
Willman 1	$-2.90^{+0.74}_{-0.74}$	33^{+8}_{-8}	$45.0^{+10.0}_{-10.0}$	$-14.1^{+1.0}_{-1.0}$	$4.0^{+8.0}_{-8.0}$	$-2.19^{+0.08}_{-0.08}$	—-
Leo V	$-4.29^{+0.36}_{-0.36}$	49^{+16}_{-16}	$169.0^{+4.0}_{-4.0}$	$170.9^{+2.1}_{-1.9}$	$2.3^{+3.2}_{-1.6}$	$-2.48^{+0.21}_{-0.21}$	$0.47^{+0.23}_{-0.13}$
Leo IV	$-4.99^{+0.26}_{-0.26}$	114^{+13}_{-13}	$154^{+5.0}_{-5.0}$	$132.3^{+1.4}_{-1.4}$	$3.3^{+1.7}_{-1.7}$	$-2.29^{+0.19}_{-0.22}$	$0.56^{+0.19}_{-0.14}$
Coma Berenices	$-4.28^{+0.25}_{-0.25}$	69^{+5}_{-4}	$42.0^{+1.6}_{-1.5}$	$98.1^{+0.9}_{-0.9}$	$4.6^{+0.8}_{-0.8}$	$-2.43^{+0.11}_{-0.11}$	$0.46^{+0.09}_{-0.08}$
Canes Venatici II	$-5.17^{+0.32}_{-0.32}$	71^{+11}_{-11}	$160.0^{+4.0}_{-4.0}$	$-128.9^{+1.2}_{-1.2}$	$4.6^{+1.0}_{-1.0}$	$-2.35^{+0.16}_{-0.19}$	$0.57^{+0.15}_{-0.12}$
Boötes II	$-2.94^{+0.74}_{-0.74}$	39^{+5}_{-5}	$42.0^{+1.0}_{-1.0}$	$-117.0^{+5.2}_{-5.2}$	$10.5^{+7.4}_{-7.4}$	$-2.70^{+0.06}_{-0.10}$	< 0.35
Boötes I	$-6.02^{+0.25}_{-0.25}$	191^{+8}_{-8}	$66.0^{+2.0}_{-2.0}$	$101.8^{+0.7}_{-0.7}$	$4.6^{+0.8}_{-0.6}$	$-2.35^{+0.09}_{-0.08}$	$0.44^{+0.07}_{-0.06}$
Hercules	$-5.83^{+0.17}_{-0.17}$	216^{+20}_{-20}	$132.0^{+6.0}_{-6.0}$	$45.0^{+1.1}_{-1.1}$	$5.1^{+0.9}_{-0.9}$	$-2.47^{+0.13}_{-0.12}$	$0.47^{+0.11}_{-0.08}$
Pegasus III	$-4.10^{+0.50}_{-0.50}$	78^{+31}_{-25}	$2.5.0^{+20.0}_{-20.0}$	$-222.9^{+2.6}_{-2.6}$	$5.4^{+3.0}_{-2.5}$	$-2.40^{+0.15}_{-0.15}$	—-
Aquarius II	$-4.36^{+0.14}_{-0.14}$	160^{+26}_{-26}	$107.9^{+3.3}_{-3.3}$	$-71.1^{+2.5}_{-2.5}$	$5.4^{+3.4}_{-0.9}$	$-2.30^{+0.50}_{-0.50}$	—-
Tucana II	$-3.90^{+0.20}_{-0.20}$	121^{+35}_{-35}	$58.0^{+8.0}_{-8.0}$	$-129.1^{+3.5}_{-3.5}$	$8.6^{+4.4}_{-2.7}$	$-2.90^{+0.15}_{-0.16}$	$0.29^{+0.15}_{-0.12}$
Pisces II	$-4.23^{+0.38}_{-0.38}$	60^{+10}_{-10}	$183.0^{+15.0}_{-15.0}$	$-226.5^{+2.7}_{-2.7}$	$5.4^{+3.6}_{-2.4}$	$-2.45^{+0.07}_{-0.07}$	$0.48^{+0.70}_{-0.29}$

1.2.3 Formation Models of UFD galaxies

The origin of UFDs is a matter of ongoing debate. Several solutions have been suggested so far to resolve the crisis. It is common for galaxy formation models to alleviate the missing satellite problem by truncating the star formation in dark matter halos below some nominal mass threshold, sometimes termed the "filtering mass", with this threshold tuned to match the observations (Brown et al., 2014). Since, one of the main challenges facing standard hierarchical structure formation models is that the predicted abundance of Galactic subhalos with circular velocities $v_c \sim 10-30\ \mathrm{km\,s^{-1}}$ is an order of magnitude higher than the number of satellites actually observed within the Local Group (Bullock et al., 2000).

1.2.3.1 Reionization scenario

Bullock et al. (2000) proposed that dSph galaxies in the LG formed during the pre-reionization era, and processes of the photoinization feedback resulted in the suppression of star formation below the observable level in 90% of the low-mass dark matter halos populating the LG (Ricotti and Gnedin, 2005). They investigated the abundances of satellite galaxies.
Their main result is that the theoritical velocity function for visible satellites is consistent with that observed and that the total number of observable systems is ~ 10% of the total dark halo abundance. The reason for this difference is that most of the halos form after reionization. The observable satellites are within halos that formed early, corresponding to rare, high peaks in the initial density field (Bullock et al., 2000).
The reionization scenario is prompted by the fact that almost all local group dSphs exhibit a prominent old population and a decline of their star formation rates about 10 Gyr ago. While in the standard ΛCDM theory stellar reionization took place 12.5 Gyr ago (Ricotti and Gnedin, 2005), so, they concluded that the observed abundances of satellite galaxies may be explained in the ΛCDM scenario if galaxy formation in low-mass halos is suppressed after the epoch of reionization, provided that $z \lesssim 12$ (Bullock et al., 2000).

1.2.3.2 Reionization fossil scenario

Ricotti and Gnedin in 2005, based on Bullock's hypothesis, who suggested that gas accretion in low-mass halos could be suppressed by the photo-ionization mechanism during the reionization of the Universe (Bullock et al., 2000), proposed that dSphs are fossils of galaxies with mass $M_{\mathrm{DM}} < 10^8 M_\odot$ that formed before reionization, while dwarf irregular galaxies (dIrrs) formed later in more massive halos. They find instead that these galaxies do form, and at the epoch of their formation, they closely resemble dSphs. Also, they show that reionization feedback is not the dominant mechanism that suppresses star formation in most low mass halos. But, the goal of this scenario is to provide evidence in support of the primordial origin of dSphs by comparing the abundant observational data on LG dwarfs with the results of detailed numerical simulations of

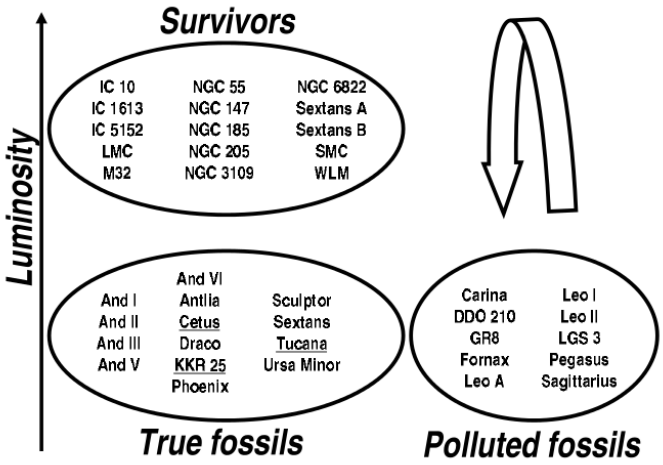

FIGURE 1.15. Tentative separation of all Local Group dwarfs. Ricotti & Gnedin on 2005 proposed that dwarf galaxies could be classified in three different classes depending on the occurrence of their star formation relatively to the reionization event: survivors, which formed via the tidal scenario, true fossils, which formed via the reionization scenario, and polluted fossils, which went through both stages. Figure from Ricotti and Gnedin (2005).

formation of dwarf galaxies in the pre-reionization era (Ricotti and Gnedin, 2005). The core of the reionization scenario is that some of the LG dwarfs are true fossils of the pre-reionization era. Clearly, not all dwarfs fall into this category, since many of them had recent episodes of star formation. Figure 1.16 shows the low-luminosity dwarfs appear to trace the same distribution as the simulated galaxies, having smaller core radii as the central luminosity density increases.
The reionization scenario proposes that dwarf galaxies of the LG were formed in three different evolutionary paths, (see Figure 1.15):

1. True fossils: formed most of their star in the pre-reionization era, and have had little ($< 30\%$) star formation since then. Living in the oldest dark matter halos of their mass, are highly biased and are also preferentially located closer to the center of the parent halo.

2. Polluted fossil: started as true fossils but had substantial episodes of subsequent star formation as they continued accreting mass and were tidally shocked during the formation of the parent galaxy halo. They formed a significant fraction of their stars in the pre-reionization era and exceeded the local filtering mass at some point in their history.

3. Survivors: They started forming stars mostly after reionization and have central luminosities generally comparable to dwarf elliptical galaxies, but less concentrated light profiles.

We can see some of results in Figure 1.16 such a comparison for the basic structural parameters. Luminosity L_v, core radius r_c and central luminosity density I_c. From the top panel of the figure

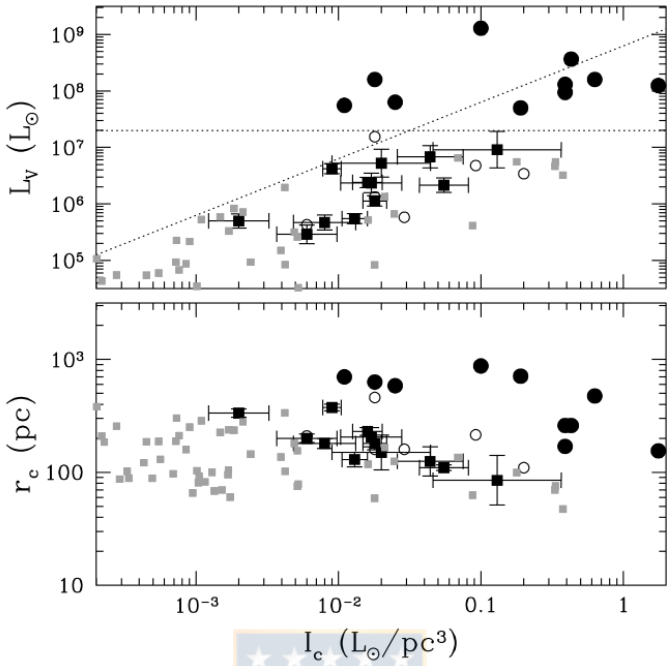

FIGURE 1.16. Comparison for the basic structural parameters : The luminosity L_v, the core radius r_c and the central luminosity density I_c. V-band luminosity (top) and core radius (bottom) vs the central luminosity density for the Local Group dwarfs: **true fossils**, squares with error bars; **polluted fossils**, open circles and **survivors**, filled circles. And gray squares for the simulated galaxies passively evolved to $z = 0$. Two dotted lines show two possible boundaries between the fossils and survivors. From the top panel it is clear that the simulated galaxies do not exceed about $10^7 L_\odot$. Moreover, it appears that the observed galaxies also fall into two groups: those with luminosities on the order of $10^7 L_\odot$ and below, and those with luminosities in excess of $5 \times 10^7 L_\odot$. The bottom panel shows, their core radii are somewhat larger than those of the simulated galaxies. Figure from Ricotti and Gnedin (2005).

it is clear that the simulated galaxies (gray squares) do not exceed about $10^7 L_\odot$. Ricotti and Gnedin (2005) contend that the observed metallicity spreads are not necessarily an indicator of star formation extending over several Gyr. In their simulations all dwarfs that form before reionization have metallicity spreads consistent with observations, but the reionization fossil scenario would not produce a correlation between UFDs and orbital distances, but could explain the existence of UFDs at large distances from the primaries, like Leo T.

1.2.3.3 Tidal stirring of disky dwarfs

Lokas et al. (2012) are using a suite of collisionless N-body simulations to investigate the formation of UFDs in the context of the tidal stirring model for the formation of dwarf spheroidal

galaxies in the Local Group. This simulations are designed to reproduce the tidal interactions between MW-sized host galaxies and rotationally supported dwarfs embedded in $10^9 M_\odot$ dark matter halos, with different inner densities slopes. The dark matter density profiles have the form:

$$\rho(r) = \frac{\rho_{\rm char}}{\left(\frac{r}{r_{\rm s}}\right)^{\alpha}\left(1+\frac{r}{r_{\rm s}}\right)^{3-\alpha}}$$

whit an asymptotic inner $r^{-\alpha}$ and a outer slope r^{-3} and two free parameters, the characteristic density $\rho_{\rm char}$ and $r_{\rm s}$.

They built three different galaxies with very similar properties and the same virial mass of $M_{\rm vir} = 10^9 M_\odot$ and concentration parameter $c = r_{\rm vir}/r_{\rm s} = 20$, but different α, which requires slightly different values of the characteristic density $\rho_{\rm char}$. They chose $\alpha = 1$ (NFW profile) and two shallower inner slopes, namely a mild cusp with $\alpha = 0.6$ and a core-like profile with $\alpha = 0.2$. The dark matter halos were populated with stellar disks of mass given as a fraction, m_d of $M_{\rm vir}$, with $m_d = 0.02$. The disk radial scale length was equal to $z_d/R_d = 0.2$, where z_d denotes the vertical disk scale height. A constant value for the central radial velocity dispersion $\sigma_{\rm R0} = 10\,{\rm kms}^{-1}$ for all dwarf models was assumed.

Each dwarf galaxy model contained $N_h = 10^6$ dark matter and $N_d = 5\times10^5$ disk particles with a gravitational softening of $\epsilon_h = 60$ pc and $\epsilon_d = 20$ pc, respectively. Each galaxy was placed on five different bound orbits R_1 to R_5 inside the primary galaxy, each orbit with different size and eccentricity. The apocenters $r_{\rm apo}$ and pericenters $r_{\rm per}$, given in kpc, are $R_1(125,25)$, $R_2(85,17)$, $R_3(250,50)$, $R_4(125,12.5)$ and $R_5(125,50)$. The dwarfs were initially placed at the apocenters and the evolution was followed for 10 Gyr. Figure 1.17 shows the different properties of progenitors dwarf models resulting in dwarf galaxies with DM density profile (upper panel) with significantly different shapes, different circular maximum velocities $V_{\rm max}$ (middle panel) and binding energy of the stars (lower panel) as an other key factor that determines their response to the tidal shocks. All dwarfs galaxies undergo mass loss, their morphology changes from a disk to a triaxial and then to a more spherical shape, and the stellar rotation is transformed into random motions. The degree of this changes it is proportional to the total tidal force experienced by the dwarfs, but also depends on the structural properties of the progenitors.

Dwarfs with shallower cusps are more susceptible to changes, they loss mass more effectively, and are thus more easily destroyed. In particular, dwarfs with the standard NFW cusps of $\alpha = 1.0$ survive until the end of the simulations for all orbits, while dwarfs with the shallowest inner profile with $\alpha = 0.2$ are dissolved completely for the tighter orbits R_1, R_2 and R_4 after 4, 3 and 2 pericenter passages, respectively. The destruction of these dwarfs occur rather early in the evolution, when the dwarfs are still quite massive. On the other hand, the intermediate cusp of $\alpha = 0.6$ leads to a longer survival, but the dwarfs become much smaller in size.

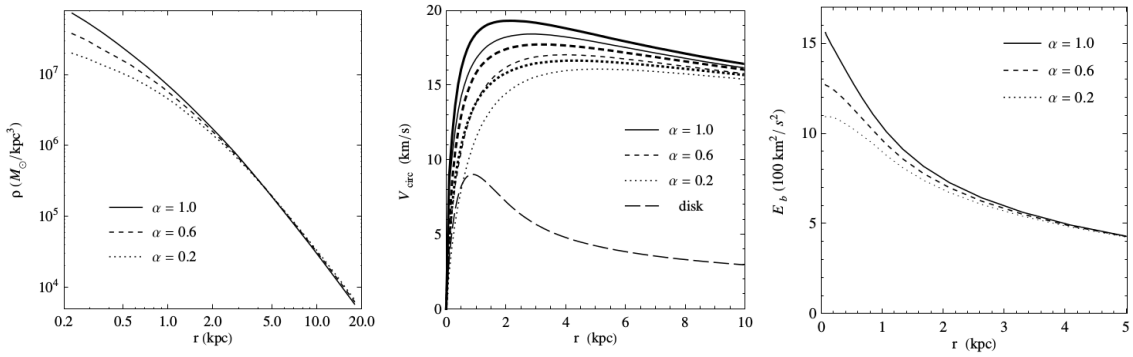

FIGURE 1.17. Different properties of progenitors dwarfs models. Dependence of the initial properties of the adopted dwarf models on the inner slope α. Left panel: the dark matter density profiles, have significantly different shapes in the region occupied by the bulk of the stellar component ($\lesssim$ 2kpc). Middle panel: circular velocities profiles, the disk, halo (thin lines) and total (thick lines). With different maximum circular velocities $V_{\rm max}$ = 19.6, 17.8 and 16.7kms^{-1}, respectively, for α = 1.0, 0.6 and 0.2. Right panel: the binding energy of the stars per unit mass. Figure from Lokas et al. (2012)

TABLE 1.3. Values of all the observational parameters of the two simulated UFDs with $\alpha = 0.6$ on orbits R_2 and R_4: The initial apo- and pericenter distances of these orbits, $r_{\rm apo}$ and $r_{\rm peri}$, their orbital times, $T_{\rm orb}$, number of apocenters after which the dwarfs are identify, $N_{\rm apo}$ and times when these last apocenters took place from the start of simulations are listed in the first five rows respectively and the last four rows correspond to the luminosity of the dwarf at each apocenter, $L_{\rm v}$, visual magnitud, $M_{\rm v}$, central surface brithness of the dwarf follows from the average number of the stars measured in three directions, $\mu_{\rm v}$ and half-light radius after fitted each profile with the Plummer formula, $r_{1/2}$. Table from Lokas et al. (2012)

Parameter	R_2	R_4
$r_{\rm apo}$ [kpc]	85	125
$r_{\rm peri}$ [kpc]	17	12.5
$T_{\rm orb}$ [Gyr]	1.3	1.8
$N_{\rm apo}$	6	6
$T_{\rm la}$ [Gyr]	6.4	9.3
L_v [$10^3 L_\odot$]	6.38	4.84
M_v [mag]	−4.68	−4.38
μ_v [mag arcsec^{-2}]	28.3	28.7
$r_{1/2}$ [kpc]	0.166	0.137

The model with an intermediate cusp of $\alpha = 0.6$, leads to a longer survival, but the dwarf becomes much smaller in size, on orbits R_2 and R_4 which leads to the formation of dSph galaxies with properties akin to those of UFDs in the vicinity of the Milky Way (see Table 1.3).

Using collision-less N-body simulations, this model demonstrates that the tidal stirring of $\sim 10^9\,M_\odot$ disky dwarfs for a period of ~ 8 Gyr can lead to the formation of stellar systems with properties akin to those of UFDs around the Milky Way. UFDs are produced when the progenitor disky dwarfs are placed on relatively tight ($r_{\rm peri} \lesssim 20$ kpc), eccentric ($r_{\rm apo}\,/\,r_{\rm peri} \gtrsim 5$) orbits inside an Milky Way-sized host and are embedded in Dark Matter halos with a mild central density cusp ($\rho \propto r^{-0.6}$).

The simulations produce UFDs with $M_v > -5$ mag, $\mu_v = 28-29$ mag arsec^{-2} and $r_{1/2} = 0.1-0.2$ kpc. These observational properties are very similar to those of the observed population of Milky Way. Thus, the key difference between the reionization and tidal hypotheses is whether most of the stars in a given dwarf galaxy formed in halos of mass $\lesssim 10^8\,M_\odot$ before reionization ($z > 6, 12.5-13$ Gyr ago) or in more massive halos after reionization, during the epoch of formation of the Milky Way and Andromeda ($z \sim 2-3$, $10-11$ Gyr ago) (Lokas et al., 2012).

1.3 This Work

We perform numerical simulations using the Astrophysical Multipurpose Software Environment (AMUSE) (Section 2.2) to study a star formation scenario for ultra-faint dwarf dSPh galaxies. We aim we proposed an alternative formation channel, in continuation to our Dissolving Star Cluster model (Subsection 1.1.1.4) for classical dSph galaxies. We study a formation scenario with a strong background potential mimicking the dark matter halo. Our stars are initially in virial equilibrium and placed in a filamentary stellar distribution, a fractal distribution, within an analytical halo, building the faint luminous component that we observe. We follow their evolution for 5 Gyr.

This work is divided as follows. In Chapter 2 we show the methods that we employ to generate the initial distribution of stars and the software used to run the simulations. In Chapter 3 we show the observational data of Segue 1 and the set-up that we employ to generate the fractal distribution and the dark matter halo, their initial masses, number of particles and radius. In Chapter 4 we study the effects in the variation in the initial parameters over the final object and present a summary of the results. Finally in Chapter 5 we present our conclusions.

CHAPTER 2

CODES TO USE

Astrophysical simulations have become an indispensable tool to understand the formation and evolution of astrophysical systems. Problems ranging from planet formation to stellar evolution and from the formation of galaxies to structure formation in the Universe have benefited from the development of sophisticated codes that can simulate the physics involved (Pelupessy et al., 2013).

2.1 Fractal Generator

Goodwin and Whitworth (2004) investigated the evolution of initially fractal star cluster to see how long substructure can survive, in which the density substructure is correlated with coherent velocity dispersion, as would be expected in clusters where sub-clusters form from distinct molecular cores. The models include star clusters with large velocity dispersion and the fractal provides a simple, one-parameter description of clumpiness.

Fractal distributions are generated by defining a cube with side 2, and placing a parent at the centre of the cube, then, the cube is divided into $N_{\rm div}^3$ equal sub-cubes, and a child is placed at the centre of each sub-cube (first generation). This method defines a cube of size $N_{\rm div} = 2$, of which the fractal is created and in which case there are 8 sub-cubes and 8 first-generation children. Each sub-cube, called child, can turn into a parent for the next generation with the probability of $N_{\rm div}^{(D-3)}$, where D is the fractal dimension, and the probability to become a parent is clearly ruled by the value of the fractal dimension (see Figure 2.1):

- $D < 3$: Less children turn to parents so a more sub-structured distribution is produced.
- $D = 3$: Correspond to an uniform distribution of the particles.

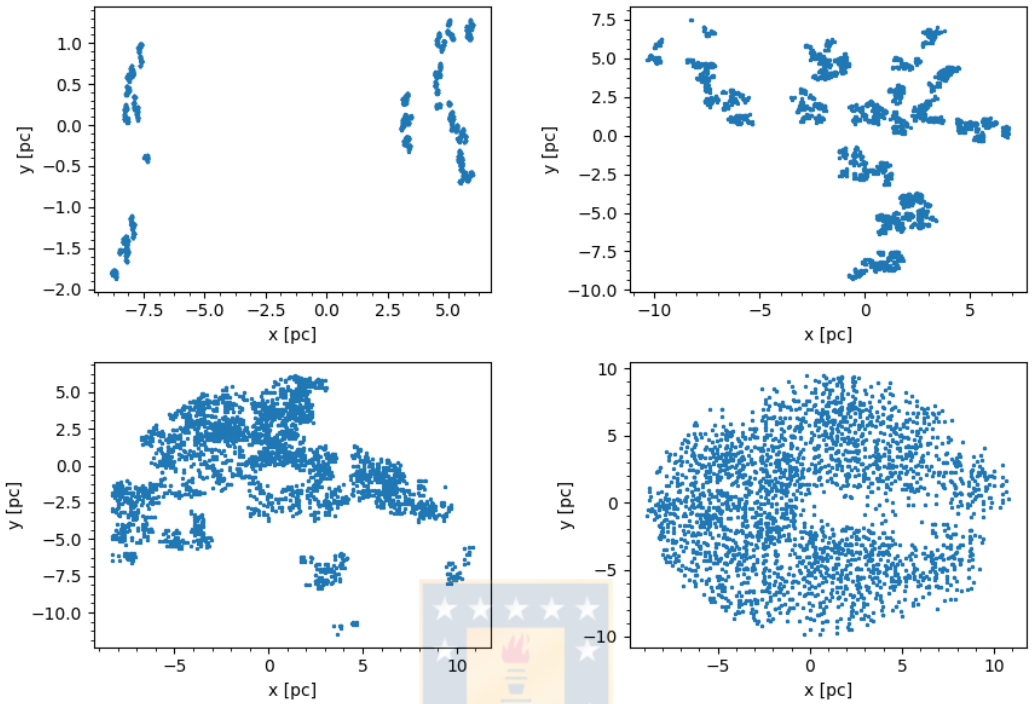

FIGURE 2.1. Examples of initial sub-structured distribution of 3000 particles for different fractal dimensions. Top left panel: fractal distribution with a fractal dimension $D = 1.0$. Top right panel: fractal distribution with a fractal dimension $D = 1.6$. Bottom left panel: fractal distribution with a fractal dimension $D = 2.0$. Bottom right panel: fractal distribution with a fractal dimension $D = 3.0$ (uniform distribution).

- $D > 3$: For high D often a binary cluster is formed with two major sub-clusters.

Children that do not mature are deleted, along with the parent. A little noise is then added to the positions of the remaining children, to avoid a gridded structure, and they become parents of the next generation, each one spawning $N_{\rm div}^3$ children (second generation) at the centres of the $N_{\rm div}^3$ equal-volume sub-sub-cubes, and each second-generation child having a probability $N_{\rm div}^{(D-3)}$ of maturing to become a parent. This process is repeated until the number of children reaches a larger number than the number of particles.

The velocities of the children are inherited of the parents including a random component that decreases with each new generation. The velocities of the parents follow a Gaussian with a mean of zero and the children inherent the velocity from the parent including a random component that decreases with each new generation. These velocities are then scaled so that the virial ratio α has the prescribed value, α is defined as the ratio of the total kinetic energy k, to the magnitude

of the gravitational potential energy, Ω:

$$\alpha = \frac{k}{|\,\Omega\,|}$$

Depending of the value of α important information of the global processes occurring in the star cluster can be derived:

- $\alpha = 0.1$: Corresponds to a cluster which immediately collapse.
- $\alpha = 0.5$: Corresponds to virial equilibrium.
- $\alpha = 0.75$: Corresponds to a super-virial cluster (i.e. one which has just expelled its residual gas).
- $\alpha \geq 1.0$: Corresponds to an unbound object with stars escaping and spreading.

For a coherent velocity dispersion, each star inherits most of its velocity from its family tree. For each matured child, of each generation, the code calculates the number of decedents (i.e. stars) and calculates the total mass of this child. This sets the velocity dispersion for this sub-group to be in virial equilibrium. Now each next generation child inherits the velocity of its parent and process of finding the correct velocity dispersion of this new smaller sub-sets is repeated. Hence the stars i.e. the final generation inherit all velocities from their previous generations, leading to a coherent velocity dispersion.

2.2 The Astrophysical Multipurpose Software Environment (AMUSE)

The Astrophysical Multipurpose Software Environment (AMUSE) is a programming framework, designed to manage multi-scale, multi-physics simulations in a hierarchical, extensible, and internally consistent way. Constructed as a collection of individual modules, AMUSE allows computational tools for different physical domains and scales (see Figure 2.2) (Pelupessy et al., 2013) to be easily combined into a single task. It facilitates the coupling of modules written in different languages by providing inter-language tools and a standard programming interface that represents a balance between generality and computational efficiency (McMillan et al., 2012).
The basic functionalities of AMUSE are:

1. A homogeneous, physically motivated interface for existing astronomical simulation codes.
2. Incorporation of multiple community codes from four fundamental domains (stellar evolution, gravitational dynamics, hydrodynamics and radiative transfer).
3. The ability to design new simulation experiments by combining one or more of the community codes in various ways.

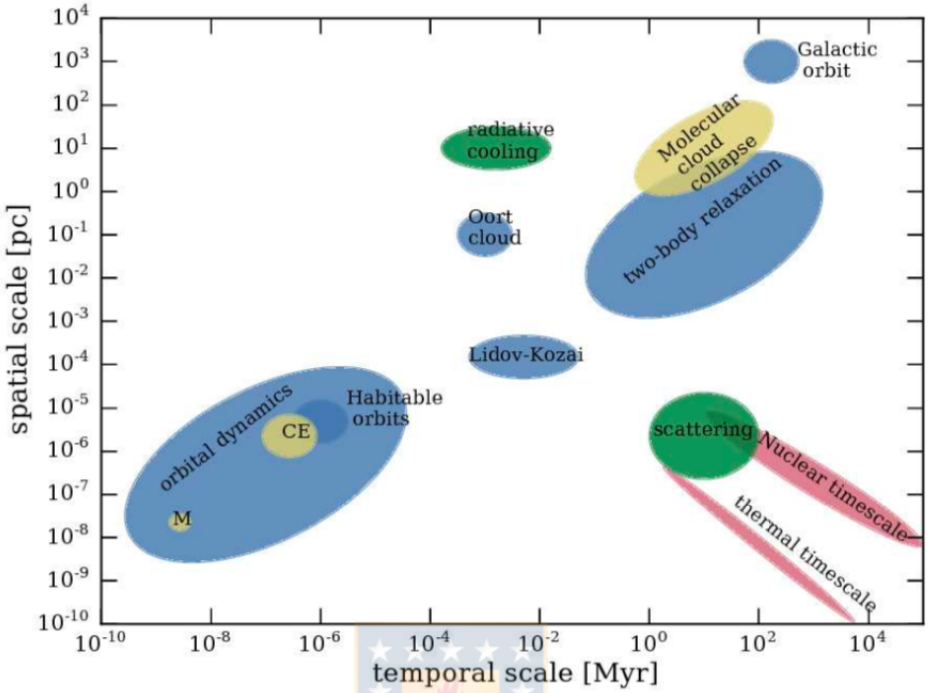

FIGURE 2.2. Physical domains of AMUSE. Typical temporal and spatial scales for a number of astronomical phenomena. The ellipses indicate specific areas of interest and the color indicate physical domains: gravity (blue), stellar evolution (red), hydrodynamics (yellow), and radiative process (green), are indicated at several locations in the plane of temporal and spatial scales. Several domains are identified by name, such as the collapse of a giant molecular cloud (top right in yellow), the range of the habitable planet orbits (blue circle at lower left) and several small scales as mergers indicated by M and common envelope evolution indicated by CE are embedded within the orbital dynamics scale ellipse. Figure from Portegies Zwart and McMillan (2018).

The target domains for the initial release of AMUSE were gravitational dynamics, stellar evolution, hydrodynamics and radiative transfer (see Figure 2.3), but AMUSE can be extended by including other codes and domains, which can then be contributed to the AMUSE repository. In addition to providing an unified interface to various types of codes, AMUSE has the objective of facilitating multiphysics simulations. The basic structure of the AMUSE framework is illustrated in Fig.2.4. The figure is subdivided intro three general parts. The top layer (red and orange) is mostly user written, the middle layer (blue) implements the interfaces onto the community codes, an the bottom layer (green) is the community modules and the actual community source code, which is connected to the rest of the framework via the MPI or sockets.

The components can be described as follow:

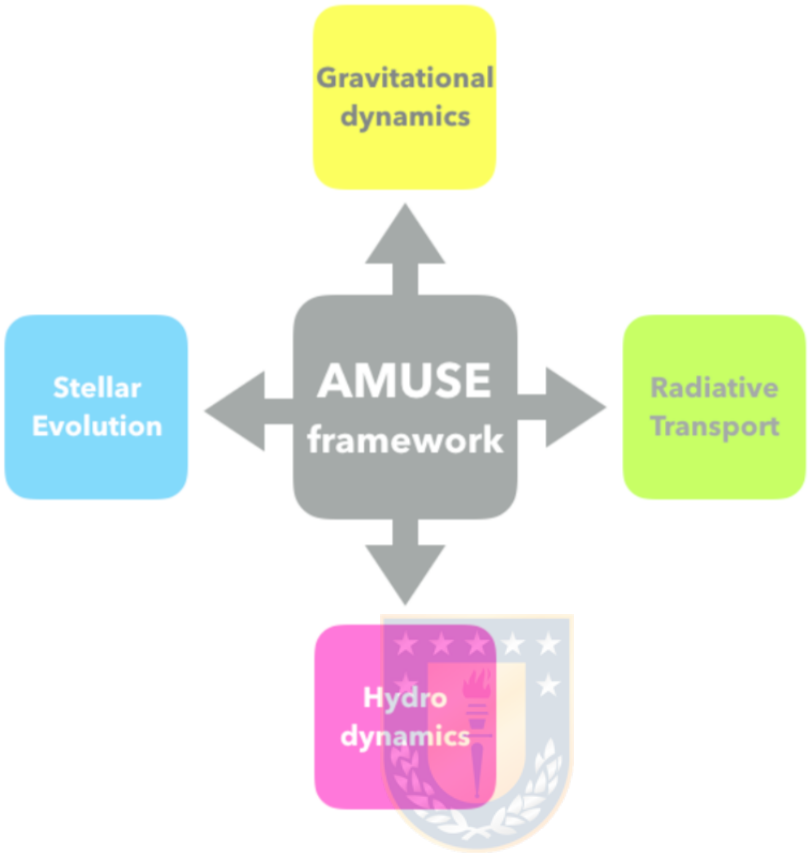

FIGURE 2.3. Fundamental domains of AMUSE. The philosophy of AMUSE, with the central AMUSE framework surrounded by its four fundamentals physical solver, i.e., stellar evolution, gravitational dynamics, radiative transport and hydro dynamics.

1. The Python user script (marked red in Figure 2.4), which addresses a specific physical problem or set of problems, in the form of system-provided or user-written Python commands that serve as the user interface onto the framework. This is the only part of a production script that needs to be written by the user. The coupling between community codes is implemented in this layer, with the help of support classes for converting units and data structures provided by AMUSE.

2. The community module, comprising three key elements:

   - The manager (orange), which provides an object-oriented interface onto the communication layer via a suite of system-provided utility functions. This layer handles unit conversion, and also contains the state engine and the associated data repository, all of which are required to guarantee consistency of data across modules. This layer is generic, it is not specific to any particular problem or physical domain.

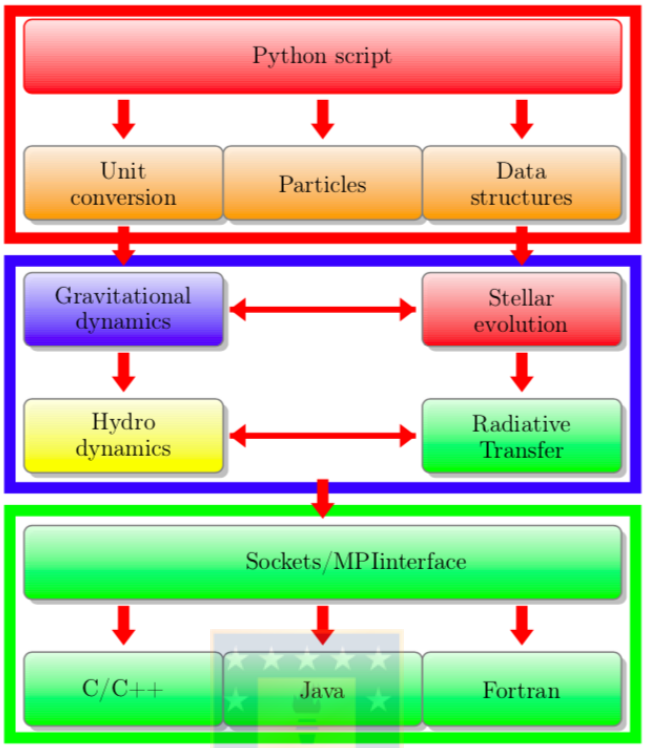

FIGURE 2.4. General structure of AMUSE framework. The user writes the Python script (top red layer). The lower orange layers are responsible for units and data structure. The framework outlined in blue represents the interfaces to the community modules (see Figure 2.3), which connect via sockets or MPI (cyan) to the community codes at bottom. Information flows downward to the community modules, as indicated by the red arrows, as well as upward, back to the Python script. Figure from Portegies Zwart and McMillan (2018).

- The community layer (blue), which realizes the bidirectional communication between the manager and the community code layer. This is implemented via a proxy and an associated partner, which together provide the connection to each community code.
- The community code layer (green), which contains the actual community codes and implements control and data management operations on them. Each piece of code in this layer is domain specific, although the code may be designed to be very general within its particular physical domain.

The main characteristics of AMUSE are:

- AMUSE offers a suite of codes that cover different physical domains (see Fig.2.3). Each domain is represented by at least two different codes, the minimum needed for verification of the simulations (Portegies Zwart et al., 2013).

- Standard interfaces for the different gravitational dynamics integrators make swipping one integrator for the other trivial.
- Codes for different domains can be combined by the use of the BRIDGE.
- AMUSE itself is implemented in Phyton, which provides the user with the flexibility needed to quickly generate astrophysical experiments thanks to its ease of programming, while the physics solvers are written in different programming languages.
- AMUSE provides unit-aware interfaces, so any data that must be transferred between codes is automatically transformed to the required units, without any additional user input.

2.2.1 Gravitational dynamics

The gravity codes included in AMUSE span most dynamic regimes except that support for large scale cosmological simulations is limited. Hermite0, PhiGRAPE, ph4 and HiGPUs are direct $N-$body integrators with Hermite time stepping schemes, where the latter three are tooled to use hardware (GRAPE or GPU) accelerated force calculation.
The interface to the different gravitational dynamics codes is the same. However, the gravitational dynamics integrators that are included in AMUSE are geared towards different types of problems.

2.2.1.1 Ph4 code

PH4 is a 4th order Hermite predictor-corrector $N-$body code, written in C++ and compatible with GPU acceleration. An $N-$body code is a piece of software that calculates the acceleration that a particle is subjected to, and updates its position and velocity. The acceleration ($\mathbf{a}_i$) corresponds to the sum of the gravitational acceleration from all the other $N-1$ bodies in the system. Once the net acceleration of the particle is determined, different codes use different ways to update the position and velocity of the particle (McMillan et al., 2012; Portegies Zwart et al., 2013).
A 4th order Hermite integrator uses not only the acceleration, but also the higher derivatives, to construct interpolation polynomials of the force (Makino and Aarseth, 1992). For particle i, using the position $\mathbf{r}_i$ and velocities $\mathbf{v}_i$ at time $t = t_0$, we calculate the acceleration $\mathbf{a}_i$ and its derivative $\dot{\mathbf{a}}_i$. The acceleration corresponds to the gravitational pull from all the other particles:

$$\mathbf{a}_{0,i} = G \sum_{i \neq j} \frac{m_j}{\mathbf{r}_{ij}^3} \mathbf{r}_{ij}, \tag{2.1}$$

where G is the gravitational constant, m_j the mass of the $j-$th particle, and $\mathbf{r}_{ij} = \mathbf{r}_j - \mathbf{r}_i$, while the derivative of the acceleration, $\dot{\mathbf{a}}_i$, is:

$$\dot{\mathbf{a}}_{0,i} = G \sum_{i \neq j} m_j \left(\frac{\mathbf{v}_{ij}}{\mathbf{r}_{ij}^3} - \frac{3(\mathbf{r}_{ij} \cdot \mathbf{v}_{ij})\mathbf{r}_{ij}}{\mathbf{r}_{ij}^5} \right), \tag{2.2}$$

where, $\mathbf{v}_{ij} = \mathbf{v}_j - \mathbf{v}_i$.
Now, we calculate a prediction for the values of $\mathbf{r}_i$ and $\mathbf{v}_i$. These predicted values are obtained from the Taylor expansion of $\mathbf{r}_i$ and $\mathbf{v}_i$:

$$\mathbf{r}_{i,p} = \mathbf{r}_i + \Delta t \mathbf{v}_i + \frac{\Delta t^2}{2}\mathbf{a}_{0,i} + \frac{\Delta t^3}{6}\dot{\mathbf{a}}_{0,i},$$
$$\mathbf{v}_{i,p} = \mathbf{v}_i + \Delta t \mathbf{a}_i + \frac{\Delta t^2}{2}\dot{\mathbf{a}}_{0,i}.$$

From the predicted values $\mathbf{r}_{i,p}$ and $\mathbf{v}_{i,p}$, the acceleration and its derivative at $t = t_0 + \Delta t$, $\mathbf{a}_{1,i}$ and $\dot{\mathbf{a}}_{1,i}$, are obtained using Equations 2.1 and 2.2.
The predictes values $\mathbf{r}_{i,p}$ and $\mathbf{v}_{i,p}$ must be corrected, the corrector is calculated using the higher derivatives of $\dot{\mathbf{a}}_i$, i.e, $\mathbf{a}_i^{(2)}$ and $\mathbf{a}_i^{(3)}$:

$$\Delta r_i = \frac{\Delta t^4}{24}\mathbf{a}_i^{(2)} + \frac{\Delta t^5}{120}\mathbf{a}_i^{(3)},$$
$$\Delta v_i = \frac{\Delta t^3}{6}\mathbf{a}_i^{(2)} + \frac{\Delta t^4}{24}\mathbf{a}_i^{(3)}.$$

$\mathbf{a}_0^{(2)}$ and $\mathbf{a}_0^{(3)}$ are not calculated directly from the positions and velocities. Instead, we use the original values of $\mathbf{a}_0$ and $\dot{\mathbf{a}}_0$, plus the values obtained from the corrected position and velocity, $\mathbf{a}_i$ and $\dot{\mathbf{a}}_i$, by using the following expressions:

$$\mathbf{a}_i^{(2)} = \frac{-6(\mathbf{a}_0 - \mathbf{a}_1) - \Delta t(4\dot{\mathbf{a}}_0 + 2\dot{\mathbf{a}}_1)}{\Delta t^2},$$
$$\dot{\mathbf{a}}_i^{(3)} = \frac{12(\mathbf{a}_0 - \mathbf{a}_1) + 6\Delta t(\dot{\mathbf{a}}_0 + \dot{\mathbf{a}}_1)}{\Delta t^3}.$$

Finally, the corrected position, $\mathbf{r}_{c,i}$, and corrected velocity, $\mathbf{v}_{c,i}$, are determined:

$$\mathbf{r}_{c,i} = \mathbf{r}_{p,i} + \Delta r,$$
$$\mathbf{v}_{c,i} = \mathbf{v}_{p,i} + \Delta v.$$

This process is repeated for each particle and for each time step.

2.2.1.2 BRIDGE algorithm

The BRIDGE method provides a way to couple different codes to obtain a self-consistent simulation (Fujii et al., 2007). In this new method Fujii et al. (2007) consider a star cluster (subscript SC) orbiting a parent galaxy (subscript G). The star clusters are integrated using a fourth-order Hermite scheme (Makino and Aarseth, 1992), with individual time steps and direct summation of the interstellar gravitational forces, while galaxies are integrated using the tree code and leapfrog scheme with a shared time step. Fujii et al. (2007) combine them by embedding a direct scheme into the tree code. Using this new algorithm, they have made it possible to perform fully self-consistent N-body simulations of star clusters that orbit in their parent galaxies with

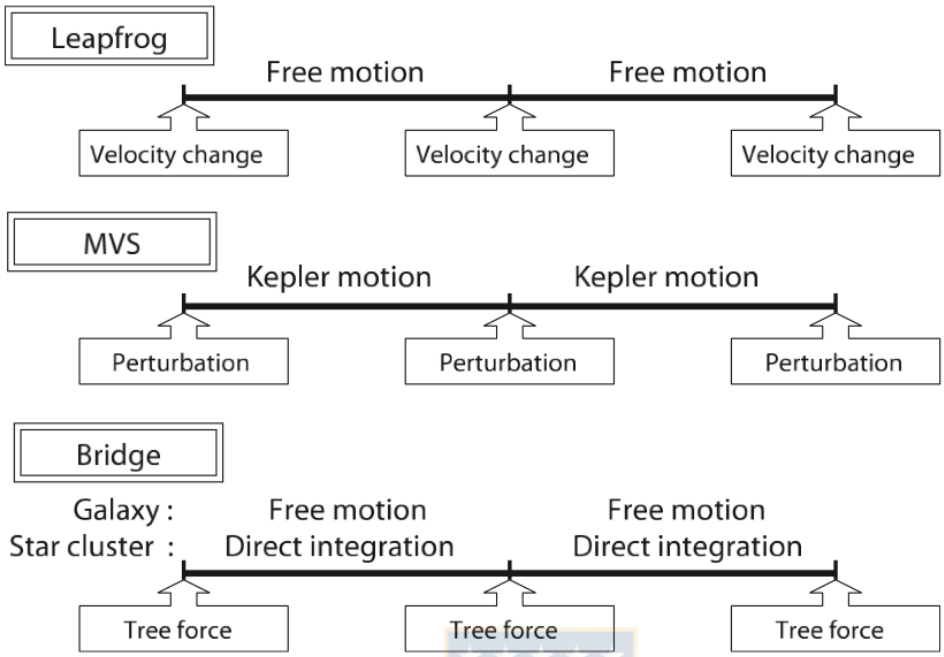

FIGURE 2.5. Procedure of the BRIDGE scheme. This scheme translates to the following algorithm: (1) The BRIDGE scheme make a tree at t_0 and calculate the acceleration from all particles on galaxy particles, $\mathbf{a}_{\{\mathrm{All}\to\mathrm{G},0\}}$, and from galaxy particles on star cluster particles, $\mathbf{a}_{\{\mathrm{G}\to\mathrm{SC},0\}}$,using the tree. (2) Star cluster give a velocity kick and the galaxy update the velocity. (3) The star cluster integrate the positions and the velocities from t to $t+\Delta t$ using the Hermite scheme with individual time steps and the galaxy update the position with the leapfrog scheme. (4) Make a new tree at $t+\Delta t$ and calculate the accelerations from all particles on galaxy particles,$\mathbf{a}_{\{\mathrm{All}\to\mathrm{G},1\}}$, and from galaxy particles on star cluster particles, $\mathbf{a}_{\{\mathrm{All}\to\mathrm{SC},1\}}$. (5) The star cluster give a velocity kick and the galaxy update the velocity. Figure from Fujii et al. (2007)

very accurate time integration for star clusters and fast time integration for the parent galaxy (Portegies Zwart and McMillan, 2018). The procedure of the BRIDGE scheme applied to the galaxy-cluster system is summarized in Figure 2.5 and as follows (advancing from time 0 to time 1) (Portegies Zwart and McMillan, 2018; Fujii et al., 2007):

- Make a tree at t_0 and calculate the acceleration from all particles on galaxy particles, $\mathbf{a}_{\{\mathrm{All}\to\mathrm{G},0\}}$, and from galaxy particles on star cluster particles, $\mathbf{a}_{\{\mathrm{G}\to\mathrm{SC},0\}}$, using the tree.

- Kick cluster star velocities with time step $\frac{1}{2}\Delta t$ using accelerations due to the galaxy; kick galaxy particle velocities with time step $\frac{1}{2}\Delta t$ using accelerations due to both galaxy and

cluster:

$$\mathbf{v}'_{\mathrm{SC},0} = \mathbf{v}_{\mathrm{SC},0} + \frac{1}{2}\Delta t\, \mathbf{a}_{\{\mathrm{G}\to\mathrm{SC},0\}},$$
$$\mathbf{v}'_{\mathrm{G},0} = \mathbf{v}_{\mathrm{G},0} + \frac{1}{2}\Delta t\, \mathbf{a}_{\{\mathrm{All}\to\mathrm{G},0\}},$$

where subscripts SC and G stand for the star cluster and the galaxy, respectively; subscript 0 indicate time t and $\mathbf{a}_{\{\mathrm{All}\to\mathrm{G}\}}$ denotes the acceleration due to the gravitational forces from all particles (including star cluster particles) to the galaxy particle.

- Update (drift) cluster positions and kicked velocities with with time step Δt, using the internal cluster integration scheme and kicked velocities; update galaxy particles positions with time step Δt using kicked velocities:

$$\mathbf{x}_{\mathrm{SC},0} \to \text{(Hermite scheme)} \to \mathbf{x}_{\mathrm{SC},1},$$
$$\mathbf{v}'_{\mathrm{SC},0} \to \text{(Hermite scheme)} \to \mathbf{v}'_{\mathrm{SC},1},$$
$$\mathbf{x}_{\mathrm{G},1} = \mathbf{x}_{\mathrm{G},0} + \Delta t\, \mathbf{v}'_{\mathrm{G},0},$$

where subscript 1 indicate time $t + \Delta t$ and $\mathbf{v}'_{\mathrm{SC},1}$ represent a new velocity at $t + \Delta t$, which has been integrated using the Hermite scheme.

- Recompute accelerations and complete the step by updating (kicking) all cluster and galaxy velocities:

$$\mathbf{v}_{\mathrm{SC},1} = \mathbf{v}'_{\mathrm{SC},1} + \frac{1}{2}\Delta t\, \mathbf{a}_{\{\mathrm{G}\to\mathrm{SC},1\}},$$
$$\mathbf{v}_{\mathrm{G},1} = \mathbf{v}'_{\mathrm{G},\frac{1}{2}} + \frac{1}{2}\Delta t\, \mathbf{a}_{\{\mathrm{All}\to\mathrm{G},1\}},$$

where subscript $\frac{1}{2}$ indicate time $t + \frac{1}{2}\Delta t$.

The main idea of AMUSE, is that different codes specialize in different physics, but these, different codes, can be brought together with BRIDGE, i.e, the evolution of the system under one code can influence the evolution under a second code, and vice versa. This is done by, first, the velocities of the particles of the system are modified due to the gravitational influence of the other system. then each system evolves in isolation and finally, the velocities are, again, modified by the interaction with the other system.

CHAPTER 3

METHOD AND INITIAL CONDITIONS

In this work we focus on the smallest half-light radius of any known Local Group dwarf galaxy, with may be, the possible exception of Willman 1, mean that Segue 1 also has the densest known concentration of dark matter, with average density enclosed within its half-light radius is $2.5^{+4.1}_{-1.9}$ $M_{\odot}pc^{-3}$, substantially higher than that found in other dwarf galaxies of the solar neighborhood.

We model Segue 1 by perfoming numerical simulations using the Astrophysical Multipurpose Software Environment (AMUSE) to study a star formation scenario for ultra-faint dwarf dSph galaxies. We aim we proposed an alternative formation channel, in continuation to our Dissolving Star Cluster model for classical dSph galaxies. We study a formation scenario with a strong background potential mimicking the dark matter halo. Our stars are initially in virial equilibrium and placed in a filamentary stellar distribution, a fractal distribution, within an analytical halo, building the faint luminous component that we observe. To move the stars under their own gravity we used the Ph4 code.

3.1 Segue 1

Segue 1 was discovered by Belokurov et al. (2007) as an overdensity of resolved stars in imaging data from the Sloan Digital Sky Survey, at a distance of 23 ± 2 kpc from the Sun, is the closest dwarf galaxy other than Sagittarius and estimated the distance to the Sagittarius Stream to be ~ 20 kpc (Norris et al., 2010).

It was first classified as a globular cluster, primary because it was more compact and fainter ($M_{\rm v} = -1.5$) those the galaxies known at this time and because of its small half-light radius (30 pc), but Geha et al. (2009) presented a strong case based on internal stellar kinematics that Segue 1 is highly dark matter dominated and therefore a galaxy (Frebel et al., 2014) and Simon

TABLE 3.1. Summary of Properties of Segue 1. Table from Simon et al. (2011)

Quantity	Value
R.A. (J2000) (h m s)	$10:07:03.2 \pm 1.7$
DEC (J2000) (° ′ ″)	$+16:04:25 \pm 15$"
Distance (kpc)	23 ± 2
$M_{\rm v}$	$-1.5^{+0.6}_{-0.8}$
$L_{\rm v}$ ($L_\odot$)	340
ϵ	$0.48^{+1.0}_{-0.13}$
$\mu_{\rm v,0}$ (mag arcsec^{-2})	$27.6^{+1.0}_{-0.7}$
$r_{\rm eff}$ (pc)	29^{+8}_{-5}
$v_{\rm hel}$ kms^{-1}	208.5 ± 0.9
$v_{\rm GSR}$ kms^{-1}	113.5 ± 0.9
σ kms^{-1}	$3.7^{+1.4}_{-1.1}$
Mass $M_\odot$	$5.8^{+8.2}_{-3.1} \times 10^5$
$M/L_{\rm v}$ ($M_\odot/L_\odot$)	3400
Mean [Fe/H]	-2.5

et al. (2011) based on the results of their observations clearly point confirm that Segue 1 is a dark matter dominated galaxy in fact, it has the highest mass-to-light ratio, and is therefore the darkest galaxy, yet found.

The study of Segue 1 can we help to understand the star formation in low density and low metallicity environments, is extremely useful for our understanding of structure formation in the universe and represent an useful probe of the galaxy formation on smallest scales.

3.2 Initial conditions of the stars

To generate the initial distribution of stars we used the method proposed by Goodwin and Whitworth (2004) to produce a initial fractal distribution of stars from a turbulent gas cloud (see section 2.1). We defined a non-uniform distribution of stars, i.e., a fractal dimension of $D = 1.6$, a cube of size $N_{\rm div} = 2$ in which case there are 8 sub-cubes and 8 first-generation children and we assign six different fractal radius, $r_{\rm frac} = 30$, 50, 70, 100, 150 and 200 pc, in order to investigate the evolution of substructures. The filamentary stellar formation region is formed by 700 particles with equal mass of 0.5 $M_\odot$ in virial equilibrium, so, the distribution have enough kinetic energy to support themselves against overall collapse.

Figure 3.1 shows in detail an example of the evolution of 700 stars in a fractal radius of $r_{\rm frac}$ = 200 pc and a Plummer distribution with a scale-length, $R_{\rm Pl} = 0.5$ kpc, from t = 0 to the final stage of evolution, t = 5 Gyr. We observe the initially very clumpy distribution rapidly collapses. At first some of the clumps disperse, but the larger of these clumps then attract nearby clumps. The

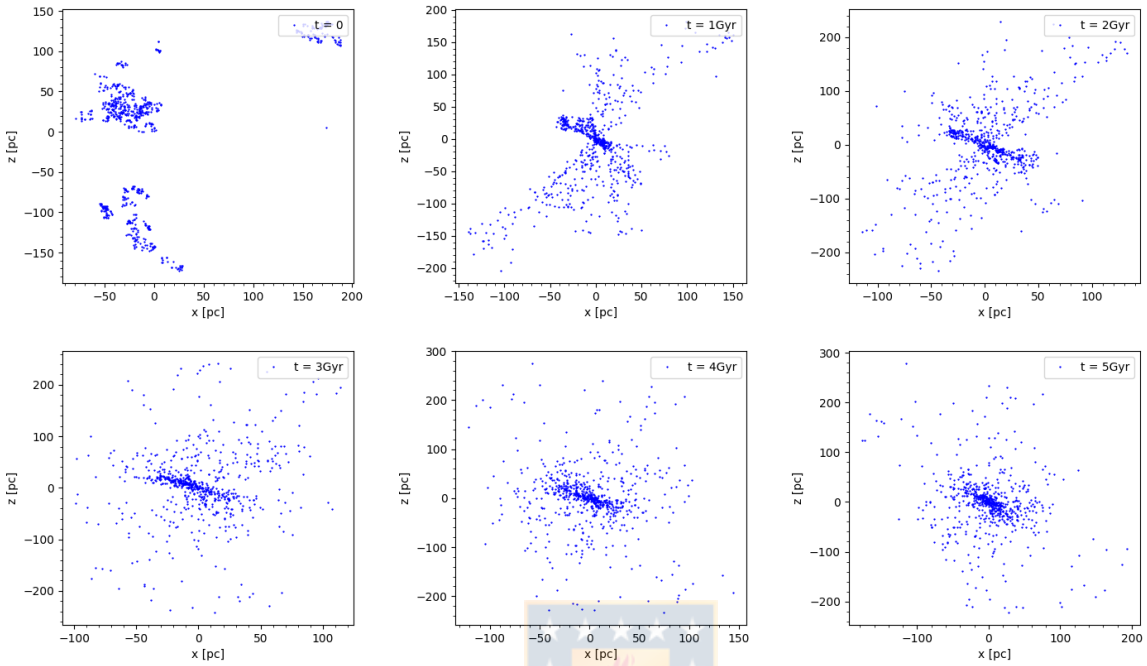

FIGURE 3.1. Example of the evolution of the distribution of stars from t = 0 to t = 5 Gyr. The blue points represent the stars ($M_\star = 0.5\ M_\odot$) in virial equilibrium, with a fractal distribution of D = 1.6 in a radius of $r_{fractal} = 200$ pc and $R_{Pl} = 0.5$ kpc. We observe the initially very clumpy distribution rapidly collapses. At first some of the clumps disperse, but the larger of these clumps then attract nearby clumps. The initial clumpiness is erased as most clumps merge.

TABLE 3.2. Summary of initial condition of stars with the fractal generator

Parameter		
Number of stars	$N_\star$	700
Stellar mass	$m_\star$	$0.5\,M_\odot$
Physical size of the system	r_{scale}	[30, 200]
Total mass of the distribution	m_{scale}	$350\,M_\odot$
Fractal dimension	D	1.6
Size cube	N_{div}	2.0
Virial ratio	α	0.5

initial clumpiness is erased as most clumps merge.

Table 3.2 and 3.3 shows a summary of the initial parameters of the fractal distribution and the Plummer models used in the simulations.

TABLE 3.3. Parameter of the Plummer models used in the simulations.

Model	M(r) $M_\odot$	R_{Pl} kpc	M_{Pl} $M_\odot$
Model 1	6×10^5	1.0	2.2×10^{10}
Model 2	6×10^5	0.5	2.8×10^{9}
Model 3	6×10^5	0.25	3.5×10^{8}

3.3 Plummer potential

We express the background potential as an analytical halo with a Plummer sphere (Plummer, 1911), with a dense center and reducing the value with the radius. The Plummer density profile follow the equation:

$$\rho(r) = \frac{3\,M_{Pl}}{4\,\pi\,R_{Pl}^3}\left(1+\frac{r^2}{R_{Pl}^2}\right)^{-\frac{5}{2}},$$

where we can identify the Plummer mass, M_{Pl}, as the total mass of the system, and the Plummer radius, R_{Pl}, as a scale length. The potential generated by this mass distribution is given by the equation:

$$\Phi(r) = -\frac{GM_{Pl}}{\sqrt{r^2+R_{Pl}^2}},$$

where G is Newton's gravitational constant.
The mass enclosed within radius r is given by,

$$M(<r) = M_{Pl}\,\frac{r^3}{\left(r^2+R_{Pl}^2\right)^{3/2}}.$$

For our simulations we use a mass enclosed of $6\times10^5\,M_\odot$ within a radius $r = 30$ pc and we assign three different Plummer radius, R_{Pl} = 1, 0.5 and 0.25 kpc, and we assume a physical size r_{frac} of the system between 30 to 200 pc, i.e. R_{Pl} and r_{frac} are the parameters that we systematically vary in the simulations to investigate the influence of the initial size of the Dark Matter halo and the initial size of the stellar distribution on the final object and known if our models are able to reproduce all kinematical and structural properties of UFDs like Segue 1 (e.g. patchy structure, ellipticity, effective radius and velocity dispersion).
The simulations evolve for 5 Gyr. The AMUSE script used to run the simulations is shown in Appendix A.

CHAPTER 4

RESULTS

In this chapter we present the results obtained from the simulations we performed and the analysis of them. We use 700 stars of 0.5 $M_\odot$ randomly placed (following a fractal distribution) within an analytical halo (following a Plummer distribution), and follow their evolution for 5 Gyr (see Chapter 3). The simulations have been repeated using a different random number seeds to explore the variations of the properties of the object formed from 10 different realizations of the same initial conditions.
The mean values show for each parameter of the final object for each Plummer distribution are obtained averaging the mean values of each fractal radius, and the error is the standard deviation of these six values.

4.1 Size of the final object

4.1.1 Lagrangian radii

A Lagrangian radius is the radius of an imaginary sphere about the centre of the stellar system containing a fixed portion of its total mass (Sweatman, 1993). To study and analyse the spatial evolution of our objects we monitor the Lagrangian radii at 50% for 5 Gyr of evolution as a function of the fractal radius of the initial distribution of stars.
Figure 4.1 shows the time-evolution of the 50% Lagrangian radii i.e. the half-mass radii through 5 Gyr of evolution for each initial fractal radius. Purple inverted unfilled triangles, green crosses, blue unfilled squares, red unfilled open circles, orange crosses and dark green asterisk fractal radii, with R_{frac} = 30, 50, 70, 100, 150 and 200 pc, respectively. The top panel shows the relation between the 50% Lagrangian radii and the fractal radius using a R_{Pl} = 1 kpc, the middle panel

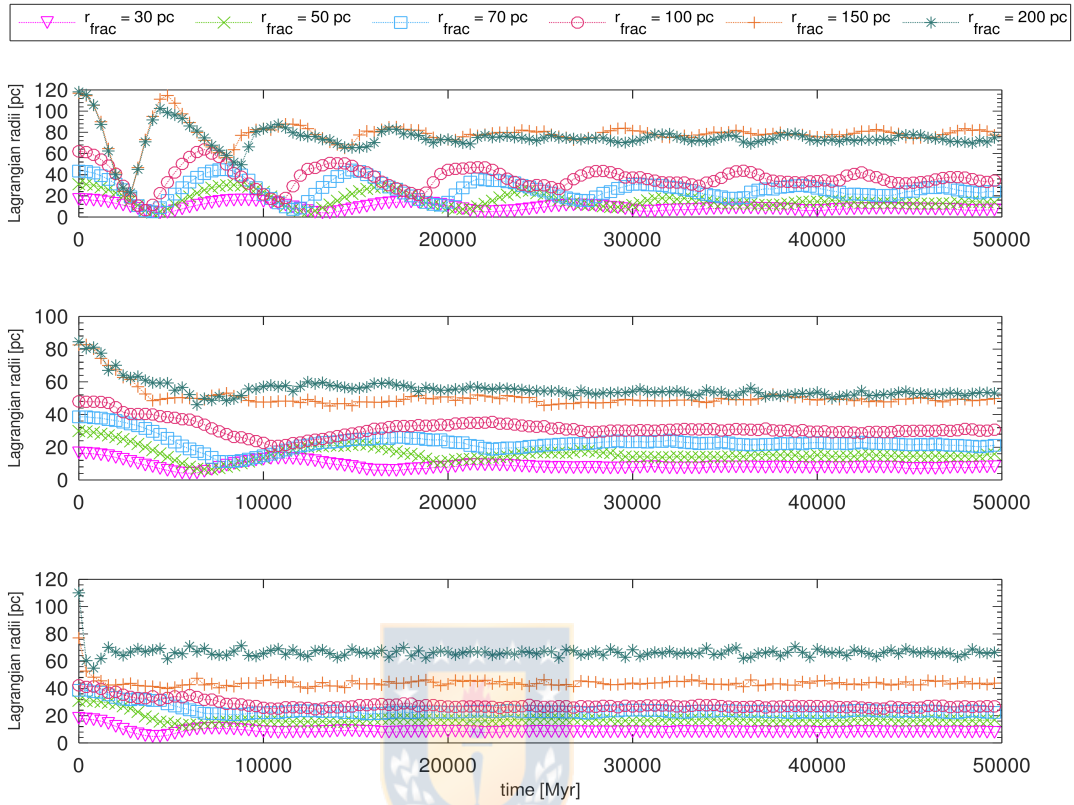

FIGURE 4.1. Time-evolution of the 50% Lagrangian radii throughout 5 Gyr of evolution. Top panel shows the relation between the Lagrangian radii at 50% of the total mass with the fractal radius when we use a R_{Pl} = 1 kpc, middle panel represent the model with a R_{Pl} = 0.5 kpc and the bottom panel shows the time-evolution of the Lagrangian radii for a R_{Pl} = 0.25 kpc. Purple inverted unfilled triangle, green crosses, blue unfilled square, red unfilled open circle, orange cross and dark green asterisk represent fractal radii, of R_{frac} = 30, 50, 70, 100, 150 and 200 pc, respectively.

represents the model with a R_{Pl} = 0.5 kpc and the bottom panel shows the time-evolution of the Lagrangian radii for R_{Pl} = 0.25 kpc. We observe in almost all simulations with smaller scale-lengths of the DM halo that the final object evolves into a stable object whitin the first Gyr of evolution. It is interesting to note that we see a different behavior when R_{Pl} = 1 kpc, where the object needs at least 3 Gyr to stabilize. When we analyze the evolution of the Lagrangian radii for each fractal radius, all show similar evolution independent of initially scale-length selected. The obvious result we see is that larger initial fractal radii lead to larger final objects.

As a result we see that while we increase the initial Plummer radius the object needs more time to stabilize independent of the fractal distribution initially selected. Also it is possible noticed that 5 Gyr is enough time for the object to evolve into a quasi-stable configuration.

TABLE 4.1. Values of the linear fitting function by a least square fitting for the 50% Lagrangian radii. The first column shows the Plummer radius and m is the slope of the fitting line, c the free parameter and ϵ the associated error.

R_{Pl} [kpc]	m	c	ϵ
1.0	0.43	−2.5	±0.99
0.5	0.43	−3.6	±0.98
0.25	0.44	−3.8	±0.99

Figure 4.2 shows the half-mass radius against the initial size of the fractal for each Plummer distribution. The data points are mean values calculated from 10 realizations. Cyan circles represent $R_{Pl} = 1$ kpc, purple squares represent a $R_{Pl} = 0.5$ kpc and the orange diamonds represent $R_{Pl} = 0.25$ kpc. The green dashed line shows the effective radius of Segue 1 and the dotted lines represent a least square fitting to the data. We use a linear fitting function by a least square fitting and the results obtains for the fitting lines are shown in Table 4.1, where m is the slope of the fitting line, c the free parameter and ϵ the associated error. Here we can see all 3 fits are the same. The size of the final object does not depend on the chosen R_{Pl} but only on the size of the initial fractal, i.e. the size of e.g. Segue 1 does not reflect the halo scale-length.

We observe that Lagrangian radii show an increasing trend with the scale-length of the fractal distribution, i.e. the larger the fractal radius, the larger the half-mass radius of the final object. However, our results show that the variation in the fractal radius of the initial distributions of stars can produce, in some cases, results far away from the observational data that we have today, but it is very clearly visible is that using cored haloes we need fractal distributions between 70 – 100 pc to reproduce Segue 1.

4.2 Central Surface Brightness

A surface brightness profile shows the integrated light along a line-of-sight. As we do not know along which line-of-sight our objects may be observed, we calculate a mean value out of three possible sight-lines along the Cartesian coordinate axes x, y and z. To fit our data points, we use an exponential shaped profile for the surface density distribution, i.e. a Sersic profile with a fixed index $n \approx 1$:

$$I(R) = I_e \exp\left(-b_n\left[\left(\frac{R}{R_{eff}}\right)^{\frac{1}{n}} - 1\right]\right),$$

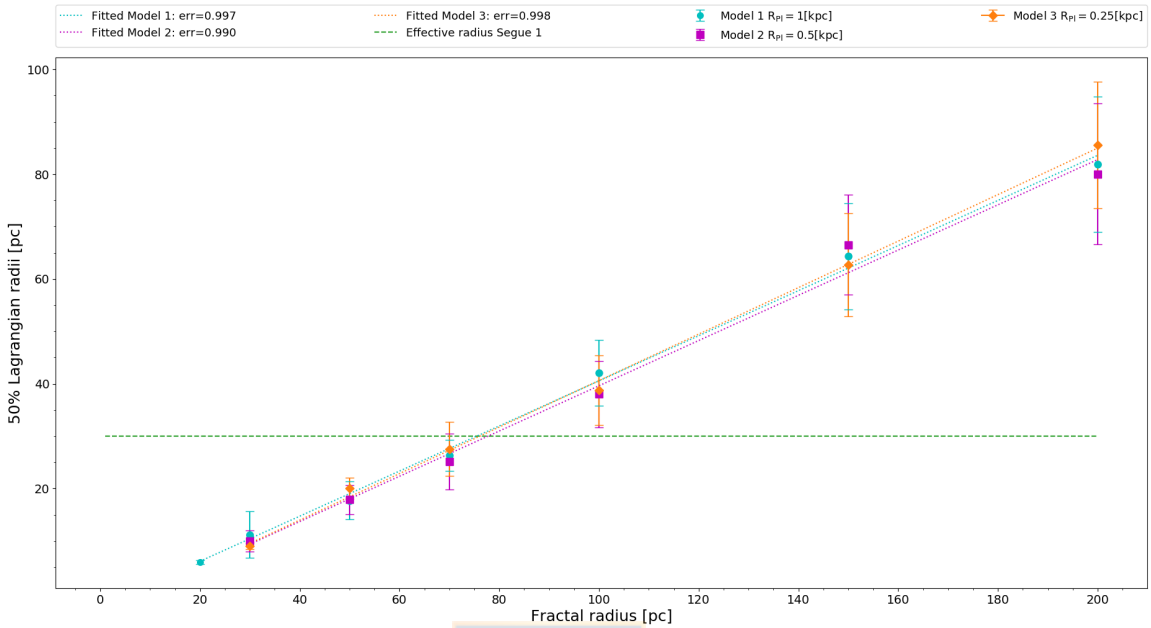

FIGURE 4.2. Half-mass radius against the initial size of the fractal for each Plummer distribution. Cyan circles represent $R_{Pl} = 1$ kpc. Purple squares represent $R_{Pl} = 0.5$ kpc and orange diamonds represent the Lagrangian radii for a $R_{Pl} = 0.25$ kpc. The green dashed line shows the effective radius of Segue 1. As the scale-length of a dSph usually should be smaller than the half-mass radius, we see that for our choices of DM haloes we need a fractal distribution of $70 - 100$ to obtain similar results to Segue 1.

where R_{eff} is the scale-length, I_e is the surface density at the effective radius and $b_n = 1.999n - 0.327$ (Caon et al., 1990).

Simon et al. (2011) estimated the average density enclosed within its half-light radius of Segue 1 is $2.5^{+4.1}_{-1.4}\,M_\odot pc^{-3}$, subtantially higher than that found in other dwarf galaxies (e.g. Simon and Geha (2007)).

The mean values of the two free parameters of the final object by fitting an exponential profile are shown in Table 4.2. The first column shows the Plummer radius, where Model 1, Model 2 and Model 3 represents a $R_{Pl} = 1.0$, 0.5, and 0.25 kpc, respectively. The second column shows the initial size of the fractal distribution and the last two columns show the surface density at the effective radius, I_e and the scale-length, R_{eff}.

Table 4.2 show the correlation of the two free parameters (I_e, R_{eff}) of the exponential profile with initial size of the DM halo and the initial size of the stellar distribution. Shows clearly that we

TABLE 4.2. Mean values of the final object. The first column shows the Plummer radius, where Model 1, Model 2 and Model 3 represent a R_{Pl} = 1.0, 0.5, and 0.25 kpc, respectively. The second column shows the initial size of the fractal distribution and the last two columns shows the two free parameters, the surface density at the effective radius, I_e and the scale-length radius, R_{eff}, by fitting an exponential profile.

Model	Fractal Radius pc	I_e $M_\odot pc^{-2}$	R_{eff} pc
Model 1	30	7.84 ± 2.8	2.82 ± 0.4
	50	4.26 ± 2.5	4.29 ± 1.3
	70	1.73 ± 0.9	5.85 ± 1.6
	100	1.09 ± 0.4	6.48 ± 1.7
	150	0.74 ± 0.5	7.95 ± 2.4
	200	0.36 ± 0.2	10.42 ± 4.9
Model 2	30	4.61 ± 3.4	3.76 ± 1.1
	50	3.08 ± 0.9	4.04 ± 0.9
	70	2.02 ± 0.6	4.94 ± 0.9
	100	1.33 ± 0.6	6.12 ± 1.7
	150	0.63 ± 0.4	9.49 ± 4.2
	200	0.42 ± 0.2	10.15 ± 2.6
Model 3	30	6.03 ± 1.3	2.77 ± 0.3
	50	2.29 ± 0.7	4.38 ± 0.5
	70	1.78 ± 0.6	4.56 ± 1.1
	100	1.45 ± 0.9	7.17 ± 3.8
	150	0.77 ± 0.3	8.49 ± 2.3
	200	0.54 ± 0.3	9.04 ± 4.3

have no important changes in the surface brightness profile parameters when we change the scale-length of the halo, but we observe a dependency as a function of the initial size of the fractal distribution. Instead from Figure 4.3 we do see a dependency: surface density decreases if we use to larger stellar distribution sizes, so if we distribute the stellar mass more concentrated, the scale-length radius of the final object is notoriously decreasing. This is also expected because if the luminous matter started more concentrated, it should also be more concentrated in the final object.

In Figure 4.3 we use a linear fitting function by a least square fitting and the results obtains for the fitting lines are shown in Table 4.3, where m is the slope of the fitting line, c the free parameter and ϵ the associated error. Here we can see all 3 fits are almost the same.

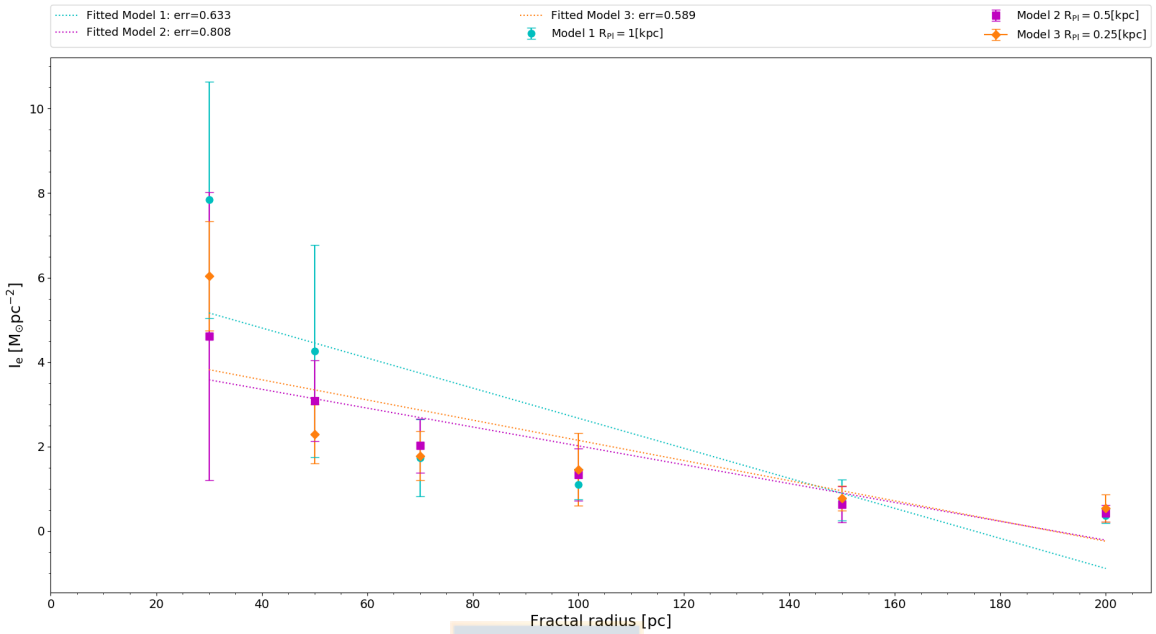

FIGURE 4.3. Surface density, I_e, as a function the initial size of the fractal for each Plummer distribution. Cyan circles represent the I_e as a function of their R_{Pl} = 1 kpc. Purple square represent the relation between the I_e with a R_{Pl} = 0.5 kpc and the orange diamonds represent the I_e for a R_{Pl} = 0.25 kpc. The data points are mean values calculated from 10 realizations of these parameters and the dotted lines represent the data with a linear fitting function by a least square fitting.

TABLE 4.3. Values of the linear fitting function by a least square fitting for the surface density at the effective radius, I_e. The first column shows the Plummer radius and m is the slope of the fitting line, c the free parameter and ϵ the associated error.

R_{Pl} [kpc]	m	c	ϵ
1.0	−0.04	6.23	±0.6
0.5	−0.02	4.24	±0.8
0.25	−0.02	4.53	±0.6

Figure 4.4 shows the data points of the radial surface brightness by fitting an exponential profile of 12 different simulations. The 3 panels shown from left to right the R_{Pl} = 1.0 kpc (cyan circles), R_{Pl} = 0.5 kpc (purple squares) and R_{Pl} = 0.25 kpc (orange diamonds), respectively. The rows from top to bottom represent the initial size of the fractal distribution R_{frac} = 30, 70, 150 and 200 pc, respectively. The dashed lines represent the exponential profile. Here we see how the stellar mass in our final object is more concentrated at the center and decreases as we go to bigger radii with an exponential decrease being a good fit.

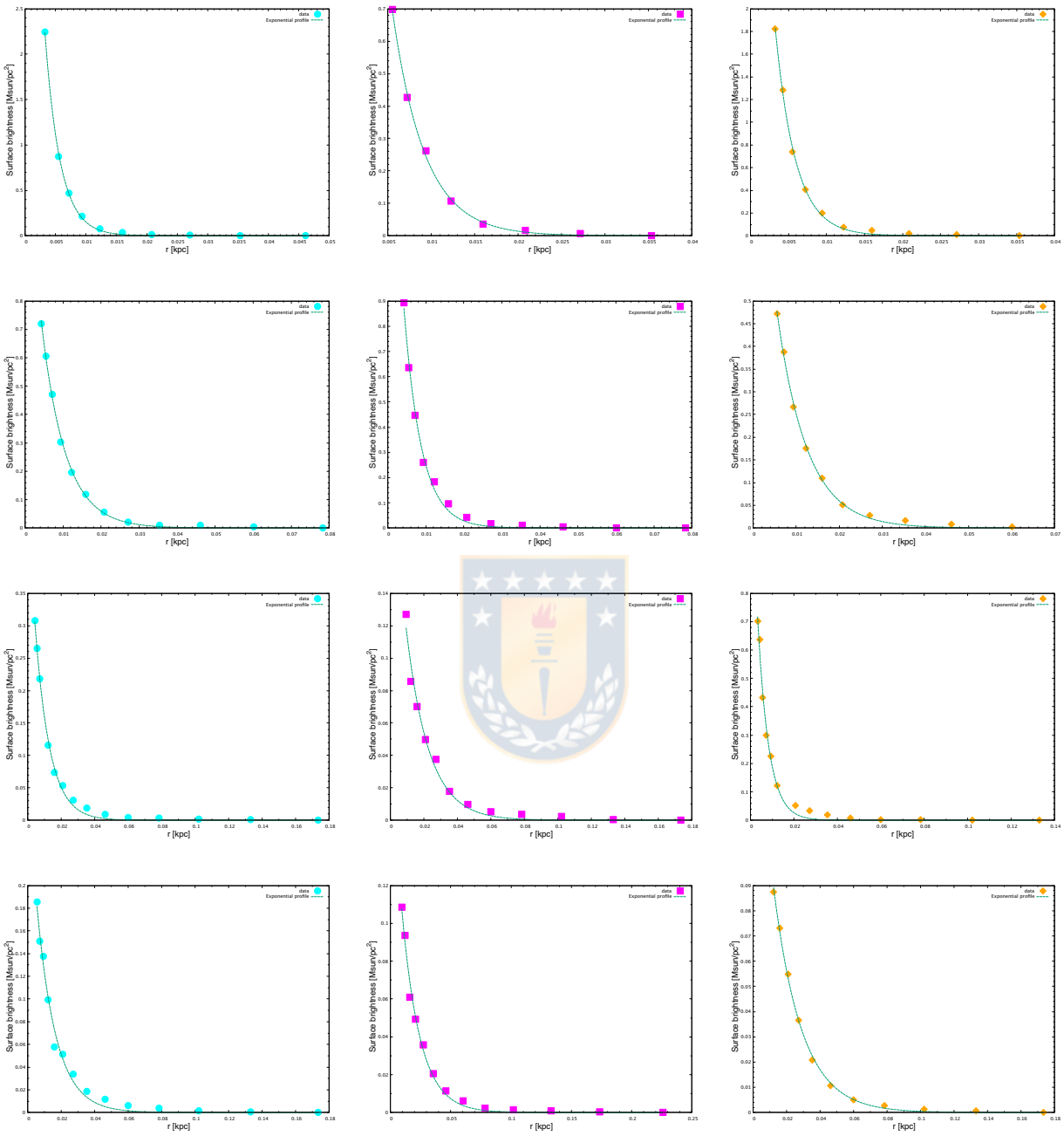

FIGURE 4.4. Fit of the data points of the radial surface brightness with an exponential profile of 12 different simulations. The 3 columns shown from left to right the R_{Pl} = 1.0 kpc (cyan circles), R_{Pl} = 0.5 kpc (purple squares) R_{Pl} = 0.25 kpc (orange diamonds), respectively. The rows from top to bottom represent the initial size of the fractal distribution R_{frac} = 30, 70, 150 and 200 pc, respectively. The dashed lines represent the exponential profile.

TABLE 4.4. Values of the linear fitting function by a least square fitting for the effective radius, R_{eff}. The first column shows the Plummer radius and m is the slope of the fitting line, c the free parameter and ϵ the associated error.

R_{Pl} [kpc]	m	c	ε
1.0	0.04	2.2	±0.97
0.5	0.04	2.2	±0.96
0.25	0.04	2.3	±0.91

4.2.1 Effective radius, R_{eff}

To obtain the effective radius, R_{eff}, we fit the data point of the radial surface brightness with an exponential profile.

In Figure 4.5 we show the effective radius as a function of the fractal radius for each Plummer distribution. The data points are mean values calculated from 10 realizations of these parameters and the dotted lines represent the data with a linear fitting function by a least squares fitting, and the results obtains for the fitting lines are shown in Table 4.4, where m is the slope of the fitting line, c the free parameter and ϵ the associated error.

From Figure 4.5 and Table 4.2 we observe the final scale-length is almost the 10% the initial scale-length of the stellar distribution. Thus, the dependency of the effective radius with the initial size of the fractal distribution is quite strong. Furthermore, we see almost no difference between the 3 Plummer distributions, at $R_{Pl} = 1$ kpc, $R_{Pl} = 0.5$ kpc and $R_{Pl} = 0.25$ kpc.

From these results we can distinguish the influence of the different initial parameters. The scale-length of the DM halo has no influence on the mean values of the exponential profile parameters. If the luminous component started more concentrated we see smaller scale-lengths in our final object and smaller scale-lengths of the fractal distribution lead a final object with higher surface density in the centre. This result can be see as a confirmation that our choice of initial Plummer radius does not affect the final outcome.

4.3 Velocity dispersion, σ_{50}

The velocity dispersion is the standard deviation for the mean velocity of the particles in the object. We calculate the velocity dispersion, σ_{50}, considering all stars within a radius of 50 pc.

We measure the line-of-sight velocity dispersion for the final object to compare them with the typical value observed in UFDs. According to Simon (2019) at the present, velocity dispersion measurements or limits for UFDs are between ~ 2 to $10\,\mathrm{km\,s^{-1}}$ (see Figure 1.10).

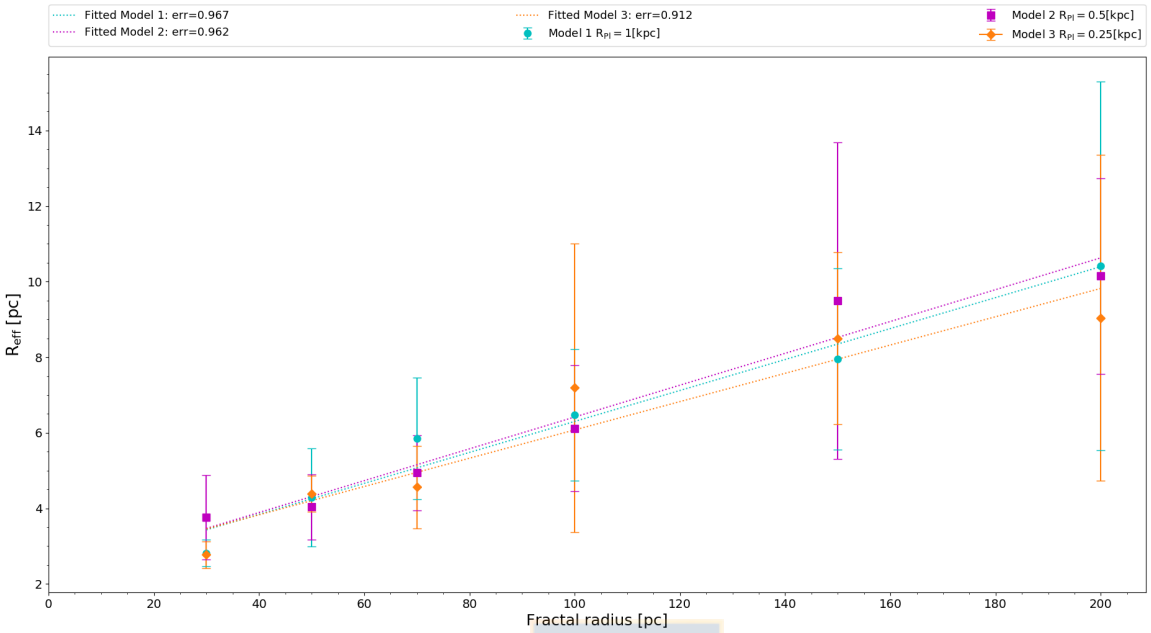

FIGURE 4.5. Effective radius as a function the initial size of the fractal for each Plummer distribution. Cyan circles represent the R_{eff} as a function of their $R_{Pl} = 1$ kpc. Purple square represent the relation between the R_{eff} with a $R_{Pl} = 0.5$ kpc and the orange diamonds represent the R_{eff} for a $R_{Pl} = 0.25$ kpc. The data point are mean values calculated from 10 realizations of these parameters and the dotted lines represent the data with a linear fitting function by a least square fitting.

Table 4.5 shows the mean values of σ_{50} for the initial size of the fractal, $R_{frac} = 30 - 50 - 70 - 100 - 150$ and 200 pc and for each Plummer distribution.

In Figure 4.6 we show the velocity dispersion of the final object as a function of the fractal radius for each Plummer distribution. The data points are mean values calculated from 10 realizations of these parameters, and the dotted lines represent the data with a linear fitting function by a least square fitting, and the results obtains for the fitting lines are shown in Table 4.6, where m is the slope of the fitting line, c the free parameter and ε the associated error.

It is possible to see there are no significant differences in the velocity dispersion with varying the Plummer distribution (see Table 4.5 and Figure 4.6) at $R_{Pl} = 1$ kpc, $\sigma_{50} = 17.342 \pm 9.7\,\mathrm{km\,s^{-1}}$, when $R_{Pl} = 0.5$ kpc and $R_{Pl} = 0.25$ kpc, then $\sigma_{50} = 15.712 \pm 8.8\,\mathrm{km\,s^{-1}}$ and $\sigma_{50} = 15.798 \pm 9.1\,\mathrm{km\,s^{-1}}$ respectively. Instead we do see a strong dependency of the velocity dispersion on the scale-length of the distribution of stars, showing an increasing trend with the fractal radius.

For smaller distributions of stars, that is, all simulations with fractal radii of 30 pc, the final objects have values similar to the measured for Segue 1 of $3.7^{+1-4}_{-1.1.}\,\mathrm{km\,s^{-1}}$ (Simon et al., 2011). Also,

TABLE 4.5. Mean velocity dispersion within 50 pc. The first column shows the Plummer radius, where Model 1, Model 2 and Model 3 represents a R_{Pl} = 1.0, 0.5, and 0.25 kpc, respectively. The second column shows the initial size of the fractal distribution and the last column shows the velocity dispersion within 50 pc of the final object.

Model	Fractal Radius pc	σ_{50} [kms^{-1}]
Model 1	30	5.92 ± 1.2
	50	8.36 ± 2.6
	70	12.33 ± 2.9
	100	18.98 ± 2.4
	150	24.39 ± 3.7
	200	34.08 ± 4.9
Model 2	30	5.67 ± 0.9
	50	7.73 ± 1.8
	70	11.11 ± 2.8
	100	16.09 ± 1.9
	150	22.89 ± 2.5
	200	30.78 ± 4.4
Model 3	30	4.89 ± 0.9
	50	8.74 ± 0.9
	70	11.08 ± 2.4
	100	15.17 ± 1.7
	150	23.61 ± 2.9
	200	31.3 ± 3.9

TABLE 4.6. Values of the linear fitting function by a least square fitting for the velocity dispersion, σ_{50}. The first column shows the Plummer radius and m is the slope of the fitting line, c the free parameter and ϵ the associated error.

R_{Pl} [kpc]	m	c	ε
1.0	0.16	0.87	± 0.99
0.5	0.15	0.87	± 0.99
0.25	0.15	0.42	± 0.99

all the simulations with fractal radii between 30 to 70 our final objects have velocity dispersion like the ones measured for some UFDs galaxies (see Table 1.2 sixth column) independent on the chosen scale-length of the DM halo.

These results show large fractal distribution scale-lengths (100 to 200 pc) exhibit velocity dispersion does not fit in the range of the UFDs galaxies and the velocity dispersion of our final object does not depend on the chosen scale-length of the dark matter halo. However, shown clearly that

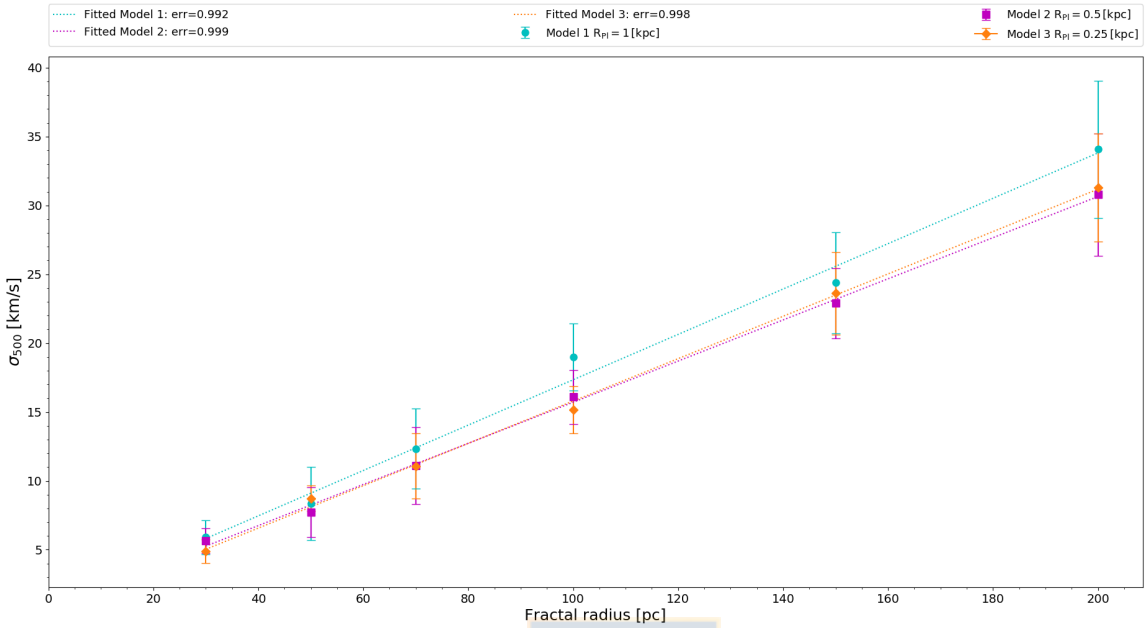

FIGURE 4.6. Velocity dispersion, σ_{50}, of the final object as a function of the fractal radius for each Plummer distribution. Cyan circles represent the σ_{50} as a function of their $R_{Pl} = 1$ kpc. Purple square represent the relation between the σ_{50} with a $R_{Pl} = 0.5$ kpc and the orange diamonds represent the σ_{50} for a $R_{Pl} = 0.25$ kpc. The data point are mean values calculated from 10 realizations of these parameters and the dotted lines represent the data with a least square fitting.

our model is well suited to reproduce galaxies like Segue 1 when we choose compact size of fractal distributions.

4.4 Shape of the final object

It is possible to characterize the shape of our resulting object ananlyzing the parameter of ellipticity, ϵ, and the distribution of stars after 5 Gyr of evolution.

4.4.1 Ellipticity

We know the ellipticity, ϵ, is a structural parameter which can help us to understood how flat is our final object. The ellipticity is given by:

$$\epsilon = 1 - \frac{b}{a},$$

where a is the semi-major axis and b the semi-minor axis of an ellipse.
To determine the ellipticity of the final object we use the ELLIPSE task under the IRAF envi-

TABLE 4.7. Derived ellipticity of the final object for each fractal distribution. The first column shows the Plummer radius, where Model 1, Model 2 and Model 3 represents a R_{Pl} = 1.0, 0.5, and 0.25 kpc, respectively. The second column shows the initial size of the fractal distribution and the last column shows the ellipticity of the final object.

Model	Fractal Radius pc	ϵ
Model 1	30	0.13 ± 0.06
	50	0.27 ± 0.1
	70	0.32 ± 0.1
	100	0.27 ± 0.1
	150	0.26 ± 0.1
	200	0.31 ± 0.1
Model 2	30	0.31 ± 0.3
	50	0.29 ± 0.1
	70	0.31 ± 0.2
	100	0.29 ± 0.2
	150	0.17 ± 0.001
	200	0.26 ± 0.1
Model 3	30	0.13 ± 0.1
	50	0.2 ± 0.1
	70	0.18 ± 0.1
	100	0.15 ± 0.1
	150	0.24 ± 0.1
	200	0.2 ± 0.1

ronment which gives the ellipticity value at different radii, i.e, looks for elliptical isophotes in the galaxy image, of all points having the same luminosity per unit area, starting from a first guess elliptical isophote defined by approximate values for the x and y centre coordinates, in our case, the density center of the final object.

In the literature it is usually considered that the faintest galaxies have significantly higher ellipticities than larger systems, with an average ellipticity for UFDs of 0.5 ± 0.01 (Martin et al., 2008), but Simon (2019) concluded that there is no significant evidence at present that UFDs have more elongated shapes than mores luminous dwarfs. Segue 1 have an ϵ value of $0.48^{+0.1}_{-0.13}$ (Martin et al., 2008).

Table 4.7 shows the mean values of ϵ for the initial size of the fractal, $R_{frac} = 30 - 50 - 70 - 100 - 150$ and 200 pc and for each Plummer distribution of the DM halo.

TABLE 4.8. Mean ellipticity of the final object for each Plummer distribution.

R_{Pl} [kpc]	ϵ
1.0	0.259 ± 0.1
0.5	0.273 ± 0.05
0.25	0.185 ± 0.04

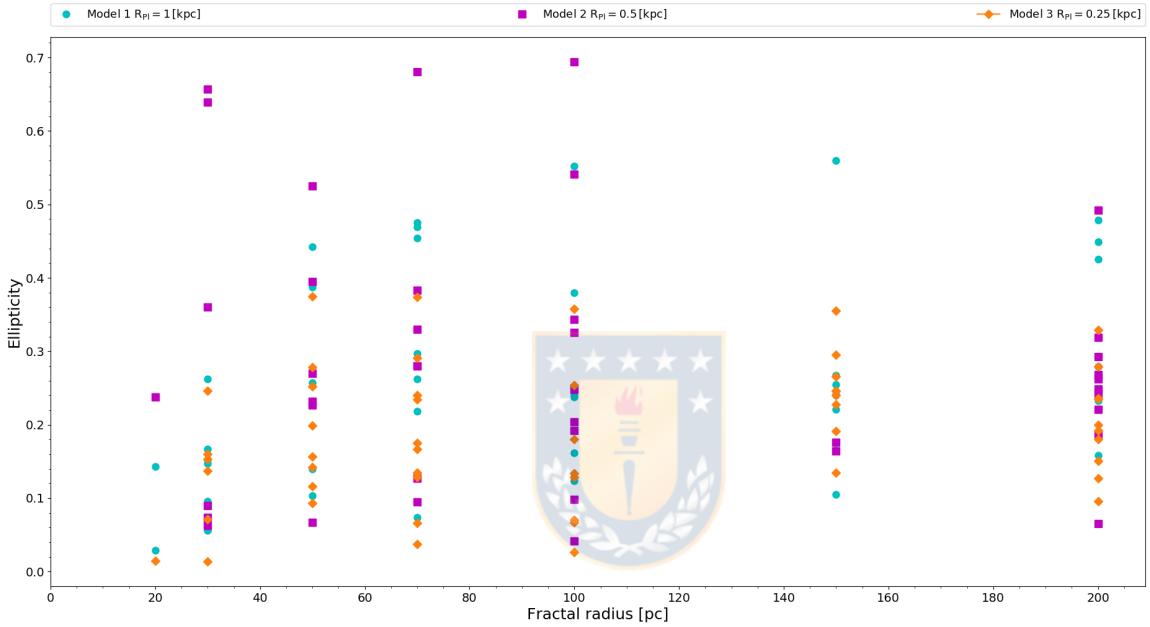

FIGURE 4.7. Ellipticity of the final object after 5 Gyr of evolution as a function of the initial fractal distribution of stars. Cyan circles are the results for a $R_{Pl} = 1$ kpc, purple squares are the results for a $R_{Pl} = 0.5$ kpc, while the orange diamonds are the results for a $R_{Pl} = 0.25$ kpc.

Figure 4.7 shows the ellipticity values against the initial size of the fractal for each Plummer distribution after 5 Gyr of evolution. Cyan circles are the results for a Plummer distribution with a $R_{Pl} = 1$ kpc, purple squares are the results for a Plummer distribution with a $R_{Pl} = 0.5$ kpc, while the orange diamonds are the results for a Plummer distribution with a $R_{Pl} = 0.25$ kpc. Here we clearly notice that there is no correlation between the ellipticity of the final object and the size of the DM halo, i.e, the ellipticity values are independent of our choice of the DM halo. Furthermore we see no trend with the initial size of the fractal. This means that the final ellipticity of our objects is a simple by-chance result and does not depend on any initial parameter.

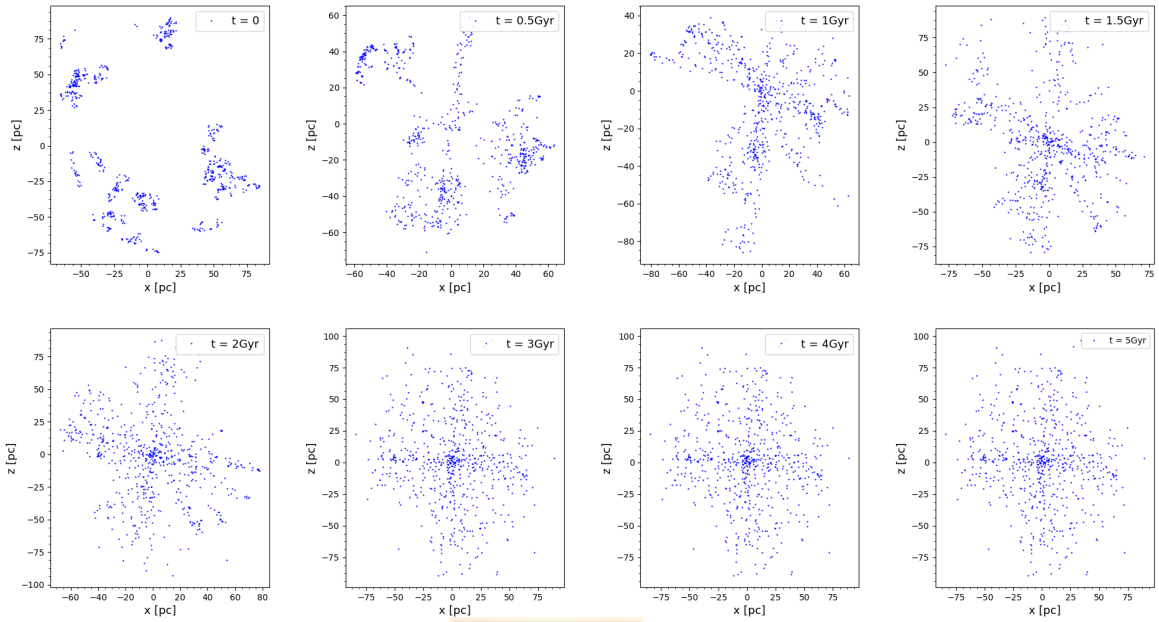

FIGURE 4.8. Example of time-evolution of the distribution of stars from t = 0 to t = 5 Gyr. The blue points represent the stars ($M_\star = 0.5\ M_\odot$) in virial equilibrium, with a fractal distribution of D = 1.6 in a radius of $r_{fractal} = 100$ pc and $R_{Pl} = 0.5$ kpc. We observe how the initially very clumpy distribution collapses. At first the larger of these clumps then attract nearby clumps. The initial clumpiness is erased as most clumps merge at centre at first 3 Gyr, after that time the distribution of stars remains stable.

We observe that the ellipticity of the final object seems not to follow any trend, also, we observe no dependence between ϵ and the initial size of the fractal distribution, is interesting to observe that the final object obtained in almost all the simulations have ellipticities in the range of 0.1 to 0.3, more similar to the weighted average ellipticity of the classical dSphs of 0.350 ± 0.003 proposed by Martin et al. (2008). However Muñoz et al. (2018) measured different structural parameters for Segue 1, and proposed an ellipticity $\epsilon = 0.31 \pm 0.13$ which is closer to the values obtained when we use a Plummer distributions of 1 kpc and 0.5 kpc, independent of our choice of fractal distribution (see Table 4.8).

4.4.2 Distribution of stars

As we showed before, models with the stars initially in a more concentrated distribution, i.e. smaller fractal distribution, generate final objects with smaller scale-lengths independent of our choice of the initial Plummer distribution for the DM halo, as we see in Figure 4.9. We show the final distribution of stars of 12 simulations with different combination of initial parameters.

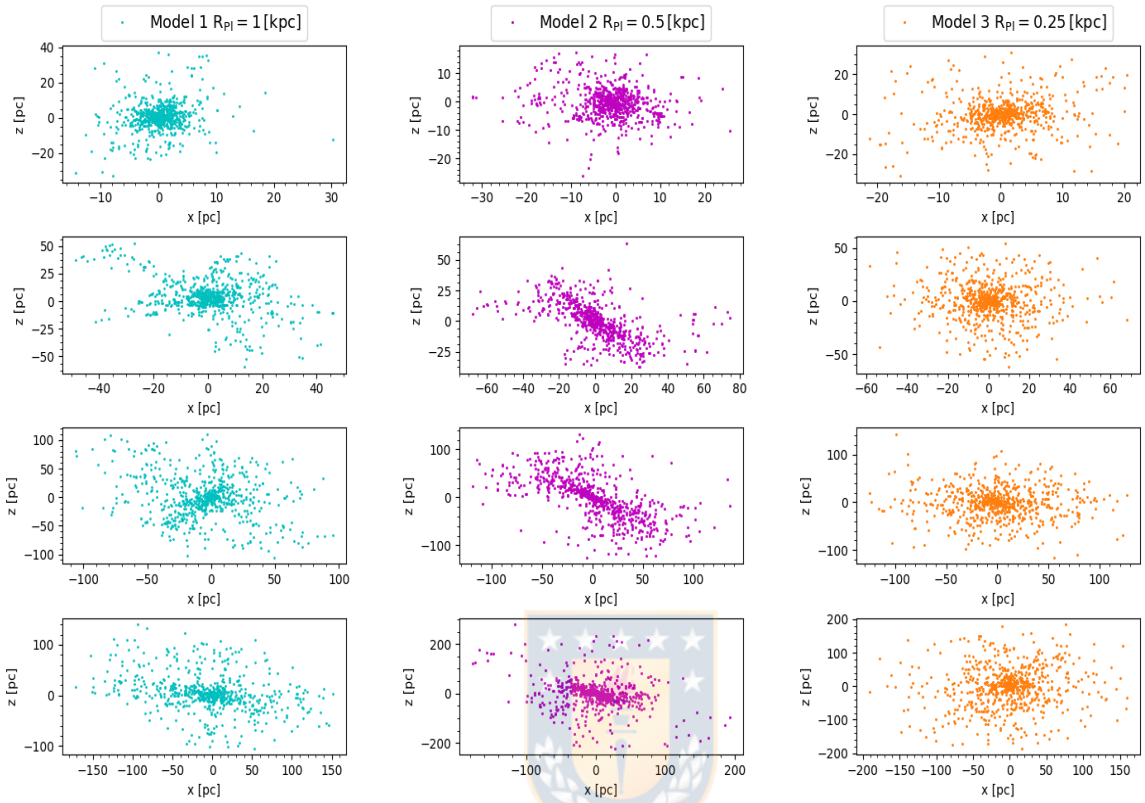

FIGURE 4.9. Distribution of stars after 5 Gyr of evolution. The 3 columns shown from left to right the final distribution of stars for a R_{Pl} = 1.0 kpc (cyan dots), R_{Pl} = 0.5 kpc (purple dots) and R_{Pl} = 0.25 kpc (orange dots), respectively. The rows from top to bottom represent the initial size of the fractal distribution R_{frac} = 30, 70, 150 and 200 pc, respectively.

Cyan circles, purple squares and orange diamonds represents a Plummer distribution with a R_{Pl} = 1.0, 0.5 and 0.25 kpc, respectively, and from top to bottom represent the initial size of the fractal distribution R_{frac} = 30, 70, 150 and 200 pc. It is possible notice how as we increase the initial size of the fractal distribution the final size of the stellar distribution also increases. We can also observe that the size of the final stellar distribution does not change with respect to the size initially selected.

It is interesting to see how the initially very clumpy distribution collapses, until the initial clumpiness is erased as most clumps merge after 5 Gyr as we show in Figure 4.8. Where we show a time-evolution example of the distribution of stars from t = 0 to t = 5 Gyr. We observe how at first the larger of these clumps then attract nearby clumps. The initial clumpiness is erased as most clumps merge at centre at first 3 Gyr, after that time the distribution of stars remains quasi-stable.

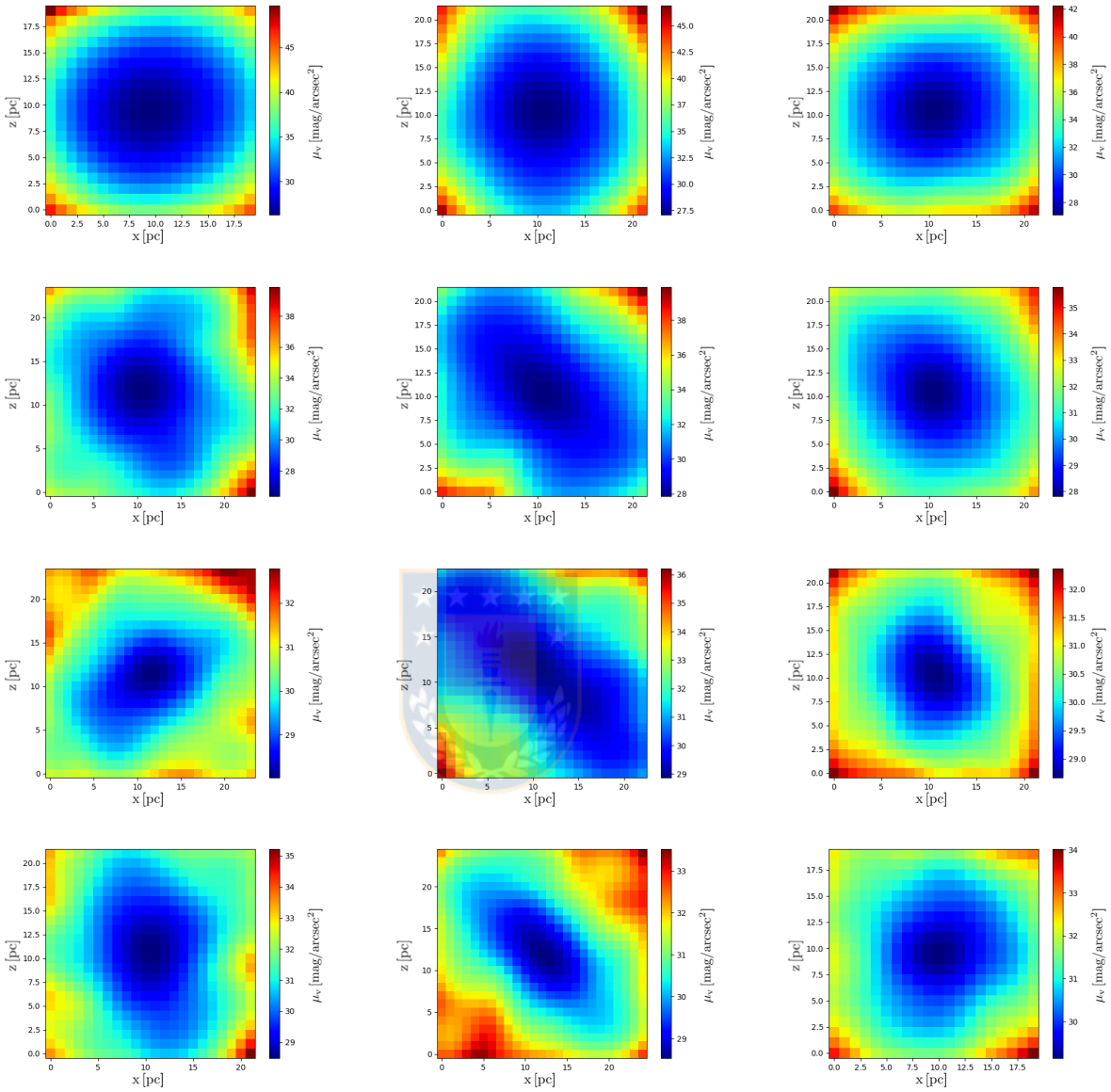

FIGURE 4.10. Final object until a radius of 50 pc. Shape of the final object within a colour bar for the magnitude of the surface brightness. The 3 columns shown from left to right the shape of the final object for a R_{Pl} = 1.0, 0.5 and 0.25 kpc, respectively. The rows from top to bottom represent the initial size of the fractal distribution R_{frac} = 30, 70, 150 and 200 pc, respectively.

Figure 4.10 show the shape of our final objects until a radius of 50 pc of 12 simulations with different combinations of the initial parameters, R_{Pl} and R_{frac}. These panels show clearly a centrally peaked and smoothed density distribution for the luminous component of our final object. They show different outcomes from our simulation, a nearly spherical final object and a very elongated final object,in both cases the initial clumpiness is erased. On the other hand,

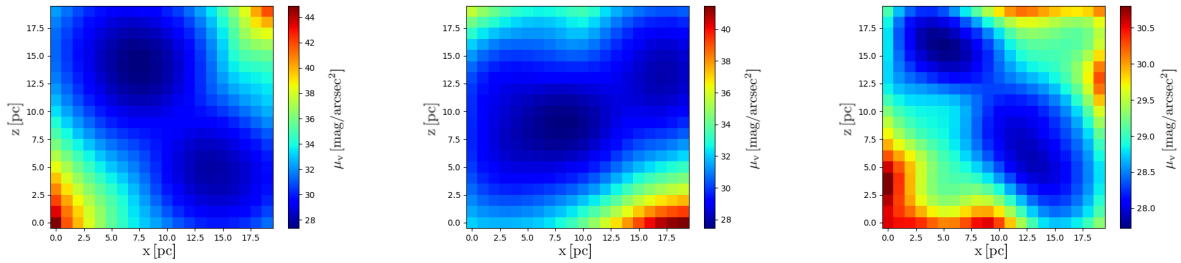

FIGURE 4.11. Final object until a radius of 50 pc. Shape of the double-cored final object with two high-density peaks in the centre within a colour bar for the magnitude of the surface brightness. The 3 columns shown from left to right the shape of the final object for a R_{frac} = 30, 50 and 70 pc, respectively and R_{Pl} = 1.0 kpc.

Figure 4.11 shows a double-cored final object with two high-density peaks in the centre. This result could be mainly due to the fact that the stellar distributions still out of the quasi-stable configuration.

Figure 4.13 show the distribution of high-density peaks against the initial parameters. We find that is more probably to obtain the clumpy structures or double-cored final objects when we chose a large halo scale-length and smaller fractal distributions.

This results show our model is able to predict objects with different shapes independent of initial conditions and large halo scale-lengths exhibit stellar distributions still out of equilibrium after 5 Gyr as we see in Figure 4.12. We show an example of time-evolution of the 50% Lagrangian radii throughout 5 Gyr of evolution of 3 different simulations with the same initial stellar distribution, i.e. $M_\star = 0.5\ M_\odot$ in virial equilibrium, with a fractal distribution of D = 1.6 and R_{frac} = 100 pc but different Plummer radius, 1.0 kpc (cyan circles), 0.5 kpc (purple squares) and 0.25 kpc (orange diamonds).

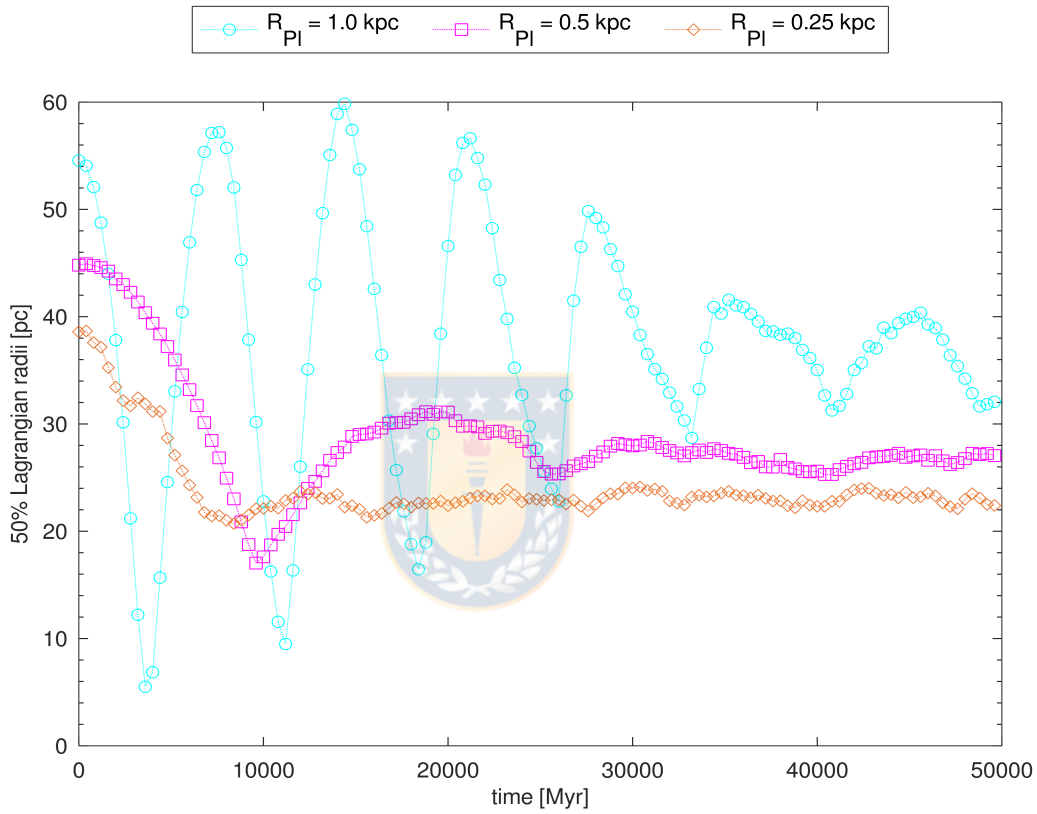

FIGURE 4.12. Time-evolution of the 50% Lagrangian radii throughout 5 Gyr of evolution. We show 3 different simulations with the same initial stellar distribution, i.e. $M_\star = 0.5\ M_\odot$ in virial equilibrium, with a fractal distribution of D = 1.6 and $R_{frac} = 100$ pc but different Plummer radius, 1.0 kpc (cyan circles), 0.5 kpc (purple squares) and 0.25 kpc (orange diamonds). This results show our model is able to predict objects with different shapes independent of initial conditions and large halo scale-lengths exhibit stellar distributions still out of equilibrium after 5 Gyr

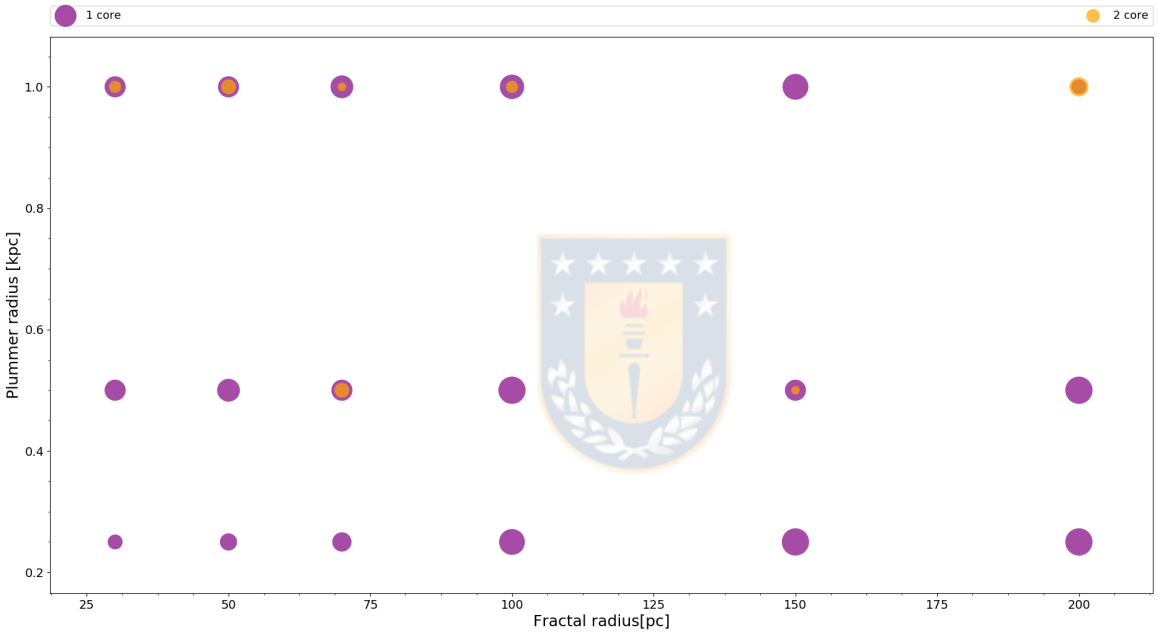

FIGURE 4.13. Distribution of high-density peaks against the initial parameters R_{frac} and R_{Pl}.Purple color represent the final object with one density core independent of their shape and orange color shows in what configurations we found final objects with two high-density peaks in the centre. The size of the circles represent how many simulations present the same result.

CHAPTER 5

SUMMARY AND CONCLUSIONS

We test the possible formation scenario for dSph galaxies, originally proposed by Assmann et al. (2013a), for the formation of UFDs galaxies. We model Segue 1 by performing numerical simulations using AMUSE and the direct N-body integrator ph4. In our simulations we consider the evolution of different fractal distributions of 700 particles within an analytical DM halo with a Plummer distribution. The simulations have been repeated using a different random number seeds to explore the variations of the properties of the object formed from 10 different realizations of the same initial conditions. In total we perform 180 simulations.
Every simulation performed in this work leads through the dissolving star cluster model, to a final quasi-stable object with characteristics of UFDs galaxies:

- The analysis of the Lagrangian radii show that while we increases the Plummer distribution scale-length the final object needs more time to stabilize independent of the fractal distribution initially selected.
  The size of the final object does not depend on the chosen R_{Pl} but only on the size of the initial fractal. Thus, the size of Segue 1 does not reflect the halo scale-length. To obtain a similar scale-length as Segue 1, we need fractal distributions of $70 - 100$ pc in size.
  We would like to add a word of caution, as the results may depend on the fact, that we only used cored DM haloes in our study.

- We use an exponential profile to study the surface density and effective radius of our final object. This parametrization is known to provide a good representation of the brightness profiles of early-type galaxies, including low-mass dSph galaxies. By analyzing the two parameters of the exponential profile we find a dependency: I_e decreases if we use to larger stellar distribution size, i.e. smaller sizes of the fractal distribution lead to a final object with higher density in the centre. On the other hand, the R_{eff} is in the range of 2.7 to 10.4

pc, which is much smaller compare with the derived by Muñoz et al. (2018) of 26.4 ± 4 pc using a Sersic model and the estimated by Domínguez et al. (2016) of $29^{+8.0}_{-5.0}$ pc.

- The range of velocity dispersion in our simulations is between 4.9 to 34.1 $\mathrm{km\,s^{-1}}$, and the derived intrinsic velocity dispersion for Segue 1 by Simon (2019) is $3.7^{+1.4}_{-1.1}$ $\mathrm{km\,s^{-1}}$. This means, our simulations with an initial fractal distribution of 30 pc present a velocity dispersion close to the estimated value and all simulations with fractal radii between 30 to 70 pc are in the range of UFDs (2 to 10 $\mathrm{km\,s^{-1}}$ independent on the chosen scale-length of the DM halo.

- The ellipticity of our final objects is in the range of 0.1 to 0.3, and the the ϵ proposed for Segue 1 is 0.31 ± 0.13. Thus, almost all simulation with Plummer distribution of 1.0 and 0.5 kpc, independent of the chosen scale-length of the fractal distribution are consistent with the estimated value (Muñoz et al., 2018). Only the simulations with initial Plummer distribution of 0.25 kpc lead to objects with ϵ slightly smaller than this value.

- By analyzing the results of the distribution of stars we conclude our model is able to predict objects with different shapes independent of the initial conditions. We obtained from our simulations nearly spherical final objects, very elongated final objects and a double-cored final objects. Also, we conclude that larger halo scale-lengths exhibit stellar distributions which are still out of equilibrium after 5 Gyr.

There are some disadvantages, or behaviors that we can not reproduce or consider in our model. We only perform simulations using a Plummer potential for the DM halo. Also, we can not treat metalicities, or an explication for any star formation or chemical-enrichment history of Segue 1. We perform simulations that treat only kinematics of the particles.
From our analysis of the central surface brightness and the exponential profile, we observe the stellar mass of our final object is more concentrated in the center and decreases as we go to bigger radii with an exponential decrease being a good fit.
Our models reproduce very well some structural and kinematical properties of Segue 1, when we chose the initial fractal radius between 70 to 100 pc, e.g patchy structure, ellipticity and effective radius. This possible formation scenario could be a good model to explain Segue 1.

APPENDIX A

AMUSE SCRIPT

```
#!/home/dmatus/bin/amuse

import os
import sys
import time

from amuse.datamodel import Particles, Particle
from amuse.units import constants, units, nbody_system
from os.path import isfile
from amuse.community.ph4.interface import ph4Interface, ph4
#from amuse.community.huayno.interface import Huayno

from amuse.couple import bridge #Potencial analitico
#from amuse.lab import *
from amuse.ic import plummer

import matplotlib.pyplot as plt
import numpy as np
import math
from amuse.lab import *

#Cosas para los snapshots:
from snapshots import print_snapshot, Time_stuff
from time import time, strftime, gmtime

#from snapshots import * #guardar archivos

class Potential(object):

```

```
30          def print_snapshot(t, N, tcpu0, stars, fo):
31                  tcpu = time()-tcpu0
32                  header = str(t) + " " + str(N) + " " + str(tcpu) + "\n"
33                  fo.write(header)
34                  for s in stars:
35                          line = ""
36                          line += str(s.mass.value_in(units.MSun))   + " " #Mass
     of star
37                          line += str(s.radius.value_in(units.RSun)) + " " #
    stars radius
38                          #line += str(s.x.value_in(units.kpc))    + " " #
    Position
39                          #line += str(s.y.value_in(units.kpc))    + " "
40                          #line += str(s.z.value_in(units.kpc))    + " "
41                          line += str(s.x.value_in(units.parsec))    + " " #
    Position
42                          line += str(s.y.value_in(units.parsec))    + " "
43                          line += str(s.z.value_in(units.parsec))    + " "
44                          #line += str(s.x.value_in(units.AU))    + " " #
    Position
45                          #line += str(s.y.value_in(units.AU))    + " "
46                          #line += str(s.z.value_in(units.AU))    + " "
47                          line += str(s.vx.value_in(units.kms))      + " " #
    Velocity
48                          line += str(s.vy.value_in(units.kms))      + " "
49                          line += str(s.vz.value_in(units.kms))      + "\n"
50                          fo.write(line)
51                  fo.write("\n")
52                  fo.flush()
53
54  def __init__(self, Rv=1.7|units.kpc, M=2.15e10|units.MSun):
55    self.M = M
56    self.Rv = Rv
57    self.a = self.Rv*(3*math.pi/16)
58    self.a2 = self.a**2
59
60
61
62  def get_gravity_at_point(self, Rv, x, y, z):
63    r2 = x**2 + y**2 + z**2
64    r = r2.sqrt()
65
66    ace = (constants.G*M*r)/(r**2 + self.a**2)**(3./2)
67
68    ax = -x/r*ace
69    ay = -y/r*ace
70    az = -z/r*ace
```

```
71
72      return ax, ay, az
73
74    def get_density_at_point(self, x, y, z):
75      r2 = x**2 + y**2 + z**2
76      r = r2.sqrt()
77
78      #Perfil de densidad
79      rho = ((3.*self.M)/(4*math.pi))*(self.a2/(r2 + self.a2)**(5./2))
80
81      return rho
82
83    def potential_at_point(self, x,y, z):
84      r2 = x**2 + y**2 + z**2
85      r = r2.sqrt()
86
87      phi = -(constants.G*self.M)/(r2 + self.a2).sqrt()
88
89      return phi
90
91    def fix_velocities(stars):
92
93      for i in stars:
94        Lz = (i.y*i.vx)-(i.x* i.vy)
95
96        if Lz<0:# .value_in(units.m**2/(units.s))<0:
97          i.vx *= -1
98          i.vy *= -1
99
100       stars_omega = i
101
102       return stars_omega  #significa que es i.xx, i.yy, i.zz, i.vx etc.
103
104 # Inicializo variables para simulacion
105
106 #Number of particles
107 N = 700
108
109 stars=Particles(N)
110
111 #Radius virial
112 R = 1.7 | units.kpc
113
114 #Total mass
115 M = 2.15e10 | units.MSun
116
117
```

```
# Llamamos archivo de distribucion fractal
stars_file = np.loadtxt('mf10.txt')

# asignamos la distribucion fractal con clase stars
#Position of the stars
stars.x = stars_file[:,0] |units.parsec
stars.y = stars_file[:,1] |units.parsec
stars.z = stars_file[:,2] |units.parsec

#Velocities of the stars
stars.vx =  stars_file[:,3] |units.km/units.s
stars.vy =  stars_file[:,4] |units.km/units.s
stars.vz =  stars_file[:,5] |units.km/units.s

stars.mass = stars_file[:,6] |units.MSun
stars.radius = 0.5 |units.RSun
# Calcular fix_velocities
#fix_velocities(stars) #Bota stars_omega con momento agular positivo

#Calcular Plummer
convert_nbody = nbody_system.nbody_to_si(1.0 |units.kpc, 2.15e10 |units.MSun)

#stars=plummer.new_plummer_model(N,convert_nbody)
#print "Stars:", starsstars.scale_to_standard(convert_nbody,virial_ratio=0.5)
#fix_velocities(stars)

#Time of simulation
t_envolve = 0|units.yr
t_end = 5000.0 |units.Myr

#snapshot dt
dt_snapshot = 0.1 |units.Myr

#Bridge dt
dt = 0.1 |units.Myr

salida = open("sim10.txt", "w")

#PH4
print 'inicio ph4'
grav = ph4(convert_nbody, number_of_workers=1, mode='gpu')

grav.initialize_code()
print 'initialize'
grav.particles.add_particles(stars)
print 'add-particles'
grav.commit_particles()
```

```
print 'particles'
channel_from_grav_to_stars = grav.particles.new_channel_to(stars)

channel_from_stars_to_grav = stars.new_channel_to(grav.particles)
print 'channel'
#Setup Background Potential
background_potential = Potential(Rv=R, M=M)

integrator = bridge.Bridge(verbose=False)
print 'bridge'
integrator.add_system(grav, (background_potential,),True)
integrator.timestep = dt

print integrator.timestep

t_snapshot = dt_snapshot

print t_snapshot

tcpu0 = time()

d_t = 0.1 |units.Myr

t_evolve=0.0 | units.Myr

while t_evolve < t_end :
  if isfile('stop'):
    break

  print t_evolve.value_in(units.yr),"/",t_end.value_in(units.yr)
  print t_evolve

  integrator.evolve_model(t_evolve)
  integrator.synchronize_model()

# t_evolve = integrator.model_time + d_t
  integrator.model_time
# t_evolve = t_evolve + d_t
  print integrator.model_time

  channel_from_grav_to_stars.copy_attributes(['x','y','z','vx','vy','vz'])

  if t_evolve >= t_snapshot:
      t_snapshot += dt_snapshot
    print_snapshot(t_evolve.value_in(units.Myr),N, tcpu0, stars, salida)
    Time_stuff(tcpu0,t_evolve,t_end,"cuanto_queda")
    #print_one_snapshot(t_evolve.value_in(units.yr),0, tcpu0, stars, salida.
```

```
    flush())
212
213   t_evolve = t_evolve + d_t
214
215 integrator.stop()
```

BIBLIOGRAPHY

P. Assmann, M. Fellhauer, M. I. Wilkinson, and R. Smith.
A possible formation scenario for dwarf spheroidal galaxies - i. fiducial model.
MNRAS, 432(1):274–284, 2013a.

James Binney and Scott Tremaine.
Galactic Dynamics.
Princeton series in astrophysics. Princeton University Press, 1987.
ISBN 9780691084459.

F. Vincenzo, F. Matteucci, S. Vattakunnel, and G. A Lanfranchi.
Chemical evolution of classical and ultra-faint dwarf spheroidal galaxies.
MNRAS, 441(4):2815–2830, 2014.

Ilse De Looze, Maarten Baes, George J. Bendo, Jacopo Fritz, Médéric Boquien, Diane Cormier, Gianfranco Gentile, Robert C. Kennicutt, Suzanne C. Madden, Matthew W. L. Smith, and Lisa Young.
The interstellar medium in andromeda's dwarf spheroidal galaxies ‚Äì i. content and origin of the interstellar dust.
MNRAS, 459(4):3900–3916, 2016.

Eline Tolstoy, Vanessa Hill, and Monica Tosi.
Star-formation histories, abundances, and kinematics of dwarf galaxies in the local group.
Annual Review of Astronomy & Astrophysics, 47(1):371–425, 2009.

Andreas Koch, Mark I. Wilkinson, Jan T. Kleyna, Mike Irwin, Daniel B. Zucker, Vasily Belokurov, Gerard F. Gilmore, Michael Fellhauer, and N. Wyn Evans.
A spectroscopic confirmation of the bootes ii dwarf spheroidal.
ApJ, 690(1):453–462, 2008.

Mihai Tomozeiu, Lucio Mayer, and Thomas Quinn.
The evolution of dwarf galaxy satellites with different dark matter density profiles in the erismod simulations. i. the early infalls.
ApJ, 818(2):21, 2016.

L. Mayer, S. Kazantzidis, C. Mastropietro, and J. Wadsley.
Early gas stripping as the origin of the darkest galaxies in the universe.
Nat, 445:738–740, 2007.

Elena D'Onghia, Gurtina Besla, Thomas J. Cox, and Lars Hernquist.
Resonant stripping as the origin of dwarf spheroidal galaxies.
Nat, 460:605–607, 2009.

Till Sawala, Cecilia Scannapieco, Umberto Maio, and Simon White.
Formation of isolated dwarf galaxies with feedback.
MNRAS, 402(3):1599–1613, 2010.

Charles J. Lada and Elizabeth A. Lada.
Embedded clusters in molecular clouds.
AAR&A, 41:57–115, 2003.

P. Assmann, M. Fellhauer, M. I. Wilkinson, R. Smith, and M. Blaña.
A possible formation scenario for dwarf spheroidal galaxies - ii. a parameter study.
MNRAS, 435(3):2391–2406, 2013b.

A. G. Alarcón Jara, M. Fellhauer, D. R. Matus Carrillo, P. Assmann, F. Urrutia Zapata, J. Hazeldine, and C. A. Aravena.
A possible formation scenario for dwarf spheroidal galaxies - iii. adding star formation histories to the fiducial model.
MNRAS, 473(4):5015–5025, 2018.

Sakurako Okamoto, Nobuo Arimoto, Yoshihiko Yamada, and Masato Onodera.
Stellar populations and structural properties of ultra faint dwarf galaxies, canes venatici i, bootes i, canes venatici ii, and leo iv.
ApJ, 744(2):96, 2011.

Erik J. Tollerud, James S. Bullock, Genevieve J. Graves, and Joe Wolf.
From galaxy clusters to ultra-faint dwarf spheroidals: A fundamental curve connecting dispersion-supported galaxies to their dark matter halos.
ApJ, 726(2):108, 2011.

Thomas M. Brown, Jason Tumlinson, Marla Geha, Evan N. Kirby, Don A. VandenBerg, Ricardo R. Muñoz, Jason S. Kalirai, Joshua D. Simon, Roberto J. Avila, Puragra Guhathakurta, and et al.
The primeval populations of the ultra-faint dwarf galaxies.
ApJ Letters, 753(1):L21, 2012.

Alexander P. Ji, Joshua D. Simon, Anna Frebel, Kim A. Venn, and Terese T. Hansen.

Chemical abundances in the ultra-faint dwarf galaxies grus i and triangulum ii: Neutron-capture elements as a defining feature of the faintest dwarfs.
ApJ, 870(2):83, 2019.

D. Q. Nagasawa, J. L. Marshall, T. S. Li, T. T. Hansen, J. D. Simon, R. A. Bernstein, E. Balbinot, A. Drlica-Wagner, A. B. Pace, L. E. Strigari, and et al.
Chemical abundances analysis of three $\alpha-$poor, metal-poor stars in the ultrafaint dwarf galaxy horologium i.
ApJ, 852(2):99, 2018.

Beth Willman, Julianne J. Dalcanton, David Martinez-Delgado, Andrew A. West, Michael R. Blanton, David W. Hogg, J. C. Barentine, Howard J. Brewington, Michael Harvanek, S. J. Kleinman, and et al.
A new milky way dwarf galaxy in ursa major.
ApJ, 626(2):L85–L88, 2005a.

Ricardo R. Muñoz, Marla Geha, and Beth Willman.
Turning the tides on the ultra-faint dwarf spheroidal galaxies: Coma berenice and ursa major ii.
ApJ, 140(1):138–151, 2010.

Vasily Belokurov.
Galactic archaeology: The dwarfs that survived and perished.
New Ast. Reviews, 57(3–4):3100–121, 2013.

Nitya Kallivayalil, Laura V. Sales, Paul Zivick, Tobias K. Fritz, Andrés Del Pino, Sangmo Tony Sohn, Gurtina Besla, Roeland P. van der Marel, Julio F. Navarro, and Elena Sacchi.
The missing satellites of the magallanic clouds? gaia proper motions of the recently discovered ultra-faint galaxies.
ApJ, 867(1):19, 2018.

Blair C. Conn, Helmut Jerjen, Dongwon Kim, and Mischa Schirmer.
On the nature of ultra-faint dwarf galaxy candidates. i. DES1, eridanus III, and tucana v.
ApJ, 852(2):68, 2018.

Ben Moore, Sebastiano Ghigna, Fabio Governato, George Lake, Thomas Quinn, Joachim Stadel, and Paolo Tozzi.
Dark matter substructure within galactic halos.
ApJ, 524(1):L19–L22, 1999.

P. Francois, L. Monaco, P. Bonifacio, C. Moni Bidin, D. Geisler, and L. Sbordone.
Abundance ratios of red giants in low-mass ultra-faint dwarf spheroidal galaxies.
A&A, 588(A7), 2016.

Anatoly Klypin, Andrey V. Kravtsov, Octavio Valenzuela, and Francisco Prada.
Where are the missing galactic satellites?
ApJ, 522(1):82–92, 1999.

Joshua D. Simon and Marla Geha.
The kinematic of the ultra-faint milky way satellites: Solving the missing satellite problem.
ApJ, 670(1):313–331, 2007.

James S. Bullock, Andrey V. Kravtsov, and David H. Weinberg.
Reionization and the abundance of galactic satellites.
ApJ, 539(2):517–521, 2000.

Massimo Ricotti and Nickolay Y. Gnedin.
Formation histories of dwarf galaxies in the local group.
ApJ, 629(1):259–267, 2005.

Thomas M. Brown, Jason Tumlinson, Marla Geha, Joshua D. Simon, Luis C. Vargas, Don A. VandenBerg, Evan N. Kirby, Jason S. Kalirai, Roberto J. Avila, Mario Gennaro, and et al.
The quenching of the ultra-faint dwarf galaxies in the reionization era.
ApJ, 796(2):91, 2014.

Mohammadtaher Safarzadeh, Enrico Ramirez-Ruiz, Jeff. J. Andrews, Phillip Macias, Tassos Fragos, and Evan Scannapieco.
r-process enrichment of the ultra-faint dwarf galaxies by fast-merging double-neutron stars.
ApJ, 872(1):105, 2019.

Myung Gyoon Lee, In Sung Jang, Rachael Beaton, Mark Seibert, Giuseppe Bono, and Barry Madore.
The carnegie-chicago hubble program: Discovery of the most distant ultra-faint dwarf galaxy in the local universe.
ApJ, 835(2):L27, 2017.

Harlow Shapley.
A stellar system of a new type.
Harvard College Observatory Bulletin, 908:1–11, 1938.

M. J. Irwin, P. S. Bunclark, M. T. Bridgeland, and R. G. McMahon.
A new satellite galaxy of the milky way in the constellation of sextans.
MNRAS, 244:16–19, 1990.

Joshua D. Simon.
The faintest dwarf galaxies.
Annual Review of Astronomy and Astrophysics, 57:375,Äì–415, 2019.

Beth Willman, Michael R. Blanton, Andrew A. West, Julianne J. Dalcanton, David W. Hogg, Donald P. Schneider, Nicholas Wherry, Brian Yanny, and Jon Brinkmann.
A new milky way companion: Unusual globular cluster or extreme dwarf satellite?
AJ, 129(6):2692–2700, 2005b.

Louis E. Strigari, James S. Bullock, Manoj Kaplinghat, Joshua D. Simon, Marla Geha, Beth Willman, and Matthew G. Walker.
A common mass scale for satellite galaxies of the milky way.
Nature, 454(7208):1096–1097, 2008.

Mohammadtaher Safarzadeh, Alexander P Ji, Gregory A Dooley, Anna Frebel, Evan Scannapieco, Facundo A Gómez, and Brian W O'Shea.
Selecting ultra-faint dwarf candidate progenitors in cosmological n-body simulations at high redshifts.
MNRAS, 476(4):5006–5015, 2018.

B. Willman and J. Strader.
"galaxy," defined.
AJ, 144(3):76, 2012.

Evan N. Kirby, Joshua D. Simon, Marla Geha, Puragra Guhathakurta, and Anna Frebel.
Uncovering extremely metal-poor stars in the milky way's ultrafaint dwarf spheroidal satellite galaxies.
ApJ, 685(1):L43–L46, 2008.

Ricardo R. Muñoz, Jeffrey L. Carlin, Peter M. Frinchaboy, David L. Nidever, Steven R. Majewski, and Richard J. Patterson.
Exploring halo substructure with giant stars: The dynamics and metallicity of the dwarf spheroidal in boötes.
ApJ, 650(1):L51–L54, 2006.

N. F. Martin, R. A. Ibata, S. C. Chapman, M. Irwin, and G. F. Lewis.
A keck/deimos spectroscopic survey of faint galactic satellites: searching for the least massive dwarf galaxies.
MNRAS, 380(1):281–300, 2007.

Nicolas F. Martin, Jelte T. A. de Jong, and Hans-Walter Rix.
A comprehensive maximum likelihood analysis of the structural properties of faint milky way satellites.
ApJ, 684(2):1075 – 1092, 2008.

Ricardo R. Muñoz, Patrick Côté, Felipe A. Santana, Marla Geha, Joshua D. Simon, Grecco A. Oyarzún, Peter B. Stetson, and S. G. Djorgovski.

A MegaCam survey of outer halo satellites. III. photometric and structural parameters.
ApJ, 860(1):66, 2018.

D. B. Zucker, V. Belokurov, N. W. Evans, J. T. Kleyna, M. J. Irwin, M. I. Wilkinson, M. Fellhauer, D. M. Bramich, G. Gilmore, H. J. Newberg, and et al.
A curious milky way satellite in ursa major.
ApJ, 650(2):L41–L44, 2006.

Ewa L. Lokas, Stelios Kazantzidis, and Lucio Mayer.
How to make an ultra-faint dwarf spheroidal galaxy: Tidal stirring of disk dwarfs with shallow dark matter density profiles.
ApJ Letters., 751(1):L15, 2012.

F. I. Pelupessy, A. van Elteren, N. de Vries, S. L. W. McMillan, N. Drost, and S. F. Portegies Zwart.
The astrophysical multipurpose software environment.
A&A, 557(1):A84, 2013.

S. P. Goodwin and A. P. Whitworth.
The dynamical evolution of fractal star clusters: The survival of substructure.
A&A, 413(3):929–937, 2004.

Stephen McMillan, Simon Portegies Zwart, Arjen van Elteren, and Alfred Whitehead.
Simulations of dense stellar systems with the amuse software toolkit.
Astronomical Society of the Pacific, 453:129, 2012.

Simon Portegies Zwart and Steve McMillan.
Astrophysical Recipes.
2514-3433. IOP Publishing, 2018.
ISBN 978-0-7503-1320-9.

S. Portegies Zwart, S. L. W. McMillan, E. van Elteren, I. Pelupessy, and N. de Vries.
Multi-physics simulations using a hierarchical interchangeable software interface.
Computer Physics Communications, 184(3):456–468, 2013.

Junichiro Makino and Sverre J. Aarseth.
On a hermite integrator with ahmad-cohen scheme for gravitational many-body problems.
Publications of the Astronomical Society of Japan, 44:141–151, 1992.

Michiko Fujii, Masaki Iwasawa, Yoko Funato, and Junichiro Makino.
Bridge: A direct-tree hybrid n-body algorithm for fully self-consistent simulations of star clusters and their parent galaxies.
Publications of the Astronomical Society of Japan, 59(6):1095–1106, 2007.

V. Belokurov, D. B. Zucker, N. W. Evans, J. T. Kleyna, S. Koposov, S. T. Hodgkin, M. J. Irwin, G. Gilmore, M. I. Wilkinson, M. Fellhauer, and et al.
Cats and dogs, hair and a hero: A quintet of new milky way companions.
ApJ, 654(2):897–906, 2007.

John E. Norris, Rosemary F. G. Wyse, Gerard Gilmore, David Yong, Anna Frebel, Mark I. Wilkinson, V. Belokurov, and Daniel B. Zucker.
Chemical enrichment in the faintest galaxies: The carbon and iron abundance spreads in the boötes i and dwarf spheroidal galaxy and the segue 1 system.
ApJ, 723(2):1632–1650, 2010.

Marla Geha, Beth Willman, Joshua D. Simon, Louis E. Strigari, Evan N. Kirby, David R. Law, and Jay Strader.
The least luminous galaxy: Spectroscopy of the milky way satellite segue 1.
AJ, 692(2):1464–1475, 2009.

Anna Frebel, Joshua D. Simon, and Evan N. Kirby.
Segue 1: An unenvolved fossil galaxy from the early universe.
ApJ, 2014.

Joshua D. Simon, Marla Geha, Quinn E. Minor, Gregory D. Martinez, Evan N. Kirby, James S. Bullock, Manoj Kaplinghat, Louis E. Strigari, Beth Willman, Philip I. Choi, and et al.
A complete spectroscopy survey of the milky way satellite segue 1: the darkest galaxy.
ApJ, 733(1):46, 2011.

H. C. Plummer.
On the problem of distribution in globular star clusters.
MNRAS, 71:460–470, 1911.

W. L. Sweatman.
A study of lagrangian radii oscillations and core-wandering using n-body simulations.
MNRAS, 261(3):497–512, 1993.

N. Caon, M. Capaccioli, and R. Rampazzo.
Photographic and ccd surface photometry of 33 early-type galaxies in the virgo cluster. i. the data.
A&A Supplement Series, 86:429, 1990.

R. Domínguez, M. Fellhauer, M. Blaña, J. P. Farias, J. Dabringhausen, G. N. Candlish, R. Smith, and N. Choque.
Could segue 1 be a destroyed star cluster? - a dynamical perspective.
MNRAS, 461(4):3630–3638, 2016.